Title
Structural Dynamics of Copper Nanomaterials for CO2 Electrocatalysis

Author
Li, Yifan

Publication Date
2019

Peer reviewed|Thesis/dissertation

Structural Dynamics of Copper Nanomaterials for CO_2 Electrocatalysis

By

Yifan Li

A dissertation submitted in partial satisfaction of the

requirements for the degree of

Doctor of Philosophy

in

Chemistry

in the

Graduate Division

of the

University of California, Berkeley

Committee in charge:

Professor Peidong Yang, Chair
Professor Omar M. Yaghi
Professor Alexis T. Bell

Fall 2019

Abstract

Structural Dynamics of Copper Nanomaterials for CO_2 Electrocatalysis

by

Yifan Li

Doctor of Philosophy in Chemistry

University of California, Berkeley

Professor Peidong Yang, Chair

Electrons are the currency of the future energy economy. With a host of renewable sources of electrical energy and steadily decreasing cost of generation, our ability to store that electricity via chemical bonds becomes increasingly paramount. Development of materials that allow the transformation of electrical energy to chemical energy, *e.g.* the electroreduction of CO_2 to value-added chemicals and fuels, will push our energy infrastructure to new heights. Despite considerable progress in thermal gas-phase heterogeneous catalysis of CO_2, the heterogeneous electrocatalysis of aqueous CO_2 under room temperature and neutral pH has remained challenging. The key gating obstacle has been the development of catalysts that effect efficient and selective formation of higher order products such as methane or multicarbons, for which only copper has emerged as a candidate material. To design next-generation electrocatalysts for CO_2 conversion to multicarbons (CO_2-to-C_{2+}), the relationship between activity/selectivity and catalyst structure must be better understood, to identify the structural motifs that define CO_2-to-C_{2+} active sites. Recent work has consistently revealed that copper nanomaterials undergo considerable structural change under operating conditions. Thus, a central challenge to the understanding of these active surfaces is their dynamic nature under operation in electrochemical conditions, especially as applied to nanoscale electrocatalysts. Hence, this dissertation centers around structural dynamics of copper-based nanocatalysts under CO_2 electroreducing conditions.

After a brief introduction to the problem statement and fundamental concepts related to heterogeneous electrocatalysis of CO_2 to value-added products, I discuss the prospects and existing work around Cu structural evolution in Chapter 1. In Chapter 2, I show how the link between structural evolution and catalytic activity change can be clearly shown on a Cu nanowire catalytic platform, and further show how strategies that mitigate structural change also impact selectivity retention. In Chapter 3, I move to a copper nanoparticle ensemble platform with intriguing activity for multicarbon formation, coupled with a striking structural evolution. I illustrate the dichotomy between the *apparent* evolution and active structure via conventional *ex situ* measurements, and the structural and catalytic insights revealed by more comprehensive investigation using

preservation strategies. In Chapter 4, I discuss how *in situ* characterization techniques assist the illumination of such structural evolution under electrocatalytic conditions, and further explore what additional advances are needed to harness these insights. Finally, I close in Chapter 5 with an outlook on materials development for CO_2 electrocatalysis as it stands at time of writing. Overall, this dissertation seeks to provide a narrative of the relationship between an electrochemical materials scientist and the concept of structural dynamics. Through the works to be described, this dissertation will take the reader on a journey from emphasizing stabilization and mitigating structural change, towards understanding it for the eventual purpose of leveraging such structural change as another dimension of electrocatalyst design.

I reserve this dedication space for everyone who has suffered, or currently suffers, from depression, anxiety, suicidal ideation, and all other mental health related issues in graduate school or academic research, whatever the cause. And I dedicate myself to making things better.

Acknowledgments

First and foremost, I acknowledge and thank my graduate advisor Professor Peidong Yang. His support and guidance throughout my graduate career has been invaluable in both my research and future directions. I am deeply grateful for the many opportunities that he has offered me over the years, to work on fascinating science, to think independently, and to present my work and myself to wide audiences.

Throughout my graduate journey, I have had the pleasure of working with many PhD students and postdocs in the Yang group and otherwise who have similarly shaped the scientist I am today. I acknowledge Dr. Dohyung Kim especially, not only for being a mentor in my early years and a close collaborator, but for continuing to offer me his insight and guidance as we continue our academic journeys. In no particular order, I also sincerely thank the many collaborators and colleagues I have enjoyed working with and learning from, including Dr. Nigel Becknell, Professor Michael Ross, Dr. Fan Cui, Dr. Chenlu Xie, Dr. Zhiqiang Niu, Sheena Louisia, and Sunmoon Yu.

To the friends who have brightened my graduate days even in the darkest hours, I offer my thanks as well. Though here there are too many to list, I especially wish to thank those with whom I've had many stimulating discussions here at Berkeley: Dr. Xinyi Zhou, Zoe Watson, Chrissy Stachl, Dr. Tom Osborn Popp, Dr. Andreana Rosnik, Dr. Wojciech Osowiecki, and Dr. Meghan Hauser. I similarly acknowledge Science Leadership and Management, the Graduate Division, and Cleantech 2 Market and their affiliated members for the various professional development opportunities they have offered me.

I also thank the various faculty members, committee members, senior scientists, etc. at UC Berkeley and elsewhere who have taken time to speak with me regarding various matters, or who have dedicated time towards supporting my career. These include (but are not limited to) Professors Gabor Somorjai, Marcin Majda, Alex Bell, Omar Yaghi, John Hartwig, Andrew Bocarsly (Princeton), Chong Liu (UCLA), Nikolay Kornienko (University of Montreal) and Dr. Shaul Aloni (LBNL).

In addition, this work, and my graduate career as a whole, has been supported financially by the Department of Energy, by University of California, Berkeley, and by Lawrence Berkeley National Lab.

And lastly, I thank my parents, my family, and my partner Michelle for their everlasting love and support, and without whom, I could not possibly have come this far.

Table of Contents

Chapter 1. Introduction

In this chapter, I introduce the problem of carbon dioxide electrocatalysis, or the CO_2 reduction reaction (CO2RR) in the context of similar and related electrochemical technologies that ultimately seek to use renewable energy as a means of enabling chemistry. I open by offering a high-level overview of the prospects of such a technology, followed by an explanation of key targets and metrics which define research challenges. I relate these challenges to fundamental research questions rooted in materials chemistry, contextualized within recent literature reports of catalyst design and understanding. Central to this discussion will be the concept of structural dynamics under operating conditions, which offer not only additional challenges in shaping our understanding of catalyst surfaces, but also intriguing opportunities to expand the library of catalyst design. Finally, I outline the thread of research discussed in the remainder of this dissertation and through my PhD work, which seeks to understand these structural dynamics with the ultimate objective of manipulating them to aid catalyst design.

1.1 Carbon Dioxide Electrocatalysis in the Ecosystem of Renewable Energy

Since the Industrial Revolution, rising energy demands coupled with unsustainable greenhouse gas emissions have resulted in a plethora of national and global issues haunting future society.[1] Over-reliance on fossil fuels to supply both energy and petrochemicals leads to geopolitical instability owing to the unequal distribution of such resources across the world. Furthermore, extracting these finite resources becomes increasingly intensive and damaging to the environment. Greenhouse gas emissions, particularly CO_2, result in a warming overall climate, significant ecological disruption, and an upswing in natural disasters and extreme weather events.[2,3] Such anthropogenic climate change has been clearly linked to significant costs to the economy, as well as contributing to major public health crises.[4] Furthermore, rising atmospheric CO_2 concentrations lead to ocean acidification, causing further damage to oceanic biodiversity and biochemistry.[5]

Nevertheless, it is undeniably true that modern society owes its success to the processes related to fossil fuel utilization. Much of society's energy, materials, and chemicals are ultimately derived from the building blocks of CO_2, H_2O, and solar energy. Nature's magnificent photosynthetic machinery is capable of converting such building blocks into biomass, which over the course of millions of years become fossil fuels. This process is visualized in Fig. 1.1. The implication, therefore, is that beyond harmful byproducts such as greenhouse gas emissions, we can consider modern society to be built around a chemical reaction with untenable slow kinetics, a rate on the order of millions of years.

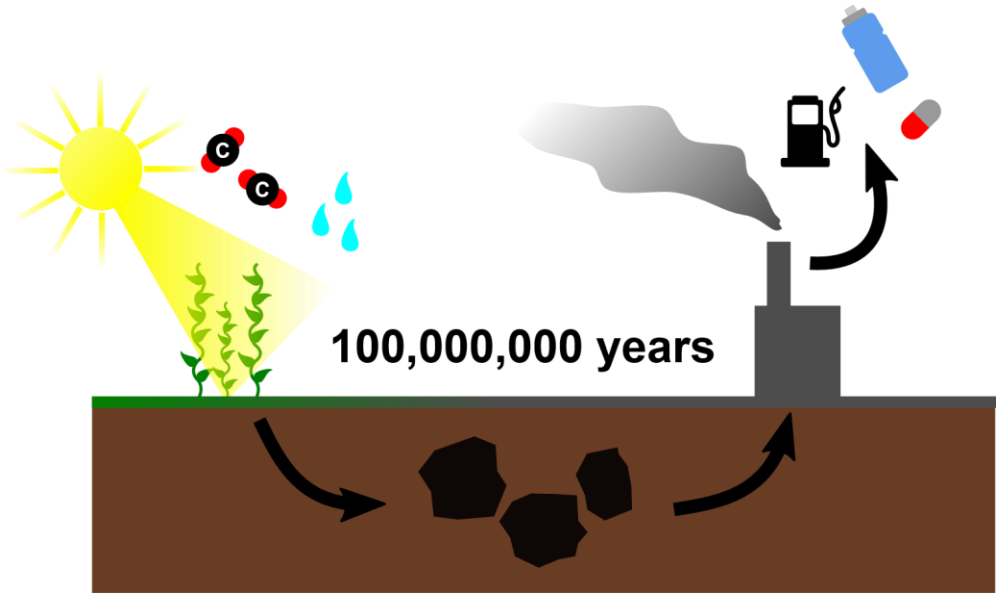

Figure 1.1. The unsustainable carbon ecosystem as it exists today, relying on a million-year chemical reaction to generate critical fuels, chemicals, and materials concomitant with untenable greenhouse gas emissions.

In the face of these threats related to the over-reliance on fossil fuels, society has made great leaps in furthering the use of renewable energy to supplement and supplant this unsustainable process. In particular, the massive growth in solar and wind energy in the U.S. and other countries across the world has been encouraging. Renewable electricity is projected to continue to cheapen in the future, such that electricity should be considered the currency of the future energy economy.[6] In such a world, the conversion of renewable electrons into other value-added processes will drive society much as fossil fuel utilization does now. Electrolysis is already critical in industrial processes such as aluminum refining and the chlor-alkali process. So-called "solar fuels" (though theoretically the renewable electricity is agnostic to whether the electrons are generated directly from solar photons or through other renewable sources, *e.g.* wind) already exist in commercially ready form as renewably-derived hydrogen fuel from water splitting.[7] Hence, the further advancement of renewable electricity conversion to fuels and chemicals is extremely attractive.

Eventually, we should seek a process through which society bypasses the untenably slow kinetics of the fossil fuel reaction. Instead, if CO_2, water, and renewable energy can be directly converted into value-added products, we achieve a renewable path towards closing the carbon cycle, mitigating greenhouse gas emissions while supplying value-added fuels and chemicals using abundant renewable electricity (Fig. 1.2). Simultaneously, this process serves to address the intermittency problem in renewable electricity generation, potentially allowing grid-scale management of crests and troughs in the energy generation time profile.

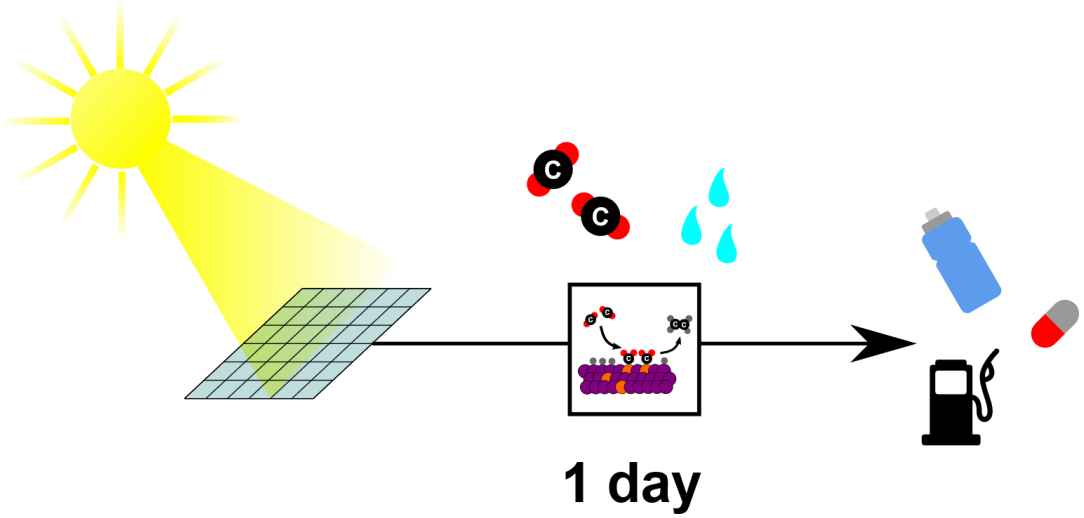

Figure 1.2. A sustainable alternative powered by renewably-derived electricity, using a catalyst that can convert CO_2 into value-added chemicals.

CO_2 electrocatalysis revolves around the development of materials that can catalyze the conversion of CO_2 into value-added products using electricity as an energy source (the CO_2 reduction reaction, or CO2RR). Many components are necessary in a full-cell system (Fig. 1.3) for overall CO_2 conversion, including a cathode material for CO2RR, an anode material to complete the circuit and supply a corresponding oxidative process, an electrolyte to serve as conductive medium, and an overall cell design that manages the flow of reactants and products (which may include, for instance, a membrane that separates the cathodic and anodic chambers).

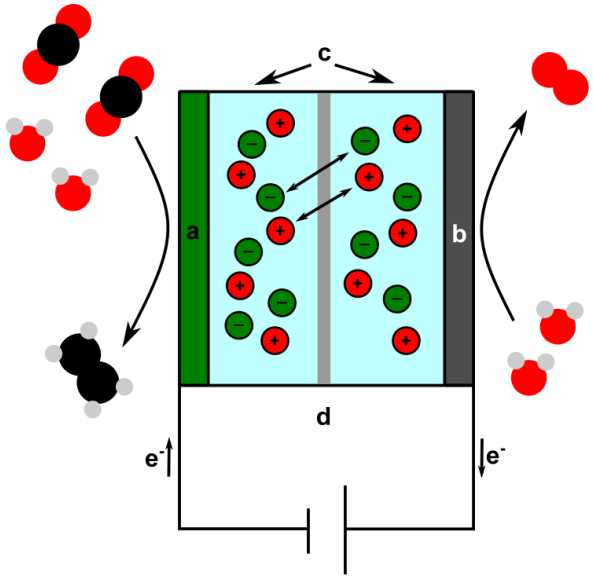

Figure 1.3. Schematic of a typical full cell for electrolytic CO_2 conversion. The principal components are (a) the cathode, (b) the anode, (c) the electrolyte, (d) the membrane (not strictly necessary but frequently employed), through which either cation or anion exchange can occur. As

representative electrochemical examples, CO_2 reduction to ethylene is shown on the cathode and water oxidation to dioxygen on the anode. Additional proton exchanges necessary for reaction balance are not shown for clarity. Black circles: carbon, red circles: oxygen, gray circles: hydrogen.

Fundamental questions in CO_2 electrocatalysis center on the behavior of the cathode material, and how different cathode materials respond to CO2RR. Ultimately, electrocatalytic science aims to answer the fundamental questions of which materials serve as active sites for CO2RR, and how those active sites can be manipulated to modulate the electrochemical activity and selectivity of the reaction.

1.2 Key Concepts and Challenges in Heterogeneous Carbon Dioxide Electrocatalysis

First, I emphasize that the scope of this dissertation will revolve around the design and understanding of heterogeneous electrocatalysis for CO2RR. Indeed, homogeneous and enzymatic electrocatalytic systems exist as well, for which the challenges are unique.[8] For instance, homogeneous systems tend to catalyze CO2RR with high selectivity, and are often conducted in organic solvents with higher solubility for CO_2. Enzymatic systems tend to have ideal selectivity for the reaction. Both systems, however, generally have significantly reduced turnover compared to heterogeneous catalysts, and potentially also suffer from issues of post-reaction product separations. However, some interesting recent work has shown that the concepts in such catalysts can be applied to "tethered" catalytic systems that behave in a heterogeneous manner but use the principles adopted from homogeneous catalysts.[9,10] Nevertheless, the focus here will be on archetypal heterogeneous electrocatalysis, *i.e.* the interactions of solid-state cathodes in an electrochemical environment with reactants and intermediates under the applied potential.

The primary challenges in heterogeneous CO_2 electrocatalysis can be described in three parts: (i) activity, (ii) selectivity, (iii) stability. In summary, the ideal electrocatalyst will catalyze CO_2 electroconversion to a single product at the exclusion of competing reactions (selectivity) with high turnover and low energy input (activity). Furthermore, it will be robust to continuous operation, and ideally even to changes in its electrochemical environment (stability). This dissertation primarily concerns itself with the formation of "higher order" products, that is, products beyond the 2-electron conversion of CO_2 to CO or formate. For these reactions (*i.e.* CO_2-to-CH_4 and CO_2-to-C_{2+}), activity and selectivity are the near-term primary challenges, as will be elaborated upon in section 1.3.

Beyond these challenges, many significant barriers remain to commercial development, including the successful isolation and purification of product streams, overall full cell engineering that minimizes wasted energy, and successful integration with renewable electricity generating systems.[6,11] Such considerations, while vitally important to the technology as a whole, will only be considered in passing in the scope of this dissertation, which focuses on understanding the CO_2 electrochemistry that happens on the cathodic catalyst surface.

CO2RR is a relatively young field with industrial demonstrations only beginning to emerge in recent years. As such, the identification of proper quantitative metrics and criteria for evaluating catalyst performance is a topic of lively debate.[12] From a basic science perspective, metrics should be selected to have some relevance to end-use performance; however, ideally they should relate to the molecular or atomic picture of electrocatalysis on the materials surface. The use of metrics that

more closely describe the mechanistic aspects of the catalytic reaction, rather than the bulk performance aspects of the electrochemical system, allow more rigorous analysis of the catalytic component rather than the device as a whole.

As a case in point, CO2RR electrocatalysts are frequently evaluated by their faradaic efficiency (F.E.) at a given overpotential (these terms will both be explained in greater depth later in this section). Essentially, such a metric purports to describe the selectivity of the catalyst, but is sometimes used as a figure of merit to tout a catalyst's "activity" in general. However, the F.E. describes a given product as a percentage of all products, without explicit consideration of mechanistic implications. A higher F.E. may result from higher turnover of the product in question, or it may result from suppression of competing reactions, as two examples. These two mechanistic pictures describe fundamentally different evaluations of the catalytic surface – in one case, the catalyst is more active but indiscriminately so; in the second, the catalyst is less active but selective. A full reporting of metrics to evaluate "activity" would include the production rate, or the electrochemical current, such that the *partial current density towards all products* may be calculated and compared.

However, even the reporting of partial current densities with overpotential is insufficient. The effects of surface area or roughness factor in modulating *extrinsic* factors to electrocatalysis (*e.g.* local pH) muddies the picture of what defines catalytic motifs that modulate *intrinsic* activity. Thus, ideally, an analog closer to the turnover frequency (TOF) used in other fields of catalysis would be helpful to derive an understanding more intimately related to the surface interaction with reactant and intermediate adsorbates. As one example, the specific current (normalized to electrochemically active surface area) can be used. The search for a complete and rigorous set of reporting criteria for CO2RR electrocatalysis is ongoing; nevertheless, in the spirit of open and collaborative science, full sets of electrochemical parameters should be made easily accessible in publication.

For the remainder of this section, I define the primary metrics that will be used in this dissertation to understand the catalysts employed and how their surfaces benefit electrocatalytic activity and selectivity. In no case do I imply that my evaluation is exhaustive; however, in all cases I endeavor to use the appropriate data to support a given conclusion or test a given hypothesis.

- Faradaic efficiency (F.E., %): The percentage of total electrons passed that are used for a specific electrochemical product.

- Current density (j, mA/cm^2): The number of electrons per area per unit time that pass through the catalyst to undergo an electrochemical process; in this case, almost all current will be faradaic current towards the cathodic HER or CO2RR reactions. Current density describes the bulk productivity of an electrode, and unless otherwise specified, the area used is geometric (*i.e.* the footprint of the electrode).
    - Partial current density (j_x, mA/cm^2): Multiplying j by F.E. yields an electrochemical analog of the production rate for a given product.
    - Specific current density (j_{ECSA}, mA/cm$^2{}_x$): Normalizing current density by the roughness factor or electrochemically active surface area (ECSA) yields a measure more closely attuned to the intrinsic activity of the catalyst.

- Roughness factor (RF, cm^2/cm^2 or unitless): The ratio of real or active surface area to geometric surface area.

- Overpotential: Considering the thermodynamic redox potential of a given process, the amount of additional potential that must be applied to achieve a given current density. For convenience, when considering catalytic activity, all potentials will be referenced against the reversible hydrogen electrode (RHE), defined as the potential of the H^+/H_2 redox couple independent of pH (hence following the Nernst equation for $[H^+]$). However, when referencing electrochemical events unassociated with catalytic performance, other reference potentials such as Ag/AgCl may be used.

1.3 Thermodynamics and Kinetics of CO_2 Electrocatalysis

As the catalysts studied in the remainder of this work operate under aqueous CO_2-reducing conditions, the thermodynamics and kinetics of CO_2 reduction with comparison to the primary competing reaction (hydrogen evolution reaction or HER) will be discussed. The treatment in this section will somewhat follow the path of a CO_2 molecule as it eventually is electroconverted to value-added products.

In aqueous environments (*e.g.* 0.1 M $KHCO_3$, a commonly used electrolyte buffer), CO_2 from the gas phase achieves an equilibrium with dissolved CO_2 in the aqueous phase. In bicarbonate systems, this gas-aqueous equilibrium extends to a second equilibrium with the acid-base reactions that take dissolved CO_2 to bicarbonate and eventually carbonate. These combined equilibria can be described as follows:[13]

$$CO_2\,(g) + H_2O \rightleftharpoons CO_2\,(aq) + H_2O \rightleftharpoons H_2CO_3\,(aq) \rightleftharpoons H^+ + HCO_3^- \rightleftharpoons 2H^+ + CO_3^{2-}$$

In general, ambient CO_2 electrocatalysis is conducted under a constant 1 atm CO_2. Before application of current, the concentration of dissolved CO_2 is derived from Henry's Law, *i.e.* that the concentration in solution is linearly proportional to the atmospheric partial pressure multiplied by a constant specific to the gas. For CO_2 at 1 atm, this yields a concentration of approximately 34 mM.[13] Meanwhile, the concentrations of other CO_2-related anions, which compose the overall carbon content of the electrolyte, are determined partially by the concentration of K^+ counterions (in our case, 100 mM) and partially by the static concentration of 34 mM CO_2 (aq). Calculating these equilibria using the known pKa values for bicarbonate (HCO_3^-) and carbonate (CO_3^{2-}) yields a steady-state pH of 6.8 with 100 mM HCO_3^- and negligible CO_3^{2-} concentration. Notably, bicarbonate and carbonate reduction have been shown to be exceedingly minor contributions to overall carbon conversion in CO2RR, likely due to electrostatic interactions that preclude the reduction of anionic species, even if bicarbonate plays a significant role in shuttling CO_2 to the surface.[14–16] Hence, despite a constant 100 mM source of carbon in the form of bicarbonate, 34 mM CO_2 (aq) is expected to be the primary source of all carbon products.

When faradaic current is applied, depletion of CO_2 (aq) at the electrode surface results in a concentration gradient across the electrolyte. The catalytic significance of this concentration gradient is revealed in the so-called "mass transport limiting current," *i.e.* there exists a ceiling at which the rate-limiting step of catalytic reactivity is the transport of CO_2 (aq) to the electrode

surface, and not the faradaic electron transfer. It is instructive to calculate the effective concentration of CO_2 in the gas phase, which under ideal gas law assumptions and 1 atm pressure is 45 mM. In other words, the mass transport limiting current is not defined by the "low solubility of CO_2 in water," as frequently discussed, but rather by the "low *diffusivity* of CO_2 in water." Many systems are being developed that overcome the mass transport limiting current by effectively thinning the Nernstian diffusion layer and hence facilitating diffusion of CO_2 to the electrode surface, and such systems (*i.e.* gas diffusion electrode architectures) offer additional advantages for device performance.[17–19] However, in general the materials in this dissertation will be studied in aqueous environments at potentials/currents at which electron transport is rate limiting.

Indeed, in such regimes, the rate-limiting step can succinctly be described as a one-electron transfer to CO_2, which dictates the electrokinetics of the reaction.[20] The thermodynamic requirements of CO2RR compared to HER are not overwhelmingly endergonic. For example, the 2-electron reduction of CO_2 to CO occurs at a thermodynamic redox potential of -0.1 V vs. RHE. Other common CO2RR products are listed in Table 1.1 with their corresponding stoichiometric electron transfers (per molecule product) and thermodynamic potentials.[8,21]

CO2RR product	**# electrons per product**	**E^0 (V vs. RHE)**
Formic acid (HCOOH)	2	-0.12
Carbon monoxide (CO)	2	-0.10
Methane (CH_4)	8	+0.17
Ethylene (C_2H_4)	12	+0.08
Ethanol (C_2H_5OH)	12	+0.09
Acetic acid (CH_3COOH)	8	+0.11
Propanol (C_3H_7OH)	18	+0.10

Table 1.1. List of cathodic half reactions in CO2RR and their thermodynamic potentials against the competing HER at a matching pH (*i.e.* the RHE reference potential), considering fully protonated products in an acidic media. Thermodynamic potentials are calculated from gas-phase Gibbs free energy of reaction using standard states, following previous literature, wherein the formation of byproducts such as H_2O should be considered as part of the calculation.

However, on many catalytic materials, HER is far more kinetically facile than CO2RR to any product at a given potential.[22,23] The kinetic barrier corresponds to an *overpotential*, which contributes to a reduced energy efficiency for the overall process (see 1.2). Thus, a major challenge lies in the relative selectivity of CO2RR compared with the major competing reaction of HER. On many early transition metals, the catalytic reaction of HER is far more active, hence precluding such materials to be used as CO2RR cathodes.[24]

Conversely, metals with poor HER activity are promising candidates for CO2RR. Such metals tend to favorably produce either carbon monoxide or formate in aqueous reducing conditions. The mechanistic branching between these two 2-electron products is interesting in its own right, but will not be deeply explored within the scope of this dissertation. Rather, considering the more complex chemistry of producing products beyond 2 electrons (denoted $CO2RR_{>2e-}$), only

Cu has been identified as an element capable of producing such products at reasonable overpotentials and selectivity.[21,25,26]

The thermodynamic origin of enhanced methane and multicarbon formation from CO_2 on Cu has been widely studied. As a qualitative argument, the classic Sabatier principle in heterogeneous catalysis can be applied here. Considering *CO as a key intermediate towards higher-order product formation, an intermediate binding strength towards this intermediate (*i.e.* not too strong or too weak) is necessary for high reaction rates.[20,22,27] This may be rationalized as follows: materials with weak binding strengths for *CO will tend to release such intermediates as products before further reaction, explaining metals such as Au or Ag. Meanwhile, materials with strong binding strengths will be subsequently poisoned upon irreversible binding of the adsorbate. The permanent blockage of these active sites results in pure selectivity for HER, which is observed in transition metals such as Pt, Fe, or Ni.

In fact, the thermodynamic and especially electrokinetic basis of this argument is far more complex. One must consider the relative binding energies of each relevant intermediate on a cathode surface. Fortunately, or perhaps unfortunately, these are observed to scale linearly with one another as the surface varies, such that modulating the surface does not dramatically affect selectivity due to the relative energetics of adsorbate-bound surfaces not significantly changing.[22,28,29] Hence, understanding the structure-activity and structure-selectivity relationships has strictly relied on the study of Cu surfaces, where further electron-transfer and chemical steps beyond the initial activation of CO_2 control activity and selectivity. The remainder of this chapter, and indeed of the dissertation at large, will focus on the nature of the Cu surface and how its atomic structure modulates these subsequent steps beyond CO_2 activation, which control the formation of higher-order products such as CH_4 and C_{2+} (multi-carbon products like C_2H_4 and ethanol).

1.4 Progress in the Design of Copper-based Electrocatalysts for $CO2RR_{2e^-}$

In the 1990s and early 2000s, pioneering work by Y. Hori et al. revealed that Cu was unique in converting CO_2 and relatedly CO to multi-carbon and otherwise higher order products.[24,30,31] The nature of CO_2 reactivity on polycrystalline Cu was then explored in-depth in a seminal work by K. Kuhl et al. in 2012;[25] since then, a truly mind-boggling number of studies have erupted from the literature regarding modifications of Cu-based catalysts for $CO2RR_{>2e^-}$. A number of excellent reviews summarize recent trends and advances in the development of Cu-based catalysts.[11,20,21,32–34] As such, in this section, my aim is not to exhaustively detail the progress in Cu catalyst development and understanding, but to highlight the paradigms that have developed around Cu catalyst design strategy and where fundamental questions remain unresolved. Through such discussion, I hope to contextualize the focus of this dissertation: the structural dynamics of a specific subset of copper nanocatalysts and the role of such dynamics in expanding the paradigms of catalyst design.

The selective formation of CH_4 is unique among the higher-order products in being the only $>2e^-$ product commonly observed that is not a multicarbon. The 4-electron product formaldehyde is likely not formed due to its instability. For reasons that are still not entirely elucidated, the 6-electron formation of methanol, which is common in heterogeneous gas phase hydrogenation of CO_2, is also not observed in aqueous electrolytic media, though some works have reported significant methanol formation in organic media.[35] Regardless, the selective formation of

methane in aqueous media is sometimes reported, for instance in the case of copper nanoparticles supported on glassy carbon.[36] Such formation typically occurs at very high overpotentials (-1.2 V vs. RHE and beyond); this, coupled with the fact that methane is not an attractive product for further chemistry, has resulted in the bulk of Cu-related work targeting the formation of multi-carbon hydrocarbons and oxygenates.[37]

Borrowing the time-honored principle of model system probing from gas phase heterogeneous catalysis, several works have started exploring Cu selectivity for multi-carbon products using model single crystal surfaces. C_{2+} selectivity was especially observed to depend on the relative proportions of specific facets, especially of (100) facets over (111).[30,38–42] Such observations were corroborated in the reduction of CO, commonly cited as an important intermediate for the formation of multicarbon products.[27,43–45] The dimerization of CO is one dominant mechanism for the formation of such C_{2+} products, with (100) terraces having a low barrier towards the formation of a CO-CO dimer.[46–48] Other works have shown that single crystals of specific facets present significantly different electrocatalytic selectivity; for example, large area (751) facet Cu was seen to enhance the selectivity for C_{2+} products, especially oxygenates.[42]

Translating these bulk-level observations to nanoscale design has been oft-attempted but of unclear success. The (100) facet has been synthetically targeted using electrochemical cycling,[49] plasma treatment,[50] and colloidal synthesis,[51] resulting in catalysts with high C_2:C_1 selectivity. However, in many of these cases, these cubes are Cu oxides that are reduced *in situ*. Characterization post-electrolysis shows that such oxide cubes lose their cubic nature, and thus much of their (100) faceting, after reduction.[52] Even for Cu^0 nanocubes, operating electrocatalytic conditions at high bias tend to cause "nanoclustering," resulting in electrochemical evolution.[53] This general bias-induced evolution is scientifically fascinating and will be discussed at length in chapters 2-4, but here it is mentioned to qualify the idea that (100) faceted catalysts in the nanoscale have been convincingly demonstrated.

In parallel with the well-defined surface faceting approach to catalyst design, another "class" of catalysts has emerged that is undergoing extensive research: oxide-derived copper (OD-Cu). Since initial work by Li et al. that OD-Cu and other metals promote increased electrocatalytic activity at modest overpotentials,[54,55] many research groups have emulated this approach through the deliberate oxidation and *in situ* reduction of copper surfaces. As a result, variously nanostructured copper catalysts are formed through chemical,[50,56,57] electrochemical,[58,59] or thermal[54,60] means, which are in aggregate labeled as "OD-Cu." Specific catalysts of this class have shown impressive catalytic activity by certain metrics (such as high C_{2+} F.E. at reduced overpotentials), which has sparked a substantial effort towards understanding the mechanistic origin of enhanced activity. The debate over the presence and potential activity of specific motifs, such as retained "subsurface oxides" or especially active grain boundaries among other suggested mechanisms, can be followed in recent reviews and pertinent literature and will not be covered extensively here.[11,61–63]

Consistent with my discussion in Chapter 1.2, such evaluation should be considered carefully given the metrics of such catalysts that are reported; however, the historical context as to the development of such mechanistic works does considerably inform the nature of my work in Chapters 3 and 4. More recent surveys and perspectives have raised an important consideration of considering the role of surface area and porous structures beyond the nanoscale, suggesting that in

many cases high surface area can be considered the principal determining factor for catalytic activity at reduced overpotentials towards C_{2+} products.[21,64,65] For one, high RFs result in high geometric current density, which produces high local pH.[65–67] As an extrinsic catalytic factor, high local pH simultaneously suppresses the competing HER, as well as potentially promoting dimerization.[68]

High RF catalysts also may access a diversity of active sites, which complicate characterization efforts but yield an overall high bulk productivity of desirable products (*i.e.* a high geometric current density but not normalized to ECSA). This factor likely contributes to recent work which compares a broad array of high-performance catalysts and shows that when normalized to ECSA of Cu, only minimal increase in activity is observed.[21] Furthermore, high surface area has been used as a design principle in and of itself, by exploiting a boost in mesoscopic transport of CO_2 using such porous structures.[69] These extrinsic factors conflate with discussion of intrinsic factors related to atomic-level catalyst understanding and serve as important caveats in the prior discussion. Regardless, it is inadvisable to completely disregard the progress that has been made in understanding the unique surfaces created by OD and other processes in recent years; rather, more effort should be made to carefully investigate the intrinsic activity of such surfaces, ideally isolating the nanoscale surface structures from the macroscopic structure that affects extrinsic effects.

As can be seen from the previous overview in sum, considerable effort has gone into understanding how surface structure modulates electrocatalytic activity and selectivity for CO2RR on Cu. From atomic level considerations such as crystal structure of facets, to broader nanoscale effects that may be induced by "OD-Cu," to length scales spanning microns and beyond that involve extrinsic effects of porosity and roughness, matters regarding the structure of Cu are considered key to understanding how to controllably design efficient catalysts for CO2RR. As such, it is perhaps mildly disturbing to now consider the prospect that all such surfaces may be structurally dynamic under operation: that is, the *in situ* structure is not guaranteed to be the well-characterized initial surface!

1.5 Structural Dynamics of Copper Nanocatalysts for CO_2 Electrocatalysis

It should be unsurprising to other fields of heterogeneous catalysis that catalytic surfaces change under operation. The issue of sintering is well-known in thermal catalysis, if not perfectly understood. Of course, the nature and difference of such change under high-temperature conditions vs. ambient conditions under bias should be considered very carefully, as will be discussed at length in later chapters. Generally, sintering and nanoparticle agglomeration are seen as undesirable pathways towards catalytic deactivation. However, recent studies have emerged which offer a perspective of catalyst change as activation, that is, the structures that are created due to structural dynamics are favorable for catalytic reactions of interest.[70–72]

Several works have now shown that the copper surface changes under CO_2-electroreducing conditions, both in the bulk and in the nanoscale. In later chapters, particular attention will be paid to certain works that examine Cu nanocrystals and their structural evolution in depth, in comparison to the dynamics explored throughout my body of work. However, here I briefly survey the progress that has been made thus far. Naturally, the reduction of copper oxides results in considerable structural change as the crystal lattice reconstructs to form metallic Cu – such evolution has been tracked *via* microscopic[62] and spectroscopic[73] methods, albeit with some

conflicting and unexpected conclusions. For instance, the extent of reduction of an oxidized Cu catalyst is difficult to probe without clear evidence that the material being probed is indeed participating in catalysis in a closed circuit.

Additionally, even metallic Cu undergoing no change in oxidation state has been shown on multiple occasions to reconstruct during reductive CO2RR. *In situ* electrochemical scanning probe techniques have revealed a remarkable surface reconstruction of Cu foil surfaces to (100) under bias.[74] Nanoscale catalysts are particularly susceptible to such evolution, as has been demonstrated for nanocubes[53] and nanoparticles.[36,75] Over this backdrop of previous work and understanding revolving around both catalyst design for $CO2RR_{>2e-}$ and structural dynamics within heterogeneous CO_2 electrocatalysis, I now outline the thread of my work, which is visually summarized in Figure 1.4.

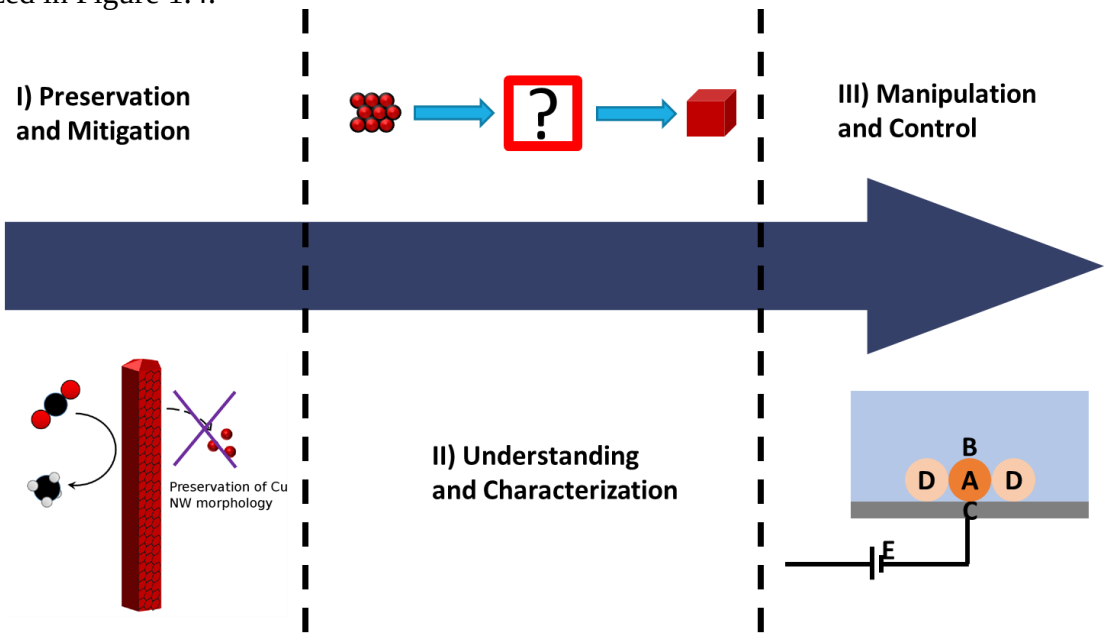

Figure 1.4. The throughline of the work outlined in this dissertation, regarding the structural dynamics of copper-based nanomaterials during CO_2 electrocatalysis. Starting from the idea that structural change should be mitigated or prevented, we will approach a more holistic understanding of how structural dynamics occurs and what new structures are created, moving towards a future in which such evolution can guide further catalyst design.

As observed in the cases of nanoparticle sintering or agglomeration, the structural degradation of nanoscale catalysts is often detrimental to a catalyst's ideal performance. For example, a highly selective catalytic surface may degrade under operating conditions, yielding a loss in selectivity. Hence, the preservation of such surfaces, or equivalently the *prevention* of structural dynamics, is one avenue towards improving catalyst design. Furthermore, access to such methods of catalyst preservation allows systematic probing of the structural sensitivity of a given structure towards a reaction. I illustrate this in Chapter 2 with the ultrathin copper nanowire system and its wrapping with reduced graphene oxide.

However, the destruction or degradation of a catalyst surface can equivalently be seen as the creation of new surfaces. Under such a lens, these new surfaces provide intriguing opportunities for observing new active sites that are otherwise difficult to access. If a catalyst

surface is observed to transform under operation, and this catalyst at the steady state achieves desirable catalytic properties, then the transformation itself deserves scrutiny and merits effort towards *understanding* structural dynamics. Chapter 3 showcases the considerable characterization efforts that are needed to fully understand such a structurally dynamic system, and how in doing so we finally gain insight into the parameters that influence such dynamics and implications for catalytic active site identification.

Finally, with the view that new surfaces competent for desirable catalytic transformations can be created *in situ*, we open novel prospects for catalyst design that themselves require structural evolution. The synthesis of new surfaces *in situ* through electrochemical evolution offers avenues to catalytic motifs that may be otherwise difficult to access through conventional techniques (such as top-down fabrication or colloidal synthesis). By seeking to *control* these structural dynamics, we ultimately aim to expand the library of parameters for catalyst design. Chapter 4 begins by discussing burgeoning efforts to characterize such evolution using state-of-the-art *in situ* techniques, and ends with a preview of how electrochemical parameters may influence the electrochemical evolution, offering a window into how such control may eventually be achieved.

I close in Chapter 5 with my perspective on catalyst development and design for CO2RR, especially with an eye towards Cu-based catalytic surfaces. In many ways, understanding in this field has only begun to develop, and it is my hope that through my work and related work by my contemporaries, a unified picture around the origin of electrochemical dynamics of Cu in CO_2-reducing conditions will emerge. Such understanding would be critical to unlock the fundamental picture of active CO_2 conversion to value-added C-C products.

Chapter 2. Structural Sensitivity and Preservation on Ultrathin Copper Nanowire Electrocatalysts

Reproduced[76] in part with permission from:
Li, Y.*, Cui, F.*, Ross, M. B., Kim, D., Sun, Y., and Yang, P. "Structure-Sensitive CO2 Electroreduction to Hydrocarbons on Ultrathin 5-fold Twinned Copper Nanowires," *Nano Letters*, **2017**, 17, 1312-1317, doi: 10.1021/acs.nanolett.6b05287.

2.1 Preface

This chapter describes my initial foray into the understanding of structurally dynamic copper-based nanocatalysts using an ultrathin (diameter ~20 nm) five-fold twinned copper nanowire system previously developed for conductive transparent electrodes. I show that with proper catalyst processing, the nanowire system exhibits interesting catalytic properties for the conversion of CO_2 into $>2e^-$ products, specifically, extremely selective methane formation, reaching 55% Faradaic efficiency at -1.25 V vs. RHE while other carbon products are produced with less than 5% F.E. total. This selectivity was found to be sensitive to morphological changes in the nanowire catalyst observed over the course of electrolysis. Wrapping the wires with graphene oxide was found to be a successful strategy for preserving both the morphology and reaction selectivity of the Cu NWs. These results suggest that product selectivity on Cu NWs is highly dependent on morphological features, and that hydrocarbon selectivity can be manipulated by structural evolution or the prevention thereof.

2.2 Introduction

Electrocatalytic CO_2 conversion to value-added products is an attractive means for mitigating the unsustainable rise in anthropogenic CO_2 emissions. Coupled with renewably-generated electricity, a CO_2 electrolyzer provides simultaneous carbon fixation and renewable energy storage.[34,77,78] Many catalytic studies in recent years have refined the electrocatalytic conversion of CO_2 to CO, increasing its commercial viability by reducing overpotential and increasing current density.[79–84] However, an efficient electrocatalyst for the conversion of CO_2 to higher order products beyond CO has yet to be developed. Though several metals and metal alloys are known to produce small quantities of higher order products at high overpotentials,[23] only copper has been shown to do so with appreciable activity.[24] Controlling product selectivity, meanwhile, remains a challenge using a copper foil catalyst.[85] Comparisons between the same copper foil under various chemical treatments, creating different nanostructures, resulted in remarkable differences in product selectivity.[86] Therefore, understanding how to manipulate selectivity on the copper surface *via* nanostructure is critical for the development of new selective catalysts.

Nanoscale catalysts present considerable advantages compared to their bulk counterparts, including higher surface areas and a high density of low-coordination, high-activity catalytic sites. Indeed, nanostructuring has been shown to improve activity for a variety of catalytic materials, primarily by improving turnover (*i.e.* partial current density towards products) and/or selectivity

at lower overpotentials.[80,81,83,87] Typically, nanostructured catalyst films are produced through chemical and electrochemical treatments of copper foil, resulting in drastically improved selectivity and activity for high-value products like ethylene.[49,55,56,88,89] However, the mechanism and origin for the improved activity is poorly understood, requiring a platform with precise control over size, shape, and composition. Colloidal nanomaterial synthesis provides a means to synthesize such well-defined electrocatalysts, but has only recently been explored for studying CO_2 electrocatalysis. For example, several recent works have conducted investigations into electrocatalytic CO_2 reduction on various colloidal Cu nanomaterials.[36,51,90–92]

One-dimensional nanowires (NWs) are an especially intriguing class of nanostructure for CO_2 electrocatalysis. Previous work on CO_2 reduction on Cu NWs have shown improved performance on wires with diameters ranging from 100 nm to several microns.[93–95] However, the catalytic activity of ultrathin Cu NWs, with well-defined twin boundary edges, has yet to be investigated. The presence of low-coordination edge sites on an ultrathin nanowire presents a catalytic surface with potential for high activity and unique selectivity, due to the difference in intermediate binding on low-coordination sites. Zhu et al have previously shown markedly higher CO selectivity on ultrathin Au NWs, which they attribute by DFT calculations to enhanced intermediate binding on edge sites.[82] In addition, the presence of grain boundaries in copper nanoparticles have been shown to directly promote CO electroreduction to multi-carbon products.[60] Thus, studying the catalytic influence of the ultrathin NW morphology using ultrathin Cu NWs[96] is highly relevant to CO_2 electroreduction.

Another point of interest for the nanowire geometry is its ability to be modified by graphene oxide wrapping. Previous work on copper nanoparticles has shown a tendency for particles to sinter at high bias, potentially as a result of electrochemical migration or copper dissolution and redeposition.[36] We have recently demonstrated that ultrathin Cu NWs can be wrapped with a thin reduced graphene oxide (rGO) shell to enhance their structural stability.[97] The wrapped Cu NW system provides an intriguing platform for studying the catalytic effects of morphological change and its prevention. Therefore, we set out to investigate how well-faceted Cu NW surfaces change over electrolysis and whether the electrocatalytic activity changes in conjunction. Subsequently, we wished to study whether rGO-wrapping could preserve the Cu NW morphology under electrolytic conditions, and whether such a strategy simultaneously preserves electrocatalytic properties hypothesized to be morphology-dependent.

2.3 Materials and Methods

2.3.1 Synthesis of Cu NWs.

In a typical synthesis, 85mg of $CuCl_2 \cdot 2H_2O$, 0.5g of tris(trimethylsilyl)silane were dissolved in 5 g of oleylamine in inert environment. The mixture was then slowly heated up to 110°C and kept at this temperature until the color of the solution turned light yellow. Then, the temperature of the reactants was slowly increased to 160°C. The reaction was left to continue for 12 hours. The copper nanowires were collected through centrifugation and further washed with toluene twice to remove ligands and unreacted reagents. The nanowires were finally dispersed in toluene and stored in a dry nitrogen box before use.

2.3.2 Preparation and charaterization of copper-graphene oxide (GO) core-shell nanowires.

Sub-ten nanometer graphene oxide nanosheets were synthesized using a previously reported approach.[97] To make copper-GO core-shell nanowires, a dilute solution of graphene oxide nanosheets in methanol was prepared with a concentration of 0.05 mg/ml. 2.5 ml of 2 mg/ml copper nanowire toluene solution was added in 20 ml of GO solution in a dropwise fashion, upon vigorous stirring. Then, the mixture was ultrasonicated for 3 min. The core-shell nanowires were collected by centrifugation at 10000 rpm for 10min. Then, the sample was further washed twice with isopropyl alcohol (IPA) to remove excess graphene oxide. The final products were dispersed in IPA and stored in a dry N_2 box. To change the thickness of the GO shell, we reduced the concentration of GO solution and follow the same procedure described above. The GO was then electrochemically reduced *in situ* to reduced graphene oxide (rGO). Energy dispersive spectroscopy (EDS) mapping was carried out with an FEI TitanX 60-300.

2.3.3 Preparation and characterization of CuNW/CB/GC electrodes.

The washed CuNWs were first loaded onto carbon black (Ketjen) at loading ratio of 20% w/w and sonicated in hexanes for 30 minutes, creating a CuNW/CB stock solution. This solution was then spread on 1cm^2 glassy carbon plates (Goodfellow) by micropipette and dried under nitrogen such that a total mass of 20 micrograms CuNW/CB was loaded per electrode.

Each individual electrode was only used for one electrolysis. After electrolysis, electrodes were immediately imaged using SEM (JEOL FE-SEM). The CuNW/CB catalyst was then recovered by sonication in solvents such as hexanes or 2-propanol and imaged under TEM (Hitachi H-7650). Between electrolyses, glassy carbon plates were wiped clear before being immersed in 0.5 M nitric acid overnight and rinsed copiously with nanopure water (EMD Milli-Q, 18.2 MΩ, <5 ppb TOC).

Electrodes for Raman spectroscopy were prepared by dropcasting bare and wrapped Cu NWs onto a piece of titanium foil to prevent any carbon signal arising from the substrate, at a geometric surface area coverage equivalent to that on glassy carbon. For the post-electrolysis sample, electrolysis was conducted in CO_2-saturated 0.1 M $KHCO_3$ at -1.25 V vs. RHE. The foil was then rinsed lightly with nanopure water before characterization. Raman spectroscopy was performed using a Horiba confocal Raman microscope with a 20x objective at 633 nm. Raman spectra were normalized by laser power (typically ~10 mW) and collection time (30-120s) and then corrected to a linear baseline.

2.3.4 Electrocatalytic testing for CO_2 reduction activity.

Electrocatalytic tests were conducted with a potentiostat (Bio-Logic) in a custom-built three-electrode cell. For both catholyte and anolyte, 0.05 M potassium carbonate solution was prepared by dissolving potassium carbonate (99.997% puratronic, Alfa Aesar) in nanopure water. Before electrolysis, the electrolyte was purged through in a sealed cell with ultrahigh purity CO_2 (99.999%, Praxair) for at least twenty minutes to make a CO_2-saturated 0.1 M $KHCO_3$ solution. A composite platinum wire and gauze (Alfa Aesar) was used as a counter electrode in an anodic compartment separated from the rest of the cell using a Nafion cation exchange membrane to prevent product re-oxidation. All experiments were conducted using a Ag/AgCl (1 M KCl) reference electrode (CHI Instruments). For polycrystalline copper foil experiments, a 0.6 cm^2

rectangle of high-purity Cu foil (Alfa Aesar, 99.999%) was rinsed in 85% phosphoric acid for 30 seconds, then copiously rinsed with nanopure water before use as working electrode.

In a typical experiment, 10 mL of electrolyte was magnetically stirred in the cathodic compartment, resulting in a headspace of 41 mL. The electrode was held at constant bias using chronoamperometry for either a set time or a set amount of charge, after which a 1mL gas sample was taken by syringe from the headspace. The gas was injected into a gas chromatograph (SRI) equipped with a molecular sieve 13X column, HayeSep D porous polymer column, thermal conductivity detector, and flame ionization detector. Ultra high purity Ar (99.999%, Praxair) was used as carrier gas. The concentration of product gases was determined using calibration curves from standard gases (Matheson TriGas). Liquid sample was taken at the end of electrolysis and mixed with D_2O at a 9:1 ratio for product analysis. Quantitative NMR was conducted on a Bruker AV-500 instrument with dimethyl sulfoxide as internal standard. Further details regarding calculations for gas and liquid products can be found in the appropriate sections below.

2.3.5 iR compensation and current-time behavior

The solution resistance was determined and compensated for using the in-built ZIR function of the potentiostat, compensating for 85% of the resistance. At all potentials tested, the potential was manually corrected for the remaining 15% using Ohm's law:

$$\Delta E = i * 0.15 * R$$

where R represents the calculated solution resistance, i the measured current, and ΔE the additional uncompensated potential shift felt by the working electrode.

2.3.6 GC quantification of gas products

Because all experiments were conducted under a batch setup, the calculation of Faradaic efficiencies and partial current densities for gas products could be calculated simply using the charge passed and a measured headspace according to the following relation:

$$F.E. = \frac{(ppm)(PV)(nF)}{Q(RT)}$$

where the *ppm* represents the measured concentration (by volume) of the analyte in the 1 mL sample, V represents the total headspace volume (typically 41 mL), P and T set by standard conditions (1 atm and 273.15 K), n the mole ratio of electrons to product formation from CO_2 (e.g. 8 for CH_4), Q the total charge in C passed, and F the Faraday constant. The partial current density could then be calculated by multiplying the *F.E.* for a given product by the total current density, or equivalently through the following relation:

$$j = \frac{(ppm)(PV)(nF)}{t(RT)}$$

where t represents the total time of electrolysis.

2.3.7 NMR quantification of liquid products

Liquid products were analyzed using quantitative nuclear magnetic resonance (qNMR) with a Bruker Avance 500 MHz instrument in a 9:1 mixture of sample to deuterium oxide with DMSO as an internal standard. Excitation sculpting was used to suppress the water signal, and each experiment consisted of 8 loops of 8 scans each with a delay time of 42 seconds to account for the long relaxation time of formate.

Because of the long delay time for each scan, the area ratio between an analyte peak and the DMSO peak should correspond well to the ratio of protons from the analyte and from DMSO, which in turn derives the concentration ratio of the analyte to the known concentration of DMSO. In addition, a calibration curve for formate, methanol, ethanol, and acetate was constructed by using the area ratio of known concentrations of analyte to the DMSO internal standard. Quantification of liquid products, especially formate, did not differ by more than 5% F.E. between these two methods. Finally, Faradaic efficiencies could be calculated as follows:

$$F.E. = \frac{[A](V)(nF)}{Q}$$

where *[A]* represents the concentration of analyte as determined by quantitative NMR and V the total volume of solution (typically 10 mL).

NMR samples from the anodic compartment were also taken, but no products, including formate or acetate, were observed. It is likely that Nafion, as a cation exchange membrane, restricts formate and acetate diffusion across compartments as may be observed for an anion exchange membrane.

2.4 Results and Discussion

2.4.1 Copper nanowires as an electrode for CO2RR

Figure 2.1a shows a transmission electron microscope (TEM) micrograph of the as-synthesized bare Cu NWs, which have a diameter of approximately 17 nm. The five-fold-twinned structure of the NWs with well-defined edges is illustrated in the inset. To test their catalytic behavior toward CO_2 reduction, freshly made Cu NWs were loaded onto carbon black (CB) to make a 20 wt% CuNW/CB catalyst suspension in hexanes, as confirmed by TEM (Fig. 2.1b). This suspension was pasted onto glassy carbon plates to make a working electrode, which scanning electron microscopy (SEM) revealed to be a conductive mesh of Cu wires and carbon black (Fig. 2.1c).

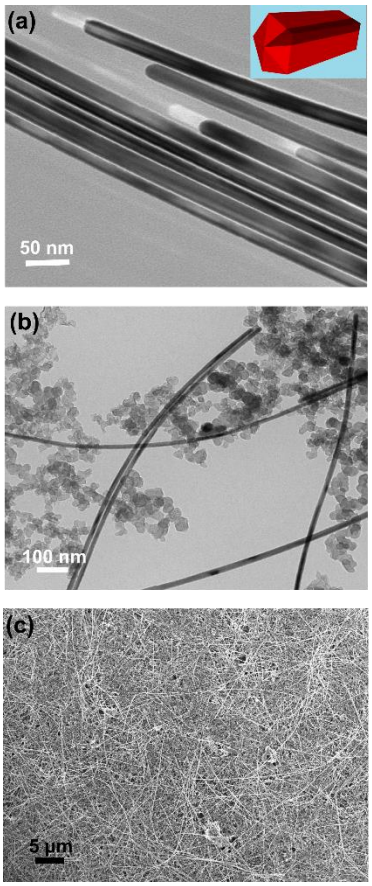

Figure 2.1. Synthesis of five-fold twinned copper nanowires. (a) TEM image of bare wires, around 20 nm in diameter, before loading. Inset: illustration of the five-fold twinned structure, showing a high proportion of low-coordination edge sites (dark red) brought about by five-fold twin boundaries. (b) TEM micrograph of Cu NWs loaded on carbon black with 20 wt% loading. (c) SEM micrograph of the CuNW/CB catalyst dispersed on a glassy carbon surface, used as the electrode for electrochemical experiments.

Direct loading of the Cu NW catalyst onto the glassy carbon substrate was also explored. It was found that while the catalytic activities between the CuNW/GC and CuNW/CB/GC electrodes were comparable, the latter formulation was more mechanically stable. Without carbon black, the Cu NWs visibly disappear from the electrode after 1 C of electrolysis (Figs. 2.2, 2.3).

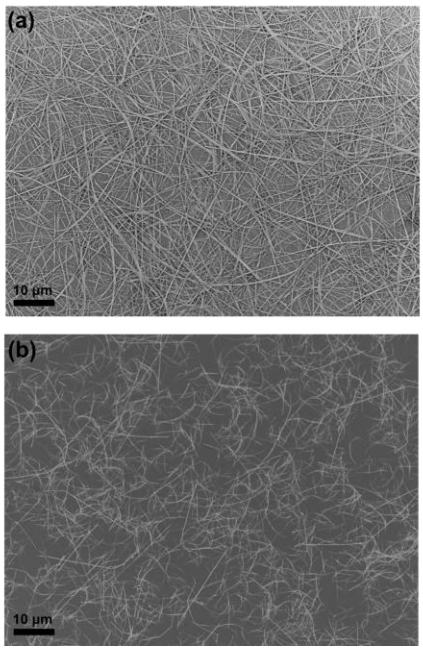

Figure 2.2. Comparison of Cu NW catalysts directly dropcast on a glassy carbon electrode before (a) and after (b) 1 C electrolysis at -1.25 V vs. RHE. In addition to a visible loss of catalyst material after electrolysis, the direct loading of Cu NWs results in significant bundling of wires.

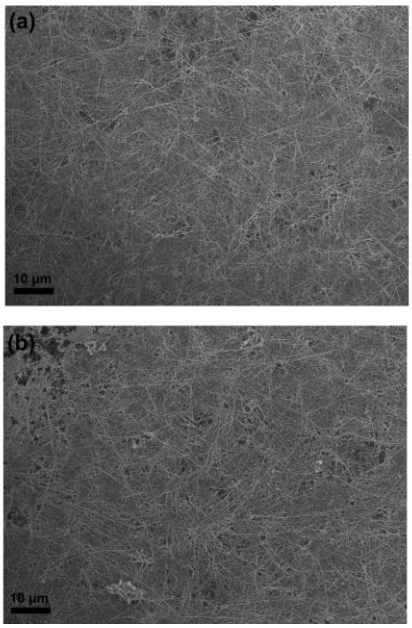

Figure 2.3. Comparison of Cu NW catalysts with carbon black loading on a glassy carbon electrode before (a) and after (b) 1 C electrolysis at -1.25 V vs. RHE. Dispersion with carbon black is observed to improve both catalyst adhesion and wire separation.

Thereafter, the CuNW/CB catalyst was tested over a range of potentials for catalytic activity, which showed a marked selectivity for methane at potentials more negative than -1.1 V

vs. RHE (Fig. 2.4a). Faradaic efficiencies (F.E.s) for methane at the potentials tested reached a maximum of 55% at -1.25 V vs. RHE. Notably, while polycrystalline copper has frequently been reported to produce a spread of C1 and C2 products at potentials below -1 V vs. RHE, the CuNW catalyst produces nearly exclusively methane among the carbon-derived products. In fact, in the potential region tested spanning 600 mV, neither carbon monoxide (CO) nor ethylene (C_2H_4) exceed 5% of all products, while formate is only substantially produced at potentials more positive than -1 V vs. RHE. Total F.E.s consistently reached 90-100% at potentials where methane was produced selectively (Fig. 2.4b), suggesting the successful detection of all major products at methane-selective potentials.

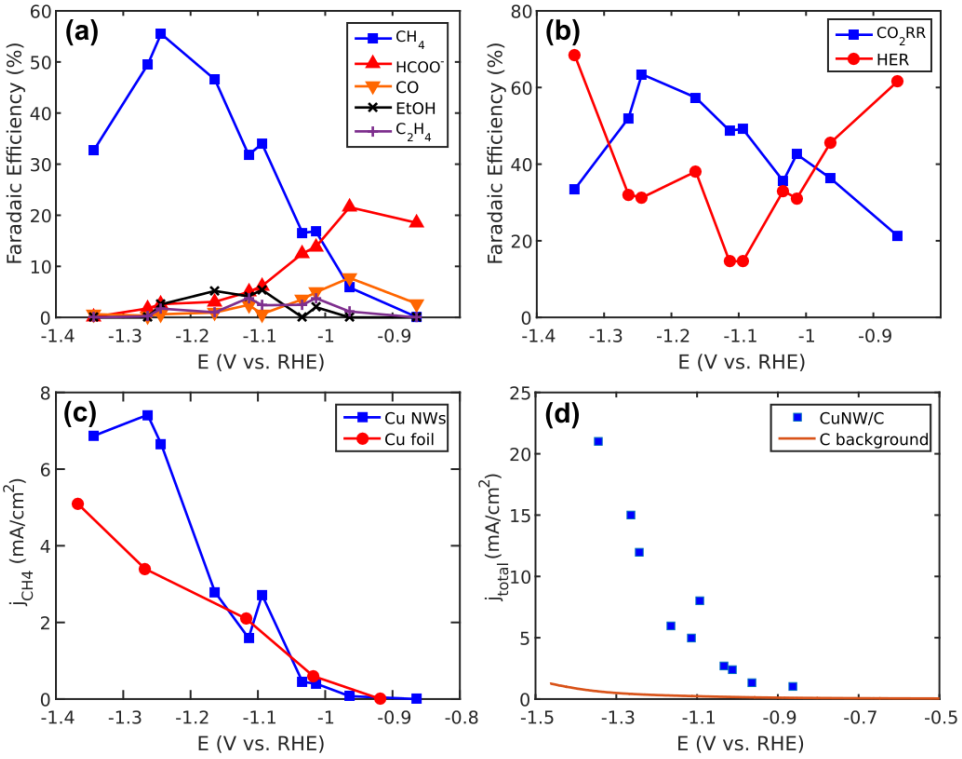

Figure 2.4. Cu NW initial electrocatalytic activity and selectivity. (a) Products of CO_2 reduction, showing the prevalence of CH_4 at high bias over other products (CO, C_2H_4, formate, and ethanol). Acetate, methanol, and n-propanol were detected in trace. (b) Total F.E. of CO_2RR and the competing reaction, hydrogen evolution (HER). (c) Partial current density towards methane of the Cu NW catalyst compared with a cleaned polycrystalline copper foil, showing the increased activity at more negative potential. (d) Total geometric current density over the range of potentials, compared to background current from the glassy carbon substrate with bare carbon black loaded. Initial activity electrocatalytic tests were conducted over the potential range of -0.85 to -1.35 V vs. RHE in 0.1 M $KHCO_3$ over 1 C of passed charge.

To more aptly gauge the activity of the catalyst towards methane, the partial current density towards methane (j_{CH4}) was also calculated and compared with a reference polycrystalline Cu foil. The corresponding measured j_{CH4} values for the Cu foil are within range of previous results.[25,36] Although j_{CH4} for the two catalysts is comparable at lower overpotentials, the CuNW-loaded

electrode achieves partial current to methane double that of Cu foil past -1.2 V vs. RHE (Fig. 2.4c). The background current contributed by the same mass of carbon black on glassy carbon was minimal even at the most negative potentials applied (Fig. 2.4d), confirming that the measured j_{CH4} is due to the Cu NW catalyst. Overall currents are relatively stable over electrolysis, but tend to be less so at higher potentials due to the large amounts of bubbles being produced which periodically block active surface area (Fig. 2.5).

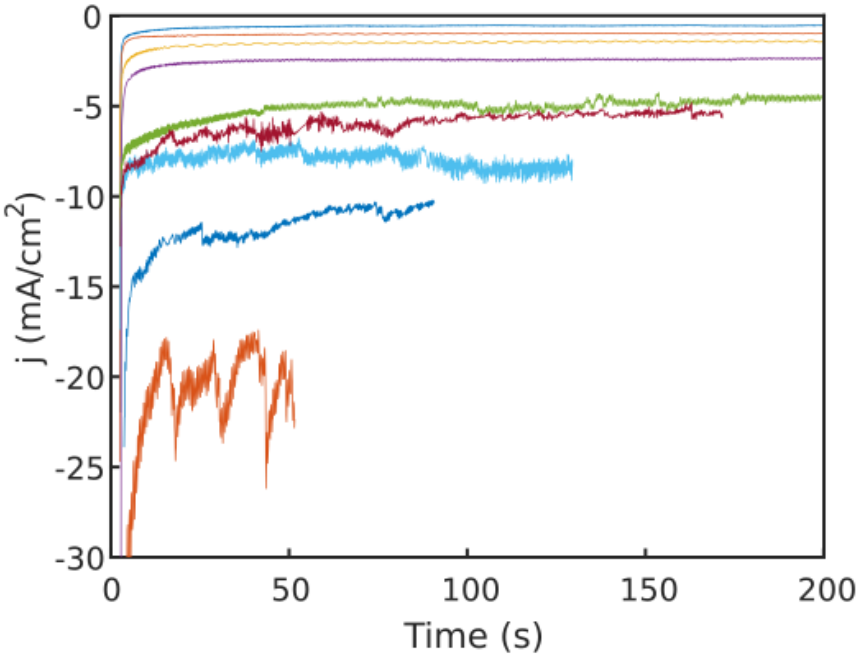

Figure 2.5. Typical i-t curves for 1 C electrolyses at various applied potentials. From top to bottom, the potentials shown here are -0.85, -0.95, -1.0, -1.05, -1.10, -1.15, -1.20, -1.25, and -1.35 (V vs. RHE). Electrolyses were stopped after 1 C of passed charge; thus, runs at more negative potentials (higher current) were conducted in a shorter amount of time. The curves are truncated at 200 s for visual clarity when comparing with the much shorter electrolyses at higher bias.

2.4.2 Evolution of copper nanowires in activity and structure

Electrocatalytic activity was also measured with varying amounts of passed charge before product measurement. Most products (such as CO, H_2, and liquid products) were not observed to change substantially over this period (Fig. 2.6).

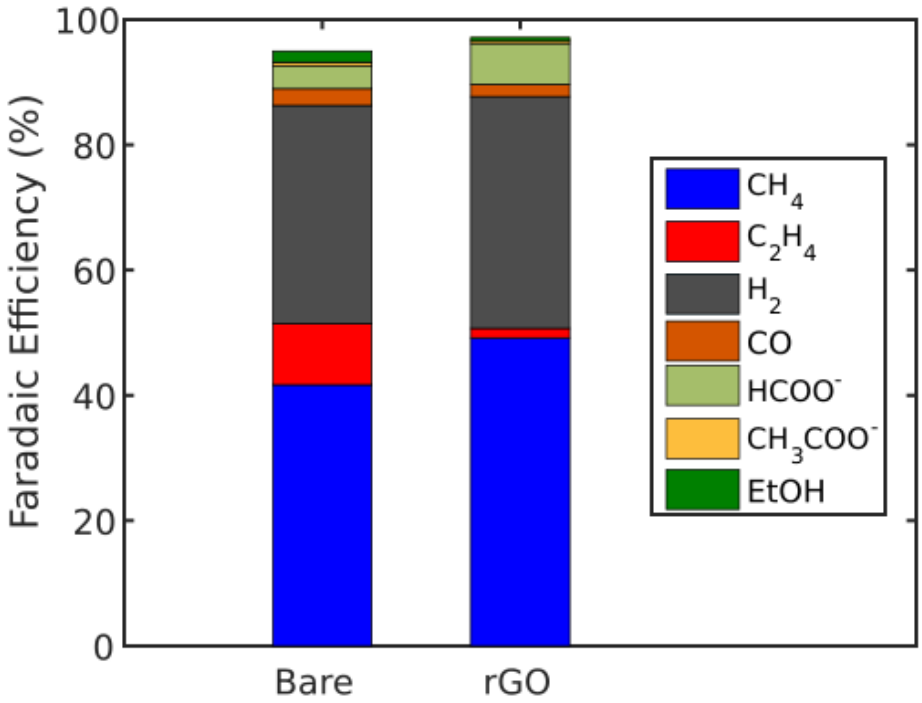

Figure 2.6. Full product comparison of bare vs. rGO wrapped Cu NWs after 5 C passed at -1.25 V vs. RHE. All products are shown here for 5 C of electrolysis, compared between the bare Cu NW and the rGO-wrapped Cu NW. Slight shifts in selectivity for H_2 and formate are observed, while the overall selectivity for EtOH and acetate is too small in both samples to observe a change. Other liquid products such as MeOH and acetaldehyde were detected but could not be quantified due to their low concentration. The 10% selectivity change in the hydrocarbons is the most salient selectivity shift between the two samples. Total F.E.s exceeded 95% at this potential, confirming the detection of all products from CO_2RR.

Strikingly, however, the selectivity of the catalyst towards its main product methane was observed to change with increasing charge passed at -1.25 V vs. RHE (Fig. 2.7a). Coulomb-by-Coulomb analysis of the activity evolution shows that the hydrocarbon selectivity shifts from almost entirely CH_4 to higher production of C_2H_4 over the course of 5 C passed.

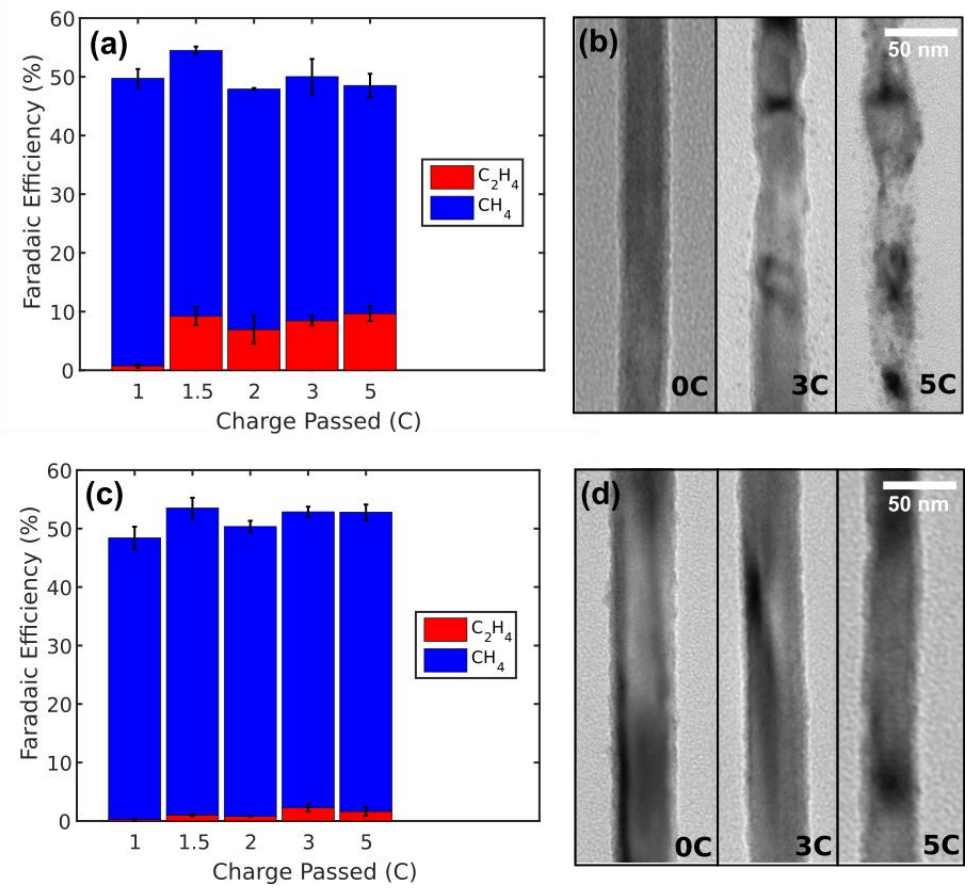

Figure 2.7. Electrocatalytic and morphological evolution of the Cu NW catalyst. (a) Rapid onset of C_2H_4 formation with a concurrent decrease in CH_4 activity after the first Coulomb of electrolysis. (b) Representative Cu NWs imaged under TEM after a given amount of charge passed, showing visible fracturing and the formation of small Cu NPs. (c), (d) Analogous electrocatalytic and morphological characterization for the rGO-Cu NW catalyst, showing preservation of selectivity as well as morphology.

The shift in selectivity appears shortly after the first Coulomb passed. This change in activity suggests that the catalyst is rapidly evolving at potentials relevant to hydrocarbon formation. TEM confirms that the morphological of the catalyst changes as a function of charge passed during electrolysis. For example, Figure 2.7b shows that after 1 C, the wire morphology begins to degrade, resulting in particle formation, wire bundling, disintegration, and fracturing.

2.4.3 Preservation of copper nanowires by reduced graphene oxide wrapping

To investigate whether the structure of a wire could be preserved, thereby also preserving the CO_2 electrocatalytic selectivity for methane, we studied the electrocatalytic properties of rGO-wrapped copper nanowires. Wrapped Cu NWs were loaded on carbon black and glassy carbon under identical loading conditions to the bare Cu NWs and tested for CO_2 electrocatalytic activity. Figure 2.7c shows analogous electrocatalytic and TEM results to Figure 2.7a-b using the rGO-wrapped CuNWs/CB catalyst. In contrast with the bare wires, rGO-wrapped wires preserve their

selectivity for methane over ethylene for up to 5 C passed. The remainder of products are shown in Fig. 2.6.

Simultaneously, the wires show no morphological evolution under TEM. Typical single wires were selected for Figure 2.7b and 2.7d to highlight the morphological difference between rGO-CuNWs and bare CuNWs under bias. TEM micrographs imaged at varying points of the electrolysis for each catalyst in the ensemble corroborate this observation at large (Figs 2.8, 2.9).

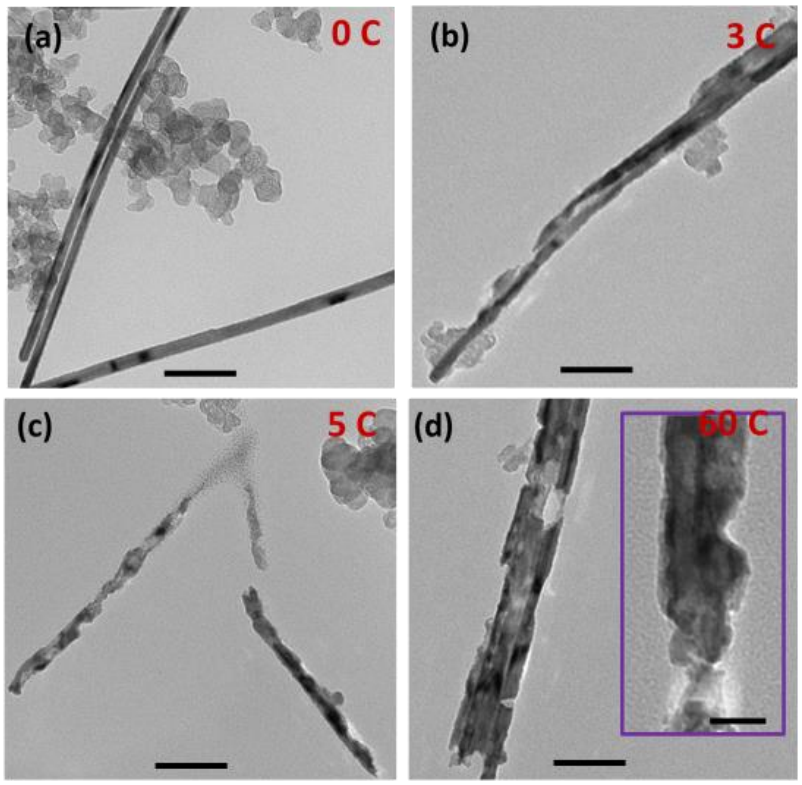

Figure 2.8. Large-area TEM micrographs of bare copper nanowires (a) before electrolysis and after (b) 3C, (c) 5C and (d) 60 C of electrolysis**.** Scale bar is 100 nm. Inset picture of (d) shows a larger-magnification TEM micrograph of a single copper nanowire after 60 C of electrolysis. The scale bar is 20 nm. During electrolysis, the bare Cu NWs are observed to dissolve, bundle, fracture, and form small Cu NPs.

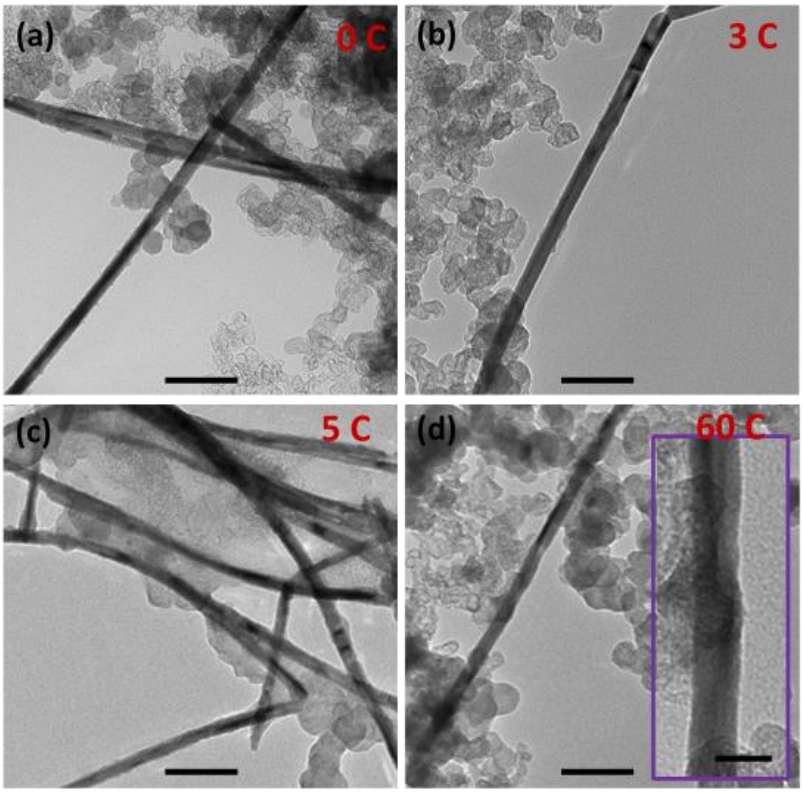

Figure 2.9. Large-area TEM micrographs of rGO-wrapped copper nanowires (a) before electrolysis and after (b) 3C, (c) 5C and (d) 60 C of electrolysis. Scale bar is 100 nm. Inset picture of (d) shows a larger-magnification TEM micrograph of a single rGO-wrapped copper nanowire after 60 C of electrolysis. The scale bar is 20 nm. The morphology of the copper nanowires are well maintained even after 60 C of electrolysis, for which the catalytic product distribution could not be reliably measured under a batch setup due to CO_2 depletion.

To verify the presence of rGO on the surface of the catalyst, we conducted Raman spectroscopy on the rGO-CuNW catalyst pre- and post-electrolysis. Both before and after 5 C of electrolysis, Raman spectra of the rGO-CuNW exhibit the characteristic *D* and *G* bands of GO or rGO (Fig. 2.10a).[98]

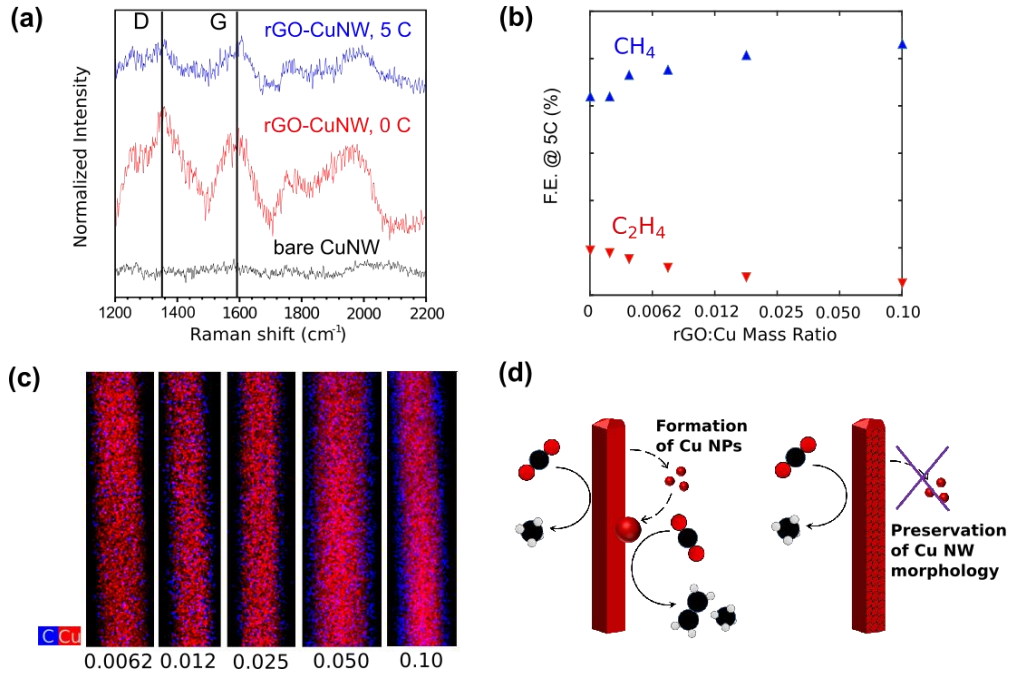

Figure 2.10. Evidence for the protective role of reduced graphene oxide. (a) From bottom to top, Raman spectra of bare CuNWs, GO-wrapped CuNWs before electrolysis, and rGO-wrapped CuNWs after electrolysis. The D and G peaks attributable to graphene oxide are indicated, showing its presence and retention after 5 C electrolysis. (b) CH_4 and C_2H_4 selectivity at 5 C on Cu NWs wrapped with varying amounts of GO used in preparation, showing preservation of CH_4 selectivity with increasing rGO wrapping. (c) EDS mapping showing the increasing presence of carbon species attributed to graphene oxide surrounding the wires as the amount of GO used in preparation of the catalyst is increased. (d) Scheme for the correlation between morphology and selectivity observed in this study. C_2H_4 onset is thought to be due to the transformation of NW edge sites to small NPs deposited on the surface (left), which rGO wrapping prevents (right).

For comparison, a Raman spectrum of the unwrapped wires is shown, which exhibits no peaks attributed to rGO. Wrapped Cu NWs with varying amounts of rGO were then used as electrodes for CO_2 electroreduction to probe whether increasing rGO wrapping better preserves electrocatalytic selectivity. Figure 2.10b shows that increasing the amount of rGO wrapping on the wires increasingly preserves high methane selectivity over ethylene over 5 C of electrolysis. Energy dispersive X-ray spectroscopic (EDS) mapping of carbon further verifies the presence of rGO on the surface of the Cu NWs, and that increasing the mass ratio of GO to copper used in the preparation qualitatively increases the amount of rGO wrapping in the final catalyst (Fig 2.10c).

2.5 Conclusions and Perspective

Taken together, these data suggest that nanowire-specific structural features, such as edge sites, are responsible for stabilizing intermediates that lead to improved methane selectivity in CO_2 electroreduction. The five twin boundaries on the ultrathin Cu NW present a unique active site for stabilizing CO_2 intermediates, which previous DFT studies have suggested enhance methane

formation.[99] As the wires evolve under bias, the well-defined twin boundaries degrade, while Cu nanoparticles simultaneously nucleate on the NW surface and create a variety of ill-defined active sites. The shift in selectivity from methane to ethylene shown here is approximately 10% F.E., such that the final ethylene selectivity at -1.25 V vs. RHE is comparable to previous reports of ethylene selectivity for polycrystalline copper foil.[25] However, it is difficult to identify the active site of the evolved catalyst, as it consists of a diverse array of roughened wires, small particles, and likely some remaining twin boundaries, all of which exhibiting distinct catalytic selectivity. The tunability of electrocatalytic selectivity with amount of rGO directly supports the role of rGO in preserving structure and selectivity. Figure 2.10d summarizes the effects of changing and preserving morphology on electrocatalytic selectivity: copper nanoparticle formation and edge loss shifts the morphology from high-density methane-selective sites to a mix of methane-selective and mixed-selectivity sites. Introducing rGO as a wrapping layer impedes nanoscale structural change and prevents the loss of methane-selective sites.

On the other hand, because the wrapping process is fairly non-discriminatory across copper sites, a consequence of the strategy is that the overall activity will decrease. Figures 2.11 and 2.12 depicts how the total electrocatalytic current diminishes as the wrapping extent is enhanced; therefore, despite preservation of selectivity, the wrapping process reduces overall turnover towards methane. Further refinement of this process would target how specifically active surfaces (*e.g.* the hypothesized twin boundary edge sites) could preferentially exposed.

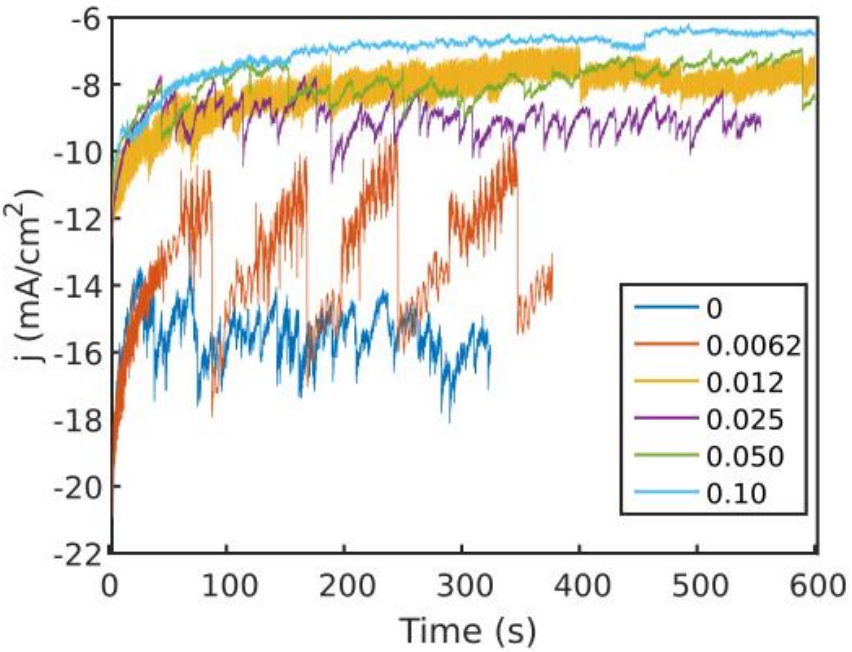

Figure 2.11. Current-time behavior of rGO-wrapped Cu NWs with varying degrees of wrapping, measured at -1.25 V vs. RHE for 5 C of electrolysis. The curves are truncated at 600 s for visual clarity. As with Fig. 2.5, electrolyses tended to be more stable at lower currents due to bubble formation, resulting in larger, difficult-to-control fluctuations of exposed surface area.

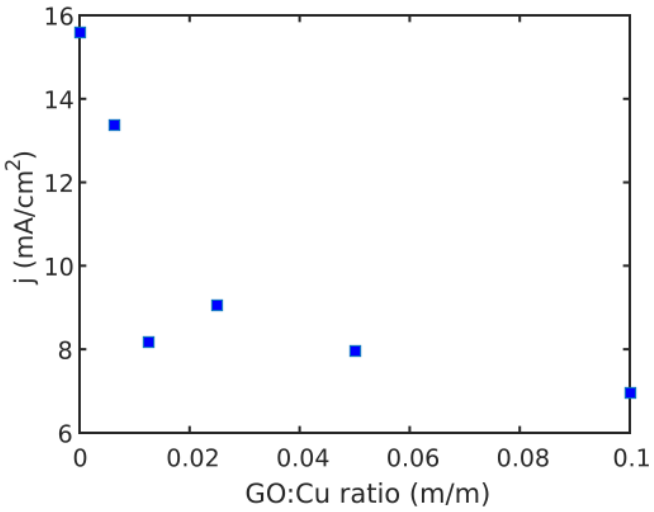

Figure 2.12. Decreasing total steady-state current density with increased wrapping. The current density was observed to decrease with an increase of the rGO:Cu ratio used during wrapping. This observation is consistent with a blockage of active sites due to the GO, further confirming the active presence of GO on the exterior of the wire.

In addition, the long-term overall stability for this catalyst, along with others reported in the literature, suffers due to the formation of methane eventually causing buildup of poisoning species on the surface of copper (Fig. 2.13). Thus, the rGO-CuNW platform is ultimately not a desirable catalyst for long-term stable electrocatalytic conversion of CO_2 to methane. However, the system still represents an intriguing probe of surface sensitivity and structural stability alongside catalytic selectivity.

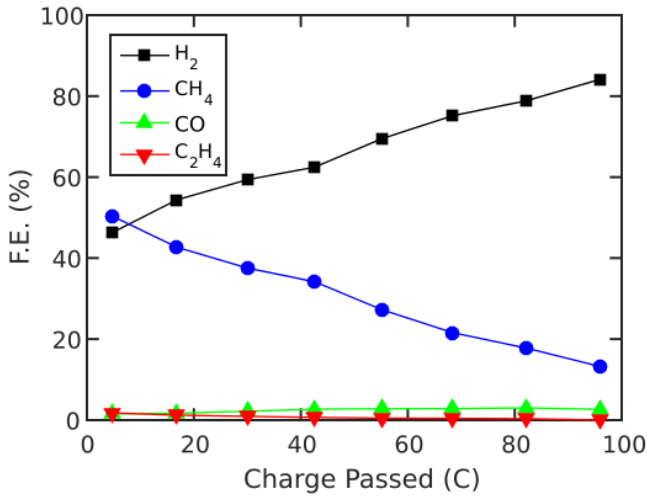

Figure 2.13. Long-term stability of electrochemical selectivity for the rGO-CuNW catalyst. Stability measurements were conducted under a flow-cell configuration in which gas samples were taken roughly every 20 minutes. Over the course of 3 hours, the activity for methane steadily decreases, while hydrogen evolution increases. However, the shift toward ethylene selectivity consistent with structural degradation does not occur, consistent with the morphological preservation observed in Figure 2.9. Previous studies have identified consistent, rapid deactivation

in catalysts that produce high levels of methane, which has been ascribed to poison species derived from key intermediates along the pathway to methane.[100] The steady deactivation of the rGO-CuNW catalyst over extended electroreduction is expected to occur for a similar reason, unlike the structurally-induced selectivity shifts highlighted in the main text.

In conclusion, I have shown that one-dimensional ultrathin five-fold twinned copper nanowires exhibit high methane selectivity for CO_2 electrocatalysis relative to other carbon products. The origin of the methane selectivity is likely due to the presence of a high density of edge sites owing to the twin boundaries. Furthermore, the morphology of these wires and their electrocatalytic selectivity evolve, losing methane selectivity in favor of ethylene formation. We posit that the change in electrocatalytic selectivity is due to the change in morphology, a claim directly supported by the observation that rGO wrapping simultaneously preserves morphology and methane selectivity over the same electrocatalytic conditions. Although this platform is ultimately not desirable for industrial applications, this study highlights the importance of manipulating nanostructural transformations of copper electrocatalysts under conditions relevant to CO_2 electroreduction, a topic that merits in-depth future study. Moreover, it demonstrates the employment of rGO wrapping as a strategy for electrocatalyst stabilization, a method that may be further explored and refined for other catalysts in which morphological change is evident.

Finally, an addendum. As I mentioned at the beginning of this chapter, the Cu NW system was originally developed to be a conductive transparent electrode as demonstrated in prior publications.[96] The use of this NW mesh as a conductive transparent CO2RR electrode can also be demonstrated by simply printing the NW mesh onto a transparent plastic substrate, as shown in Fig 2.14. Potential applications of such an electrode towards coupling with light absorbers are an interesting engineering consideration, but beyond the scope of this dissertation.

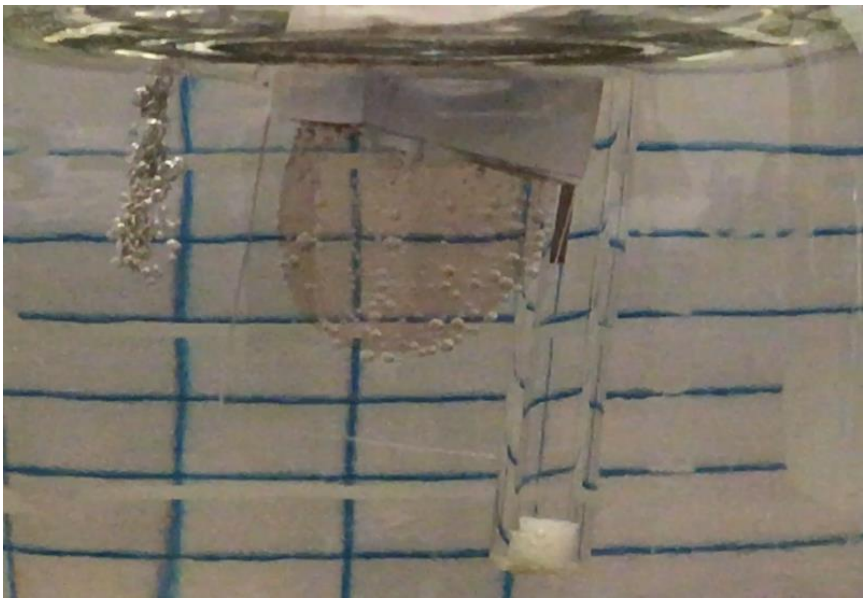

Figure 2.14. Demonstration of a conductive transparent flexible electrode for selective methane formation from CO_2 and water. Pictured is the Cu NW mesh printed onto a flexible transparent plastic (non-conductive) substrate. To the left, a Pt counter electrode, and to the right, a Ag/AgCl (1M KCl) reference electrode. Electrical contact is made using a Ag wire above the point of

immersion in electrolyte (not pictured). Formation of bubbles on both electrodes upon application of -1.2 V vs. RHE suggests a closed circuit forms with the NW mesh and electrolysis is successfully conducted, with the blue lines in the background (behind the reactor) clearly demonstrating the transparency of the electrode.

Chapter 3. Investigating the Active Surface of a Structurally Dynamic Copper Nanoparticle Ensemble

Much of the text in this chapter is adapted from "Electrochemically Scrambled Nanocrystals are Catalytically Active for CO_2-to-Multicarbons," Li, Y.*, Kim, D.*, Louisia, S., Xie, C., Kong, Q., Yu, S., Lin, T., Aloni, S., and Yang, P. *Proc. Natl. Acad. Sci. USA*, **2019**, In review.

3.1 Preface

As alluded to in Chapter 1, promotion of C-C bonds is one of the key fundamental questions in the field of CO_2 electroreduction. Despite a wealth of copper-based catalysts studied for CO_2-to-multicarbons (CO_2-to-C_{2+}), a clear identification of the structural motif linked to improving intrinsic C-C activity has yet to emerge. By closely probing a Cu nanoparticle (NP) ensemble catalyst active for CO_2-to-C_{2+}, we show that bias-induced rapid fusion or "electrochemical scrambling" of Cu NPs creates uniquely disordered structures intrinsically active for low overpotential C_{2+} formation. This unprecedented state, confirmed by an arsenal of *ex situ* and *in situ* methods, exhibits around 7-fold enhancement in C_{2+} turnover over crystalline Cu and high-performance oxide-derived catalysts, with a distinctive transition to single-crystal Cu_2O cubes upon air exposure. These results emphasize that electrochemical nanocrystal scrambling accesses a unique state with a high degree of catalyst disorder that facilitates C-C bond formation from CO_2.

3.2 Introduction

Structural evolution of materials under operation is a topic of emergent importance in the field of heterogeneous catalysis.[101] Since nanoscale catalysts are highly susceptible to structural changes due to their high surface area and energetics, growing awareness of this phenomenon has led to deeper understanding of catalysis from a spectrum of works in both gas and liquid phase [70,101,102]. The catalytic relevance of such dynamics to CO_2 electrocatalysis has recently been highlighted in copper-based systems [53,74,103,104].

Understanding the surface requirements of copper to promote CO_2 electroconversion to multicarbon products (CO_2-to-C_{2+}) is crucial for the development of catalyst materials in the field. With copper as the sole material to demonstrate CO_2-to-C_{2+} at reasonable rate and efficiency,[21] a host of high-activity copper catalysts have shown promise in achieving high C_{2+} activity/selectivity in bulk product formation rates.[54,56,65,66,105–108] However, the *intrinsic* CO_2-to-C_{2+} activity (*e.g.* $\mu A_{C2+}/cm^2_{Cu}$) of these catalysts has only been observed to marginally improve against a typical copper foil surface thus far, suggesting that nominal activity enhancements are inextricable from the modulation of extrinsic factors, such as local pH or mass transport, through catalyst microstructure.[21] Hence, despite many investigations into the structural and/or compositional origin of CO_2-to-C_{2+},[42,59,60,64–66] a clear identification of a core structural variable that correlates with and directly influences the *intrinsic* CO_2-to-C_{2+} activity has yet to emerge.

Recently, we reported the structural transformation of a copper nanoparticle (Cu NP) ensemble into cuboidal structures, coupled with selective electroconversion of CO_2 to multicarbons at lowered overpotentials.[109] The observed coalescence of NPs towards distinct shape formation and desirable catalytic performance, in contrast to conventional sintering and

deactivation, warrants a close study of the electrochemical evolution process. In light of both the prevalence of structural dynamics on copper nanocatalysts and the importance of understanding structural effects on intrinsic activity, such work may enable directed evolution strategies as new avenues to electrocatalyst development for CO_2 utilization.

In this work, we probe the structural transformation process of the previously reported Cu NP ensembles under CO_2 electroreducing conditions. By closely tracking the material state over electrolysis, a unique *ex situ* structural signature (*i.e.* single crystalline oxide nanocubes) of the C_{2+}-active catalyst is identified and confirmed to be catalytically relevant. Crucially, the *ex situ* signature is determined not to exist under CO_2-reducing conditions, suggesting that the *in situ* metallic active species are highly unstable upon removal of bias. Chemical passivation to preserve the *in situ* structure allows their full quantitative characterization as C_{2+}-active copper nanostructures with enriched disorder. This state of copper boosts the intrinsic C_{2+} activity by 7-fold over the crystalline counterpart and previous state-of-the-art catalysts, resulting in a direct experimental determination of a necessary structural characteristic for enhancing CO_2-to-C_{2+} turnover. Therefore, we show how Cu nanoparticle dynamics result in a unique and highly active catalyst state efficient for C-C formation, providing broader fundamental insights for CO_2-to-C_{2+} and raising the prospect of structural dynamics as an approach to catalyst design.

3.3 Materials and Methods

3.3.1 Nanoparticle synthesis and electrode fabrication

7 nm copper nanoparticles were synthesized as previous reported.[109] For larger size nanoparticles, size was controlled by tuning the mole ratio of tetradecylphosphonic acid (TDPA) to copper(I) acetate (CuAc), where higher ratio resulted in larger particles. Specifically, to synthesize 7, 9, 14, and 20 nm nanoparticles, ratios of 0.5, 0.7, 1, and 1.25 respectively were used while maintaining the absolute concentration of CuAc (1 mmol).

Nanoparticle concentrations by mass of copper were measured by inductively-coupled plasma optical emission spectroscopy, after which 68.9 μg of copper was deposited on 1 cm^2 area of carbon paper (Sigracet 29AA, Fuel Cell Store) to make working electrodes. Larger nanoparticles were deposited in a similar manner with identical mass loading.

For electrochemically grown Cu_2O nanocubes, a square wave voltammetric pulse program was employed as reported previously. Cu_2O nanocubes were directly grown on carbon paper (Sigracet 29AA).[110]

For copper foil derived electrodes, copper foil (Alfa Aesar 99.9999%) was electropolished in 85% H_3PO_4 at 3 V for 3 minutes against a copper counter electrode. Electrochemically-cycled oxide-derived copper was then fabricated following the method previously reported for EC-Cu.[65]

3.3.2 Electrochemical evolution of NPs and catalytic activity measurements

The customized electrochemical setup used to carry out bias-induced evolution of NPs and catalytic testing has been described previously.[109] All electrochemical measurements were made against a 3 M KCl Ag/AgCl reference electrode (World Precision Instruments). For all biasing experiments, the bias was applied directly without a prior linear sweep. Evolution was typically carried out by directly applying -1.2 V vs. Ag/AgCl, while catalytic results were measured at -1.45 V vs. Ag/AgCl. These potentials were considered equivalent by the steady-state structure made,

as elaborated upon in Fig. S3. All chronoamperometry was corrected with 85% of the solution resistance (Biologic), with the remaining 15% corrected afterward, as detailed in Chapter 2. Gas and liquid products were measured by a gas chromatograph equipped with TCD and FID-methanizer (SRI) and NMR with water suppression (Bruker Avance 500), respectively, as detailed in Chapter 2.

For pulsed preparation of Sample P, the potential was varied between -1.2 V vs. Ag/AgCl and 0.0 V vs. Ag/AgCl with periods of 2.5 s each. This pulse program was repeated 240 times, for a total of 1200 s of bias, before the potential was immediately switched to -1.45 V vs. Ag/AgCl for catalytic testing.

Passivation with benzotriazole (BTA, Sigma-Aldrich 99%) was conducted after electrolysis by removing the electrode from the cell and, within a short period time, immersing the electrode in a pre-made 10 mL bath of BTA dissolved in CO_2-saturated 0.1 M $KHCO_3$. The amount of BTA was set to a mole ratio of 1000 mol BTA to 1 mol Cu (the maximum concentration shown in Fig. S21).

Lead underpotential deposition was conducted immediately post-electrolysis in a solution of 0.1 M $NaClO_4$, 10 mM $HClO_4$, and 3 mM $Pb(II)(ClO_4)_2$. Cyclic voltammetry in the Pb underpotential region was conducted at 10 mV/s six times, for which the cycles were confirmed consistent and the fifth scan was reported. The potentials are referenced against a 1.0 M KCl Ag/AgCl electrode.

3.3.3 *Ex situ* structural characterization

Electrodes were directly imaged by SEM (Ultra 55-FESEM), and samples were crushed into a fine powder for powder X-ray diffraction (Bruker D8). For TEM sample preparation, the carbon paper electrode was crushed into a fine powder and dropcast on a TEM grid, typically lacey carbon, from a dispersion in toluene. Low magnification TEM (Hitachi H-7650) was conducted at 100 kV, while HRTEM and STEM-EELS (Tecnai F20 UT) were conducted at 200 kV. NBED, along with additional HRTEM (JEOL 2100-F) were also conducted at 200 kV. XPS (Thermo Scientific K-Alpha) was measured using an Al Ka source with spectra collected at a pass energy of 20 eV and step size of 0.05 eV.

X-ray absorption spectroscopy experiments were conducted at ALS beamline 10.3.2 following previously reported procedures and specifications for Cu NPs.[111] For *ex situ* measurements, electrodes were biased in the typical manner and removed for measurement under ambient conditions. The XANES data processing, including linear combination fits (LCF), were conducted in Athena. Edge step normalization for each spectrum was performed by subtracting the pre-edge and post-edge backgrounds in Athena.

EXAFS data reduction was performed in Athena and EXAFS fitting was performed in Artemis according to previous procedures.[111] For fitting the EXAFS data of the various Cu samples, two FEFF models of Cu metal and Cu_2O were generated. They were made according to the well-known crystal structure (both face-centered cubic with respect to Cu) of the bulk materials. All Cu nanoparticles samples were fit using the first three single scattering paths and the collinear triple scattering path to the fourth shell from Cu metal, as well as the first O single scattering path in Cu_2O. Addition of the first Cu single scattering path in Cu_2O was required to fit the samples containing a more prominent oxide phase.

3.4 Results and Discussion

3.4.1 Remarkably sharp cuboids with unexpected crystal structure and composition

Colloidally synthesized Cu NPs (7 nm) were spread on carbon paper and biased in CO_2 electroreducing conditions for multicarbon production in an aqueous environment (0.1 M $KHCO_3$). The observed change by *ex situ* characterization is rapid and striking, with the appearance of sharp cubic structures on the order of seconds and the predominance of said structures on the order of minutes (Fig. 3.1a and Fig. 3.2).

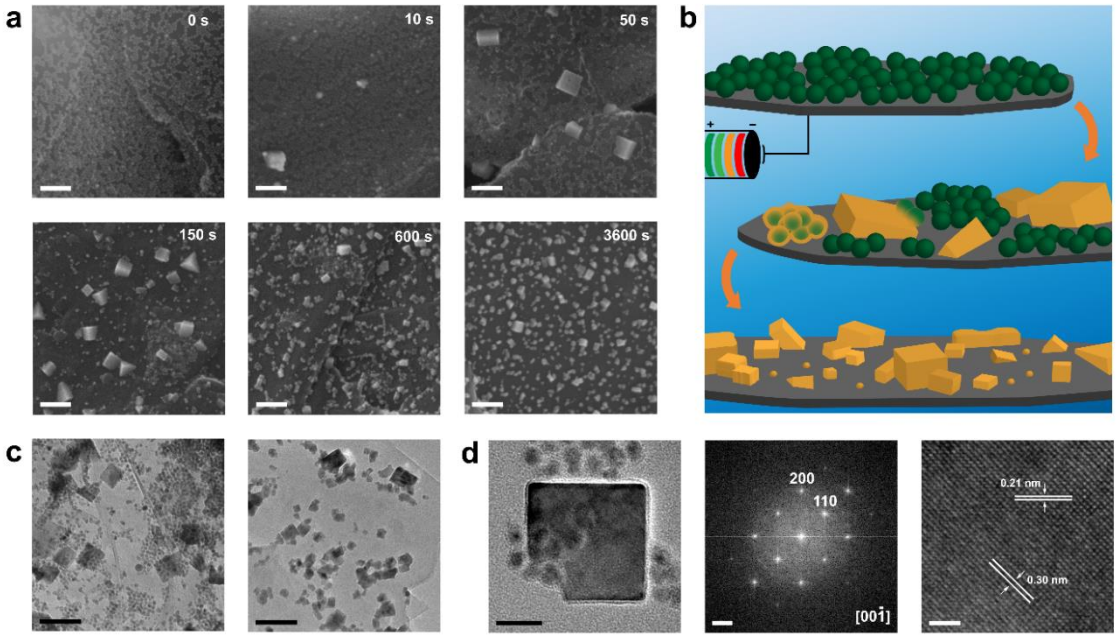

Figure 3.1. *Ex situ* electron microscopy of the Cu NP ensemble evolution timeline**.** (a) SEM after removing the electrode at various time points of bias (scale bars 100 nm). (b) Schematic of the structural evolution. (c) TEM (scale bars 50 nm) after 50 seconds (left) and 3600 seconds (right) of bias. (d) HRTEM (scale bar 10 nm) of a single Cu_2O cube at 50s with FFT showing Cu_2O reflections (scale bar 2 nm^{-1}) and a selected region at higher magnification (scale bar 2 nm). Electrochemical conditions are -0.6 V vs. RHE in 0.1 M $KHCO_3$ at 1 atm CO_2.

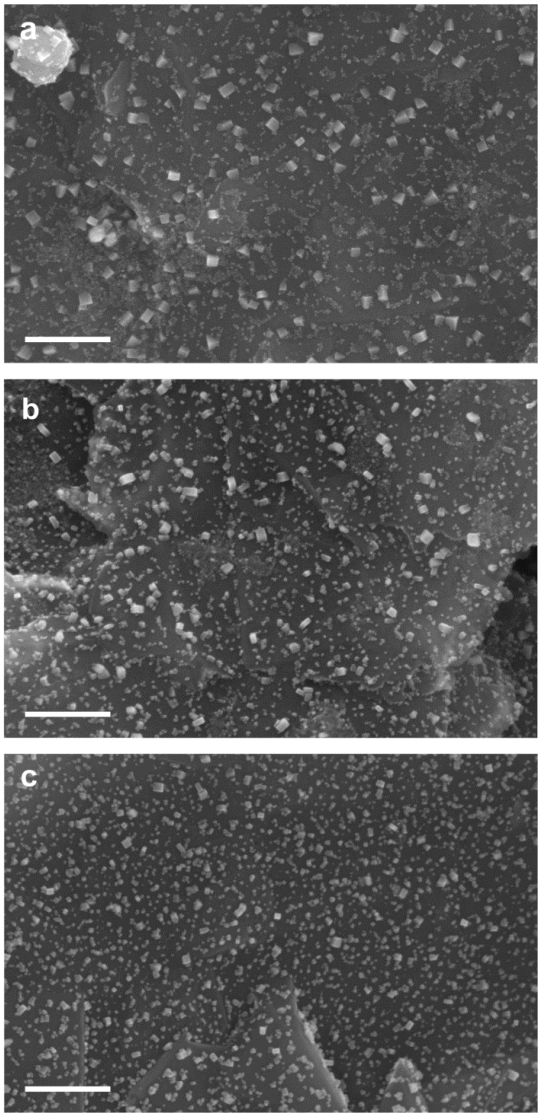

Figure 3.2. Additional scanning electron micrographs with expanded field of view at (a) 150s, (b) 600s, and (c) 3600s, demonstrating the generality of observed structures shown in Figure 3.1. Scale bars 200 nm.

More negative potentials resulted in a more rapid evolution process (Fig. 3.3). Regardless, the evolution of NPs under these biases eventually resulted in identical catalysts by both their morphology and catalytic activity (Fig. 3.4).

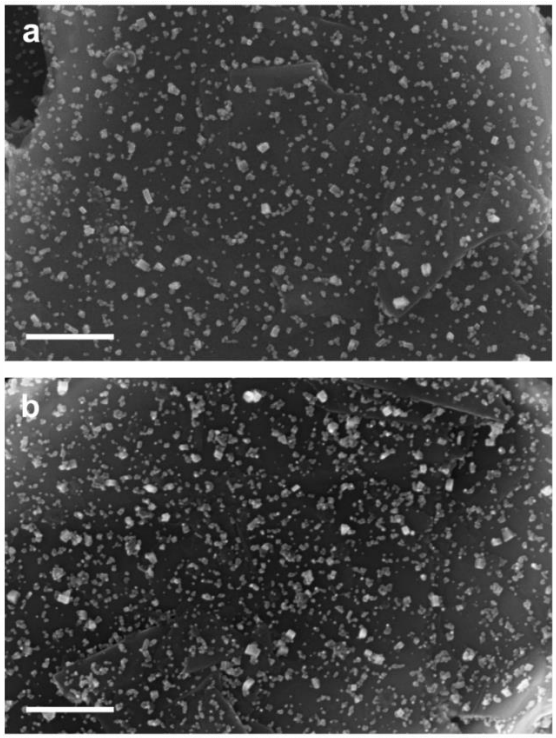

Figure 3.3. At an applied potential of -0.8 V vs. RHE, scanning electron micrographs of the catalyst at 50s bias (a) already bears many features indicative of the steady state (b), which in turn resembles the steady state at -0.6 V vs. RHE. Scale bars 200 nm.

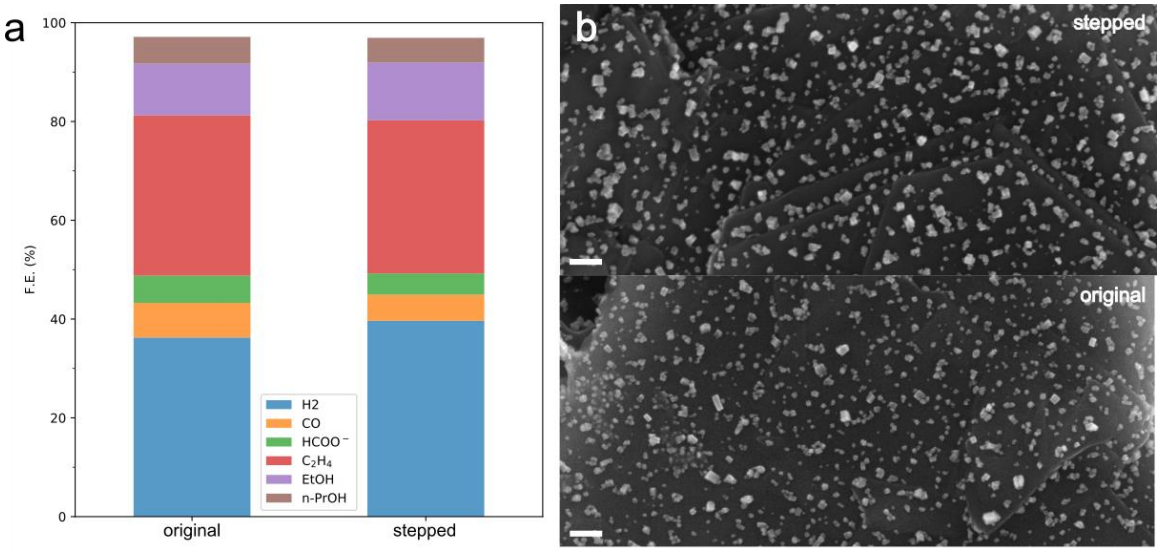

Figure 3.4. An electrode created at -0.6 V vs. RHE and then stepped to -0.8 V vs. RHE for catalytic testing exhibits the same activity (a) and steady-state structure (b, scale bars 100 nm) as the electrode directly biased at -0.8 V vs. RHE and tested for catalytic performance. Because both activity and structure are indistinguishable under the two paths employed, it is surmised that the catalyst created at -0.6 V vs. RHE has the same active surface as that created at -0.8 V vs. RHE. Minor multicarbon products are omitted from the column graph.

Qualitatively, the evolution is described by the loss of original nanoparticles, being gradually replaced by cubic and cuboidal structures (Fig. 3.1b). The formation of sharp cubes (Fig. 3.1c) is surprising given that the original NPs are spherical and exhibit 5-fold twinned Cu (Fig. 3.5).

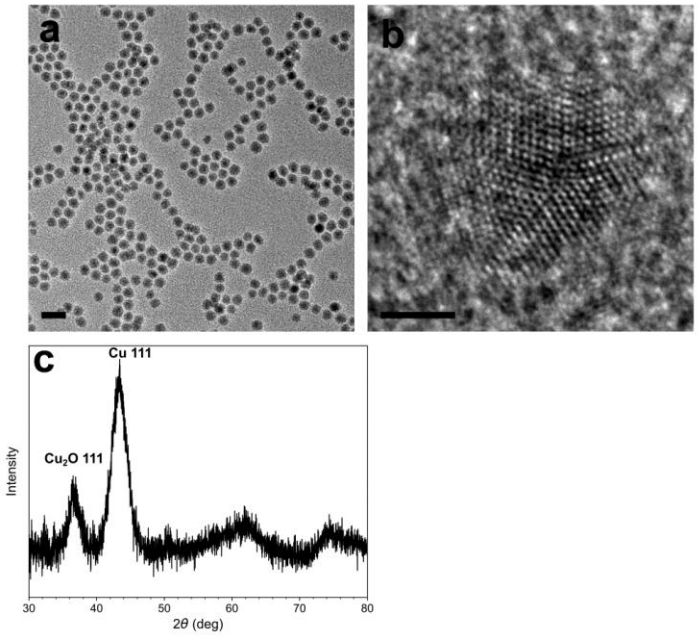

Figure 3.5. Characterization of the initial 7 nm copper nanoparticles by (a) TEM (scale bar 20 nm), (b) HRTEM (scale bar 2 nm), and (c) XRD. The nanoparticles are of uniform size (7 nm) and exhibit 5-fold twin polycrystallinity by HRTEM, resulting in broad diffraction peaks. The particles also contain a thin oxide shell that is inevitable for copper.

Furthermore, high-resolution transmission electron microscopy (HRTEM) reveals that these cubes are single-crystalline Cu_2O (Fig. 3.1d). These observations are beyond the irregularly shaped structures typically expected from nanoparticle coalescence.[36,112] The copper appears to redistribute over the course of evolution, such that at intermediary time points when many particles have transformed, the resultant cubes are smaller and more uniformly spread. Indeed, the 10-20 nm particles at later times are characterized as monocrystalline Cu_2O cuboids as well (Fig. 3.6).

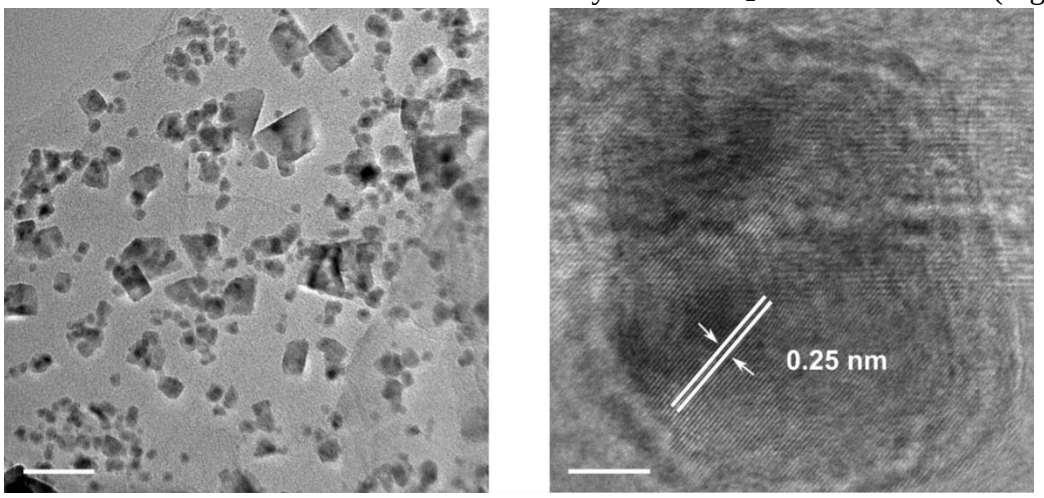

Figure 3.6. TEM (left, scale bar 50 nm) and HRTEM (right, scale bar 5 nm) of the catalyst after 600s of bias at -0.6 V vs. RHE. Many of the smaller (~10 nm) structures whose shape cannot easily be resolved by SEM are also cuboidal. HRTEM of one of these structures reveals an extended crystalline domain with spacing 0.25 nm, consistent with Cu_2O (111) and inconsistent with any Cu interplanar spacing.

The prevalence of these structures with high crystallinity is confirmed on the ensemble by X-ray diffraction, most clearly seen at early time points (Fig. 3.7). The Cu_2O cubes grow with no preferred orientation on the graphitic support (Fig. 3.8), suggesting the absence of interaction with the support as part of the process.

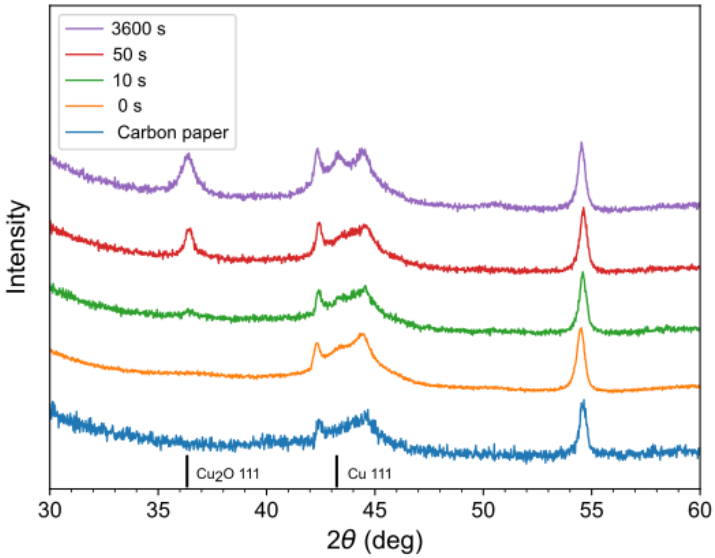

Figure 3.7. XRD of the full electrode at various time points. The growth of the sharp Cu_2O 111 peak is observed early on during the evolution. Additional peaks come from the graphite background used as an electrode support (bottom blue curve).

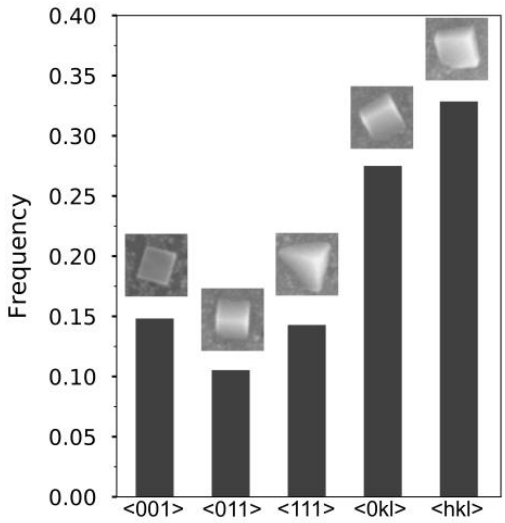

Figure 3.8. Statistics of the perceived "growth direction" of the oxide cubes relative to the graphitic support. Cuboidal structures in the early stage (50 and 150s) are categorized according to their symmetry and counted (n = 560). Of the three "low-index" growth directions, no clear preference is observed. Many of the structures are grown in some arbitrary "high-index" direction normal to the 0001 plane of the graphitic support, further reinforcing a lack of preferential interaction with the graphite.

3.4.2 Electrode-scale quantification of composition through XANES and LCF

To quantitatively assess the evolution of metal/oxide phase distribution, *ex situ* X-ray absorption near-edge structure (XANES) spectra at the Cu K-edge were deconvolved with linear combination fitting (LCF) using known phases. The XANES of the original Cu NPs was used alongside Cu^0 and Cu_2O standards for a 3-component LCF at early time points (Fig. 3.9a).

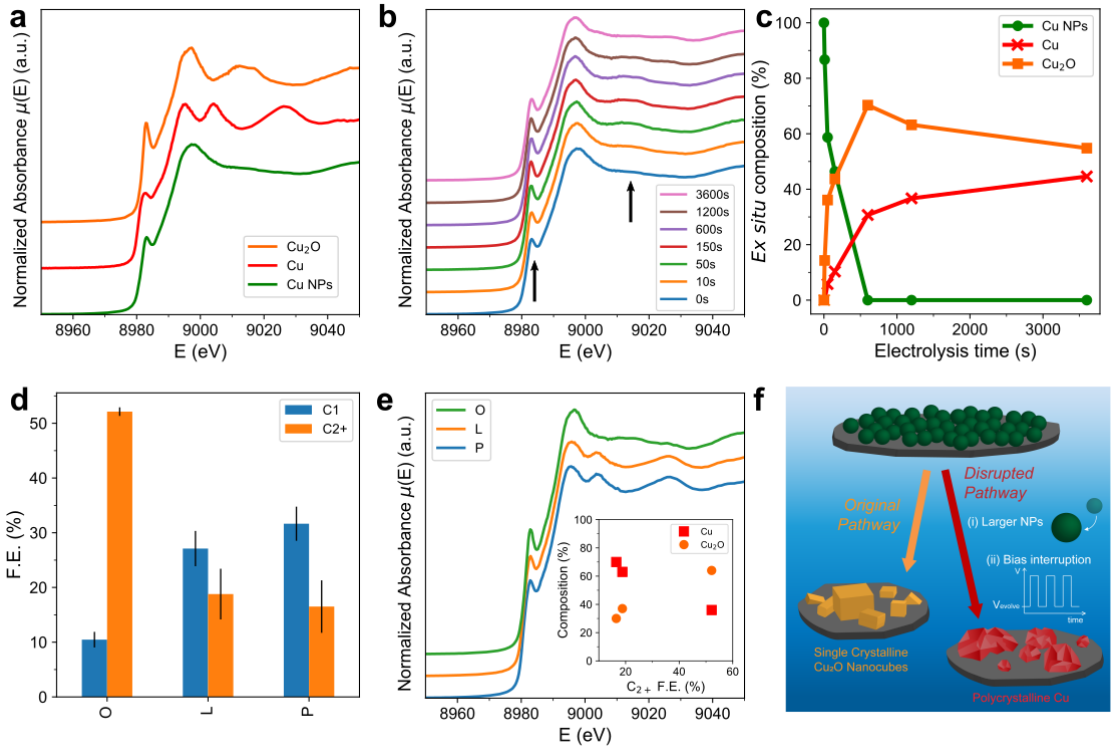

Figure 3.9. *Ex situ* X-ray absorption near-edge spectroscopy of catalysts. (a) Three standards used in this work: Cu, Cu_2O, and 7 nm Cu NPs. (b) XANES time series over electrolysis time *ex situ* with arrows indicating Cu_2O features. (c) Shift in composition tracked by LCF. (d) Catalytic selectivity for C_1 and C_{2+} products in samples O, L, and P (error bars 1 SD, n = 3). (e) XANES of O, L, and P, with inset showing the correlation of phase composition and C_{2+} selectivity. (f) Scheme summarizing the catalytic relevance of the Cu_2O structures observed uniquely in Sample O.

The Cu NPs are suitable as a phase component as they are observed at those times, and their XANES exhibits unique features (Fig. 3.10). The relative phase portions were extracted from the XANES spectra as the evolution proceeds (Fig. 3.11).

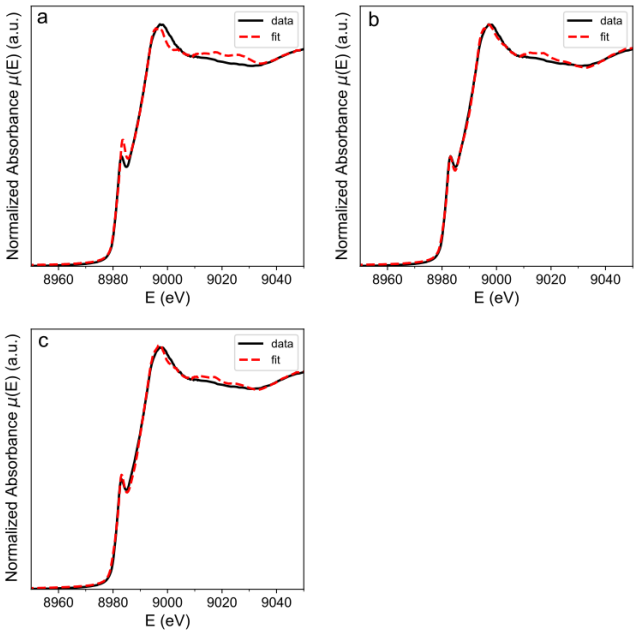

Figure 3.10. XANES of original Cu NPs with LCF fitting using three different choices of basis: (a) Only Cu and Cu_2O; (b) Cu, Cu_2O, CuO; (c) Cu, Cu_2O, hydrated Cu_3PO_4 (as a first order approximation of the phosphonic acid ligand coordination to the surface). No matter the choice of components, a satisfactory fit for the Cu NPs cannot be achieved. Size effects on metal nanoparticle XANES are known to be unpredictable and complex owing to a high percentage of surface atoms,[113] which is the likely main contributor to the unique features observed in these XANES. Thus, the NPs are considered to be a unique phase in the context of XANES LCF within this work, so long as the structures are observed to exist by corroborative techniques such as TEM and SEM.

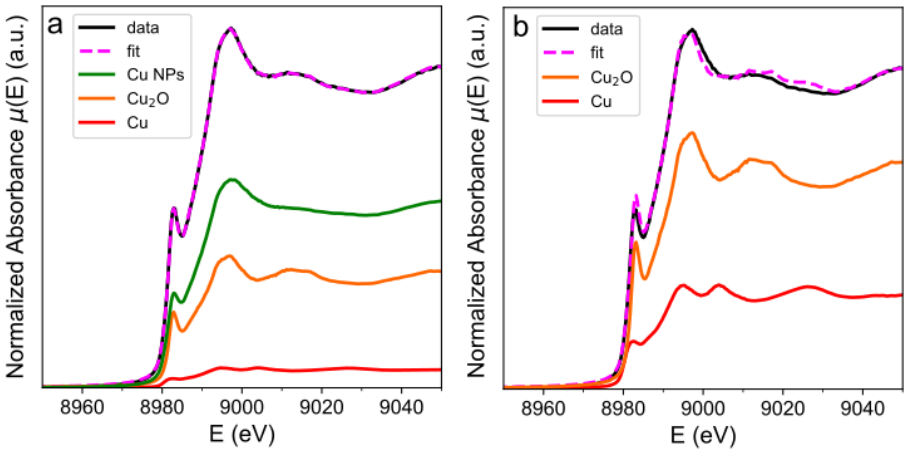

Figure 3.11. An example of the LCF method employed in this work. The 50s time point here is selected as being representative of the general approach: components of Cu, Cu_2O, and Cu NPs are assigned to and multiplied by varying weights, which together sum to a simulated XANES (dashed pink) that matches the observed data (solid black) well. The weights then represent the

proportion of the sample comprising each phase. In (a), the success of a three-phase fit including the Cu NPs is contrasted against (b), where a two-phase fit omitting Cu NPs results in an unsatisfactory fit for an early-stage sample with high amounts of Cu NPs as observed by SEM.

Cursory analysis of the time series (Fig. 3.9b) shows a rapid increase in intensity of the rising edge $1s \rightarrow 4p_{x,y}$ shake-down feature (~8984 eV) and a fingerprint crest (~9015 eV) indicative of Cu_2O.[114] Quantitative tracking by LCF more clearly demonstrates that the early loss of Cu NPs is counterbalanced by a rapid growth of Cu_2O cubes (Fig. 3.9c). Beyond this critical period of Cu_2O formation ending around 600s, most of the steady state structure is characterized by the retention of cuboidal Cu_2O crystals. At more negative potentials, the phase evolution is accelerated but results in a similar final phase distribution (Fig. 3.12). The minor metallic Cu phase is mainly found at the junctions of aggregates of Cu_2O cubes (Fig. 3.13). Thus, *ex situ* XANES further confirms that the evolution of Cu NPs results in Cu_2O cuboidal rich structures as first identified using *ex situ* electron microscopy.

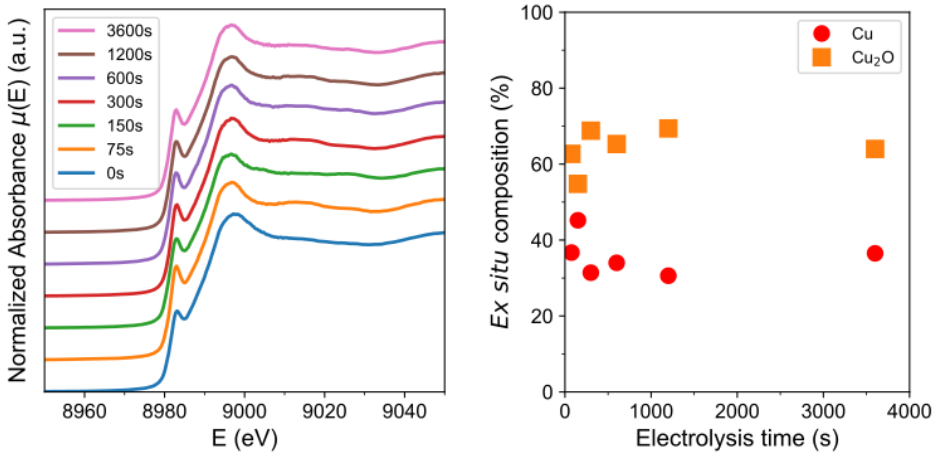

Figure 3.12. XANES time series of the Cu NP ensemble electrode biased at -0.8 V vs. RHE, showing compositional information corroborating the rapid evolution demonstrated by microscopy (Fig. 3.3). LCF analysis shows that the distribution of Cu and Cu_2O created at a very early time stage (75 s) already resembles the steady state, consistent with the structural characterization. In addition, the steady-state composition of approximately 60 – 70% Cu_2O is consistent with that observed for the electrode created at -0.6 V vs. RHE as presented in the main text.

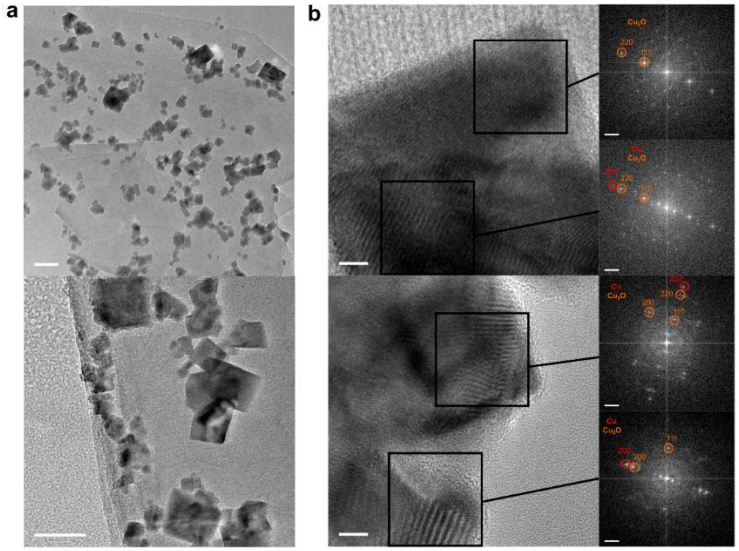

Figure 3.13. TEM and HRTEM characterization of the catalyst after one hour of electrolysis, the "steady-state" structure. (a) TEM (scale bars 50 nm) confirms the distribution of larger cubic crystals with small shapes, some of which are also cuboidal and some of which appear more irregular. In all cases, significant "junctions" exist between cuboidal features. (b) HRTEM (scale bars 5 nm) at the junctions of cuboids, with corresponding FFTs (scale bars 2 nm^{-1}) illustrates the location of the minor Cu phase. Such areas are rich with moiré patterns, where Cu reflections can frequently be found overlaid against the crystalline Cu_2O. In areas without the moiré, highly crystalline Cu_2O is more typical, as shown by the top example.

To evaluate the catalytic relevance of the appearance of Cu_2O cuboids, we considered two methods of varying the original evolved Cu NP system (Sample O). First, larger 14 nm Cu NPs (Sample L) were synthesized to controllably change the starting state of the material (Fig. 3.14). The characteristic cube formation is absent for these larger particles under similar electrochemical conditions (Fig. 3.15). Furthermore, the phase distribution remains mostly metallic throughout electrolysis (Fig. 3.16).

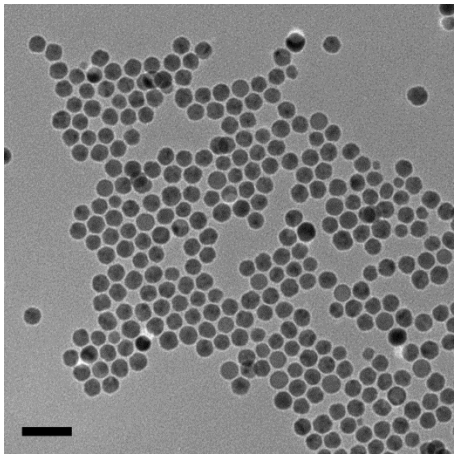

Figure 3.14. TEM of the 14 nm Cu NPs (Sample L) which are also of uniform size distribution and spherical in shape. Scale bar 50 nm.

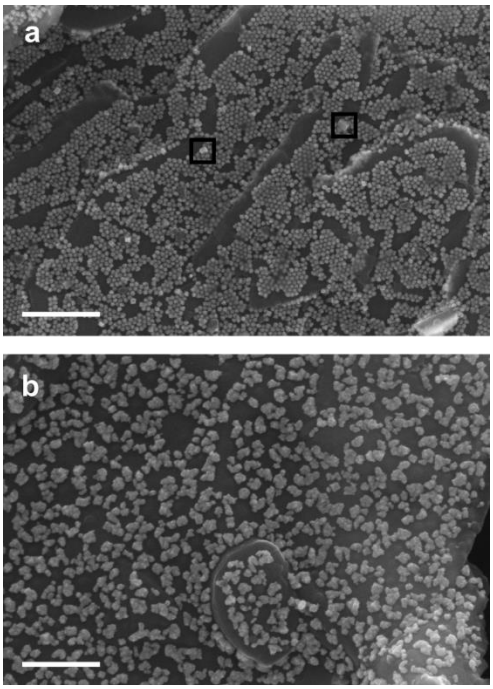

Figure 3.15. Sample L after (a) 150s and (b) 3600s of bias at -0.6 V vs. RHE. Contrasted with the 7 nm Cu NPs, the 14 nm NPs are much more resistant to change, with very few cuboidal structures forming in the early stage (marked in black squares) and the steady-state also lacking sharp cuboidal features, composed of mostly rough, irregular morphologies. Scale bars 200 nm.

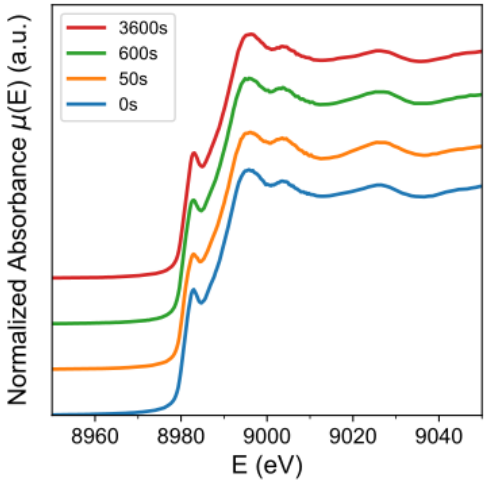

Figure 3.16. XANES of Sample L at different time points. The *ex situ* oxide growth observed in Sample O is absent in L throughout electrolysis.

Secondly, we also aimed to disrupt the evolution process of the original nanoparticles by applying a voltammetric pulse perturbation program. The perturbation is applied at frequent intervals throughout the critical period of evolution, interrupting the transformation with a mild oxidation pulse (Fig. 3.17). As a result, despite beginning with the same NPs, the pulsed electrode (Sample P) consists of larger, more irregular morphologies compared to Sample O (Fig. 3.18).

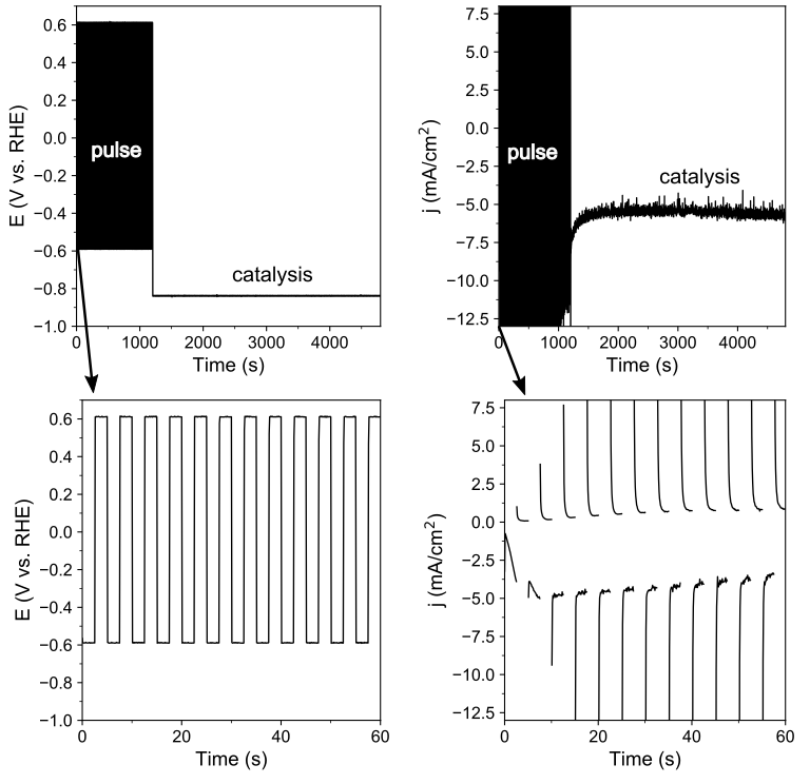

Figure 3.17. Pulse program (E vs. t, left) and current response (*j* vs. t, right) for Sample P, where the electrode is cycled between 2.5s at -0.6 V vs. RHE (growth) and 2.5s at +0.6 V vs. RHE (perturbation). The full period of bias is shown at top, where after 20 minutes of pulsing, catalytic activity is measured for the next 60 minutes. The first 60 seconds of pulsing is shown at bottom. Spikes are due to capacitive current from rapid potential switching. Notably, the electrochemical perturbation is a mild surface redox cycling as indicated by the low, positive current density during the perturbation pulse (~0.1 mA/cm^2 or lower), with the negative current density afterwards still matching closely with the established current density in the previous cycle.

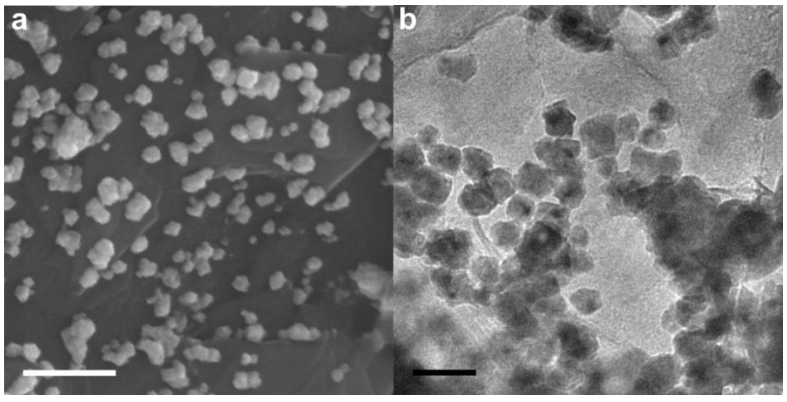

Figure 3.18. (a) SEM and (b) TEM of Sample P after 1 hr of CO_2 electrolysis. Compared to Sample O, P exhibits more of irregular morphologies, although the overall distribution of particles is similar to that of O. Scale bars (a) 200 nm and (b) 50 nm.

A substantial reduction of C_{2+} formation is observed for Samples L and P relative to O (Fig. 3.9d and Fig. 3.19), in conjunction with a more metallic composition by XANES (Fig. 3.9e) and more polycrystalline aggregates of Cu as opposed to cuboidal oxides (Fig. 3.20).

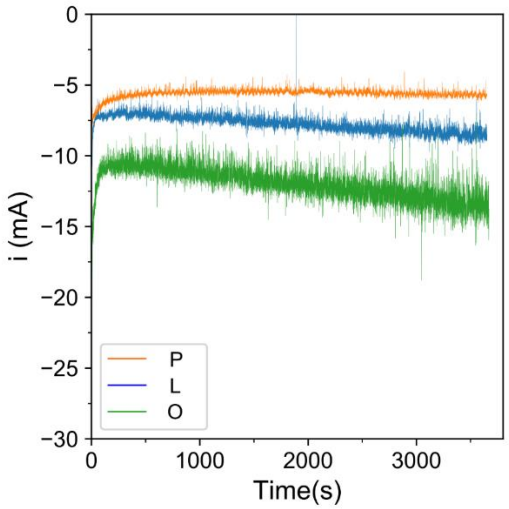

Figure 3.19. Representative electrolytic current traces over a full hour of electrolysis for the three catalysts compared in this study (O,L,P). Occasional spikes in current are due to measurement glitches in the potentiostat.

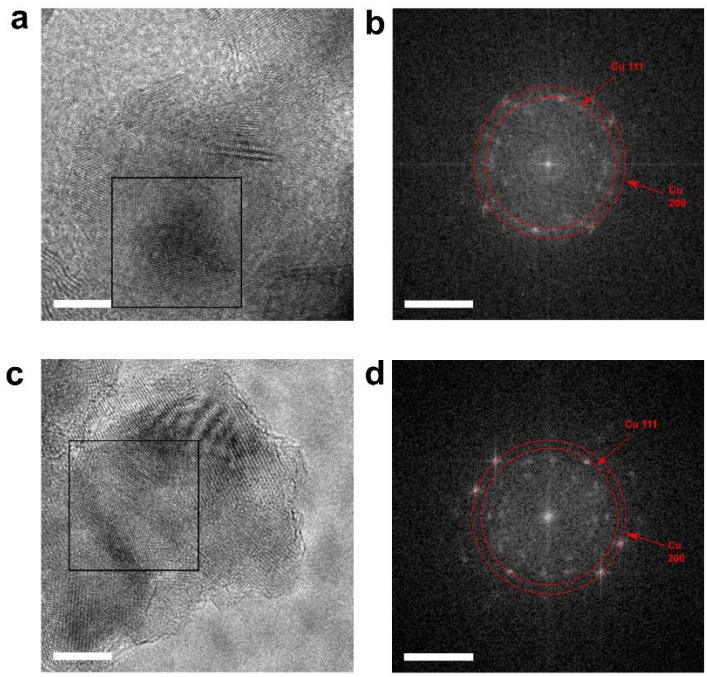

Figure 3.20. HRTEMs (scale bars 2 nm) and corresponding FFT of the representative structures in Sample P (a,b) and Sample L (c,d) post-electrocatalysis. Unlike Sample O (see Figure 3.13) which contains extended domains of single-crystal Cu_2O with minor metallic Cu located in areas of material overlap, Samples L and P mostly consist of structures that inherently comprise multiple metallic crystallites. This is evident by the lack of obvious Cu_2O cubic features by

HRTEM and polycrystalline character of the FFT (scale bars 5 nm^{-1}), where Cu reflections are more dominant. These results support the ensemble-scale characterization of L and P as metal-dominated as shown in Fig. 3.9e.

As such, we find a direct correlation between C_{2+} selectivity of the evolved catalysts and the extent of Cu_2O contribution in the *ex situ* catalyst composition (Fig. 3.9e inset, Table 3.1).

	F.E. (%) @ -0.8 V vs. RHE		
Product	**7 nm NPs (O)**	**14 nm NPs (L)**	**Pulsed 7 nm NPs (P)**
Hydrogen	36.3	54.1	52.0
Carbon monoxide	5.5	14.3	16.5
Methane	0.3	0.1	0.2
Ethylene	32.5	9.2	9.2
Ethane	0.8	0.2	0.3
Formate	5.1	12.7	14.6
Acetate	0.9	0.6	0.7
Ethanol	11.7	4.4	3.3
n-propanol	5.7	4.2	3.3
Acetaldehyde	0.2	0.1	-
Allyl alcohol	0.5	-	-
Glycolaldehyde	0.3	-	-
Acetone	0.1	0.1	-

Table 3.1. Full product distribution for Samples O, L, and P at -0.8 V vs. RHE. Faradaic efficiencies have been normalized to 100% total products. In all cases, the measured total F.E. before normalization was between 90 and 95%, suggesting some amount of lost product.

These *ex situ* single-crystalline cuboidal Cu_2O structures are therefore a signature for catalytically enhanced C_{2+} formation. Variations of the evolution pathway, either by modifying the initial state or by perturbing the evolution process, shift the distribution of catalyst structures towards polycrystalline nanoparticles with a high proportion of metallic Cu post-reaction, correlated with lower activity for C_{2+} formation (Fig. 3.9f).

However, formation of Cu_2O is thermodynamically disfavored under CO_2 reducing conditions,[61,115] suggesting that the Cu_2O cubes should not have formed *in situ*. Indeed, when Cu_2O nanocubes are directly grown on the carbon support, activity is strictly limited to hydrogen evolution and C_1 formation at potentials where Sample O makes majority multicarbons (Fig. 3.21).

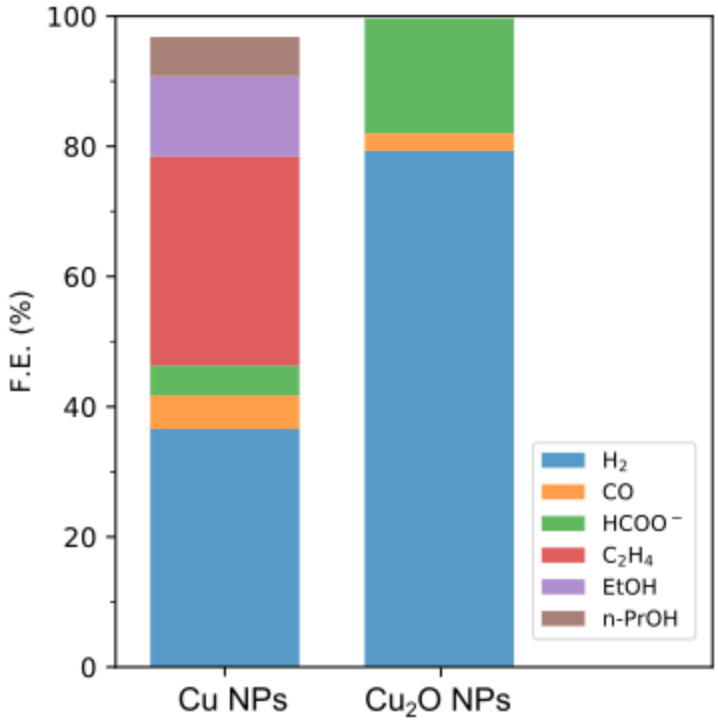

Figure 3.21. At -0.8 V vs. RHE, the electrochemically grown Cu_2O cube catalyst is completely inactive for C_{2+} formation compared with the evolved Cu NPs (i.e. Sample O), suggesting that the species active for C_{2+} formation is neither cubic Cu_2O nor its reduced analog.

Furthermore, Cu_2O electrochemically grown on carbon, after CO_2 electrolysis, is dominated by metallic Cu consisting of small particles and broken cubes with their facets destroyed (Fig. 3.22). Hence, neither crystalline Cu_2O itself nor its reduced equivalent is the active phase in the transformed Cu NP ensemble, despite the above *ex situ* observations.

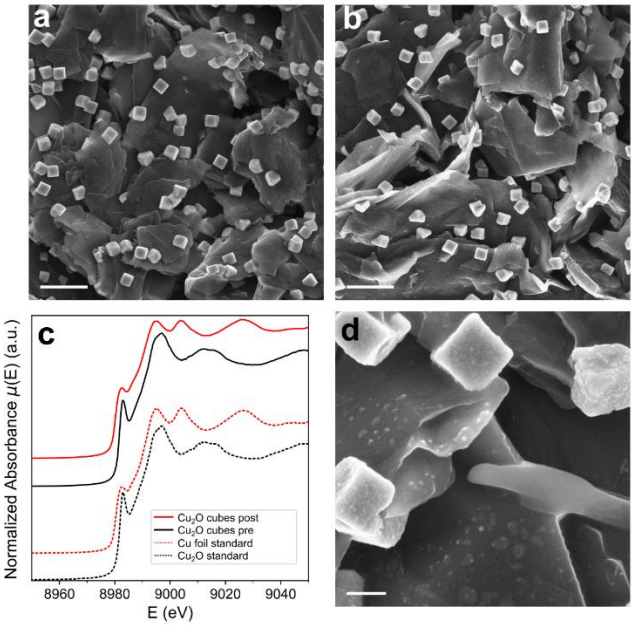

Figure 3.22. Electrochemically grown Cu_2O cubic particles (a) subject to the same electrolysis conditions at -0.8 V vs. RHE (b) yield a very different structural evolution (scale bars 1 μm). (c) XANES indicates that while the starting material is pure Cu_2O, electrolysis results in full reduction to metallic Cu with little to no oxide character after drying, in stark contrast with the other systems investigated. (d) The electrolysis creates a combination of roughened cubes with their facets destroyed and smaller particles; however, as consistent with the XANES, no cuboidal features indicating Cu_2O can be seen (scale bar 200 nm).

3.4.3 Preservation of the active structure reveals disrupted crystallinity

These findings suggest that a different structure, most likely metallic, is formed *in situ* and is uniquely active for CO_2-to-C_{2+}. Moreover, the structure readily and distinctively oxidizes to a single crystal Cu_2O cube at open circuit. To identify this structure, we employed a chemical immersion passivation method using benzotriazole (BTA), which is known to prevent copper oxidation (Fig. 3.23a).[116]

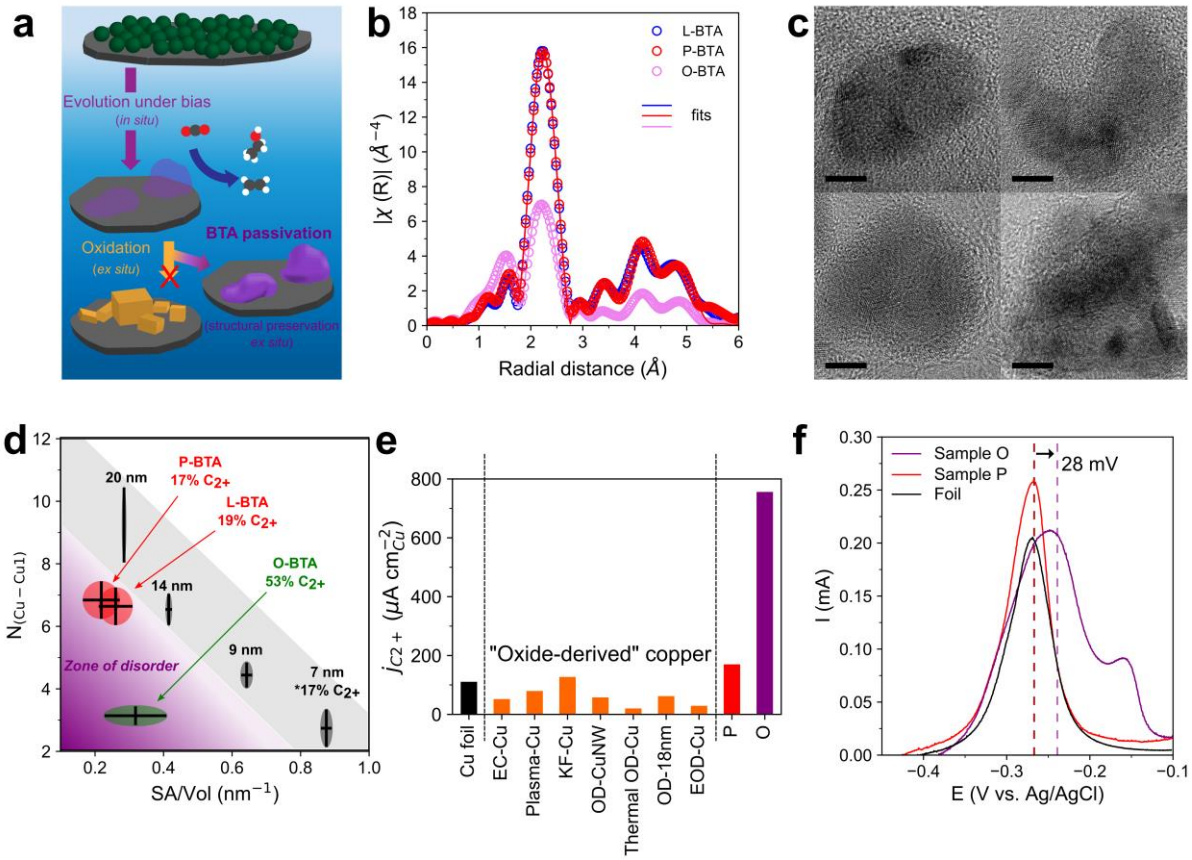

Figure 3.23. *Ex situ* elucidation of the disordered C-C active surface. (a) BTA passivation diverts oxidation of the active catalyst for characterization. (b) EXAFS of BTA-passivated O, L, and P with fits. (c) HRTEMs of O-BTA (scale bar 5 nm). (d) Relationship between SA/Vol and $N_{Cu\text{-}Cu1}$, showing unusually low coordination of O-BTA. Error bars are 1 SD. Isolated 7 nm NPs catalytic activity from previous work.[109] (e) Specific ECSA-normalized C_{2+} partial current density at -0.8 V vs. RHE for foil [65], high-performance oxide-derived catalysts from literature (see Fig. 3.34 for details), P, and O. (f) Desorption of underpotentially deposited Pb as an indicator for adsorbate binding strength, where Sample O exhibits anodic shifts (peaks at -0.25 and -0.16 V vs. Ag/AgCl) associated with its disordered surface. Dashed lines represent centroids for each anodic stripping voltammogram.

Immersion into a BTA solution immediately post-electrolysis coordinates BTA to the surface, impeding rapid oxidation and preserving the metallic portion of the electrode formed *in situ* as characterized by XANES, XRD, STEM-EELS, and XPS (Figs. 3.24 to 3.27). Notably, single-crystal Cu_2O is absent across the electrode, further suggesting that the Cu_2O cuboids observed *ex situ* were actually the oxidation product of the *in situ* formed Cu metal nanostructures.

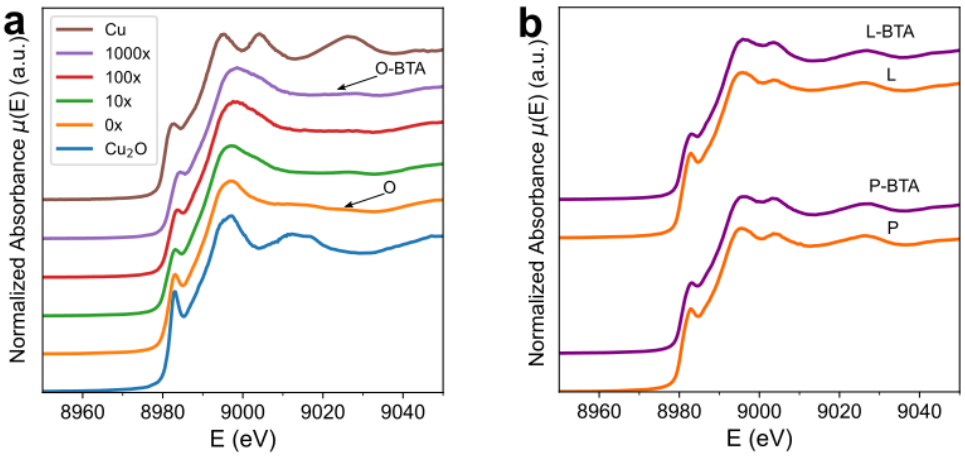

Figure 3.24. (a) To determine an appropriate amount of benzotriazole for oxidation prevention, a series of amounts (10 to 1000 mole ratios of BTA to Cu) were applied to a typical catalyst (Sample O), which was investigated for metal/oxide ratios by XANES. Between 100x and 1000x, a slight qualitative increase in passivation is still observed as indicated by increasing resemblance to the Cu standard; however, the effect is minor across orders of magnitude, and the prevention of complete oxidation seems limited due to the inherent tendency of Sample O to readily oxidize. However, the metallic portion of the sample is estimated to be above 80%. (b) For Samples L and P, BTA passivation shows the maintenance of metallic character better than in O-BTA, which is expected from the lack of significant *ex situ* oxidation in these samples in the first place.

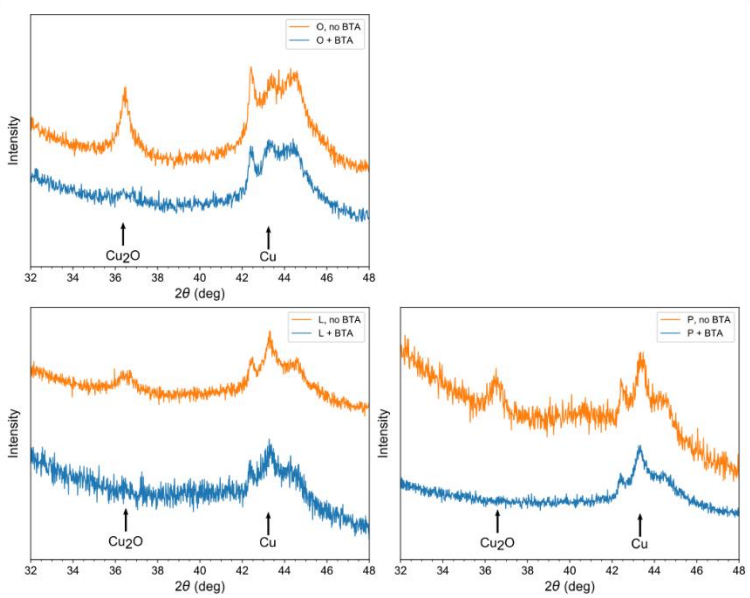

Figure 3.25. X-ray diffraction of O, L, and P treated with and without the BTA (1000x) shows a clear passivation through removal of the Cu_2O 111 lattice spacing, while preserving the Cu 111 feature. As in Fig. 3.24, limited prevention can still be observed in the case of O-BTA.

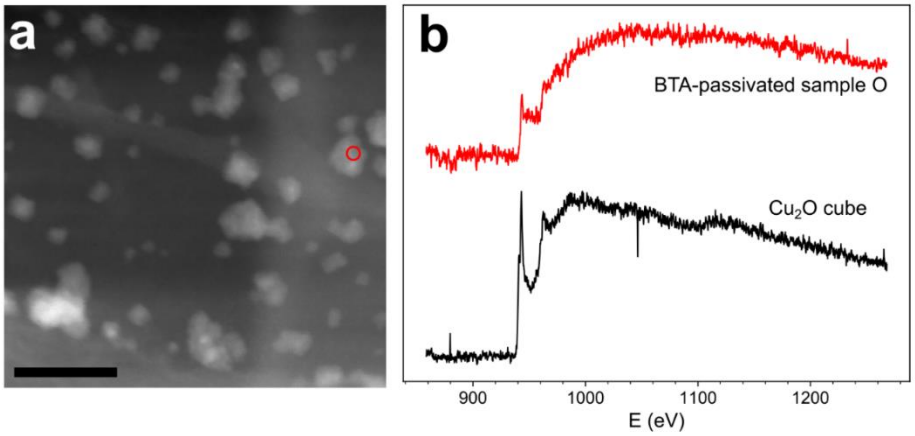

Figure 3.26. (a) High-angle annular dark field (HAADF, scale bar 50 nm) STEM micrograph of O-BTA with a representative structure selected for electron energy loss spectroscopy (EELS, b). The BTA-treated structures exhibit a metallic EELS by inspection of the Cu $L_{2,3}$ edge (above, red). [117] EELS of a typical Cu_2O cube formed in the absence of BTA is shown for comparison (below, black), which shows the typical white line feature for oxidized Cu.

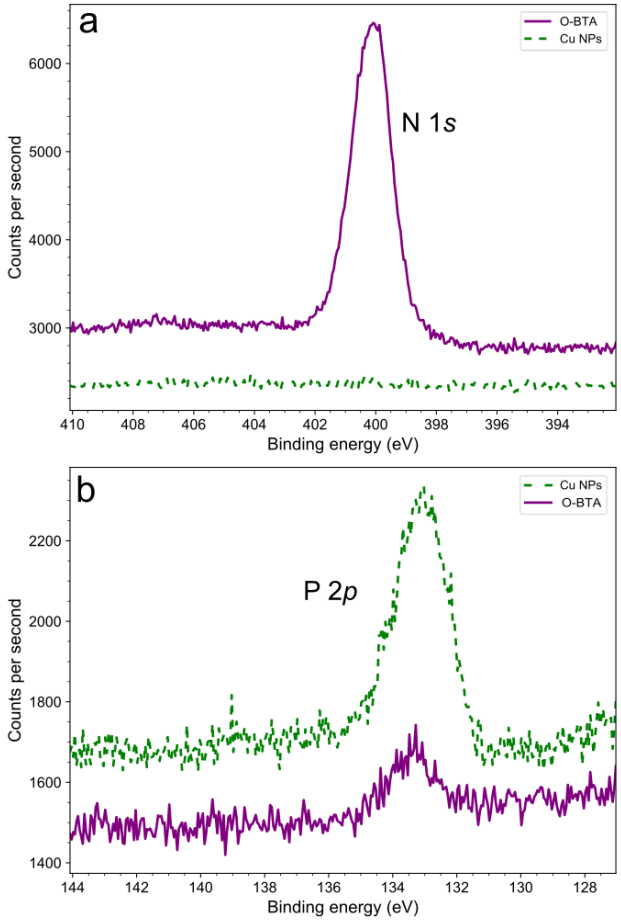

Figure 3.27. X-ray photoelectron spectra of the 7 nm NPs as-synthesized (dashed, green) and after electrolysis + BTA passivation (solid, purple). Spectra are shown here for comparison of absolute counts over identical probing area. The appearance of a pronounced peak in the N 1*s* region (a)

confirms the coordination of N-containing BTA to the surface of the catalyst after immersion. This coordination is suggested to impede rapid oxidation at the surface after a substantial amount of the native ligand, TDPA, is lost during electrolysis as shown by the drop in signal in the P 2*p* region (b).

EXAFS at the Cu K-edge was then used to probe the difference between the three catalysts when oxidation is inhibited by BTA (O-BTA, L-BTA, and P-BTA). A clear feature of O-BTA is the lower scattering amplitude from the first Cu shell of the metallic phase, with its subsequent shells following a similar trend (Fig. 3.23b). The EXAFS-derived fitting parameter $N_{Cu\text{-}Cu1}$ is used here as a quantitative descriptor of this empirical scattering amplitude difference. According to the fits (Table 3.2), O-BTA exhibits a considerably lower $N_{Cu\text{-}Cu1}$ (3.1) compared to the other catalysts L-BTA ($N_{Cu\text{-}Cu1}$ = 6.8) and P-BTA ($N_{Cu\text{-}Cu1}$ = 6.6).

	"O-BTA"			**"L-BTA"**			**"P-BTA"**		
	N	*R* (Å)	σ^2	*N*	*R* (Å)	σ^2	*N*	*R* (Å)	σ^2
Cu-O	1.7(0.2)	1.90(1)	0.006(2)	0.8(0.3)	1.85(2)	0.006(6)	1.0(0.4)	1.86(2)	0.008(6)
Cu-Cu1(met)	3.1(0.3)	2.54(1)	0.008(1)	6.8(0.6)	2.54(1)	0.008(1)	6.6(0.6)	2.54(1)	0.008(1)
Cu-Cu1(ox)	-	-	-	-	-	-	-	-	-
Cu-Cu2	6.0(0.0)	3.59(2)	0.025(3)	6.0(0.0)	3.58(2)	0.016(2)	6.0(0.0)	3.57(2)	0.017(3)
Cu-Cu3	17.6(8.2)	4.47(2)	0.024(6)	21.8(7.9)	4.46(1)	0.017(4)	21.3(7.4)	4.46(1)	0.016(4)
Cu-Cu1-Cu4	12.0(9.6)	5.18(2)	0.022(8)	12.7(7.2)	5.18(1)	0.014(5)	13.3(7.7)	5.18(1)	0.014(5)
ΔE_{Cu}		3.6(1.0)			4.6(0.8)			4.7(0.8)	
ΔE_{Cu2O}		7.2(1.3)			4.6(0.8)			4.7(0.8)	
R-factor		0.7%			0.1%			0.9%	

Table 3.2. EXAFS fitting parameters for the fits displayed in Fig. 3.23.

To contextualize this trend, a series of nanoparticles with varying size and well-defined crystallinity were employed as standards (Fig. 3.28). The EXAFS-derived $N_{Cu\text{-}Cu1}$ is expected to decrease for smaller sized nanoparticles (Fig. 3.29 and Table 3.3) by the rise in the surface area to volume ratio (SA/Vol); however, $N_{Cu\text{-}Cu1}$ for O-BTA is unexpectedly low given its size of structures (~20 nm).

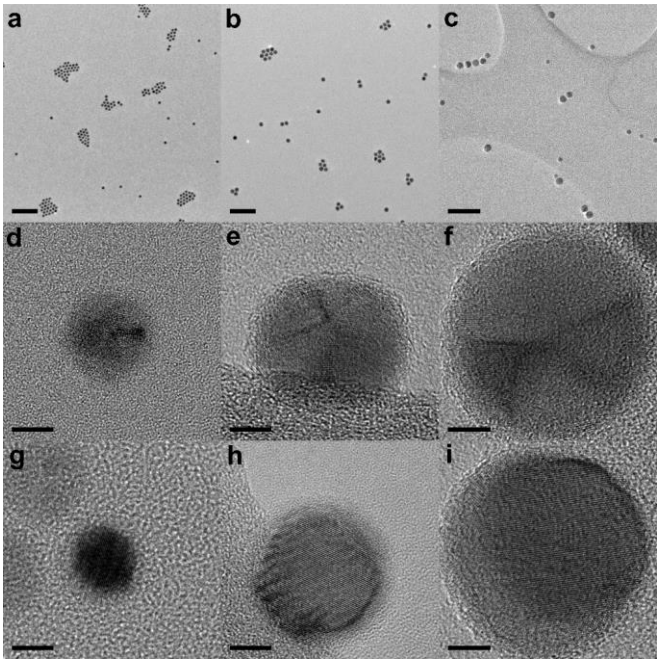

Fig. S25. TEM of (a) 9, (b) 14, and (c) 20 nm particles (scale bars 100 nm), as well as HRTEM (scale bars 5 nm) showing 5-fold twin (d-f) and single crystal (g-i) particles, representing their well-defined crystallinity.

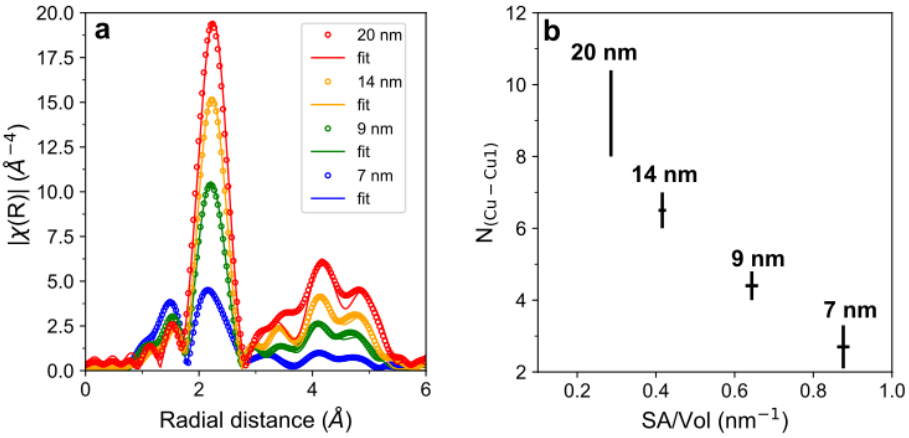

Fig. S26. (a) EXAFS with fits of 7, 9, 14, and 20 nm standard Cu NPs as shown in Figures S4 and S25. The amplitude of the Cu-Cu first shell decreases with decreasing size, which can be attributed to the increase in the proportion of undercoordinated surface atoms. This results in a decreasing observed coordination number with respect to SA/Vol, shown in (b). Error bars are 1 SD.

	"7 nm"			"9 nm"			"14 nm"		
	N	*R* (Å)	σ^2	*N*	*R* (Å)	σ^2	*N*	*R* (Å)	σ^2
Cu-O	1.3(0.1)	1.87(1)	0.003(1)	1.0(0.2)	1.89(2)	0.004(3)	0.6(0.2)	1.89(4)	0.003(5)
Cu-Cu1(met)	2.7(0.6)	2.54(1)	0.010(2)	4.6(0.4)	2.54(1)	0.008(1)	6.5(0.5)	2.54(1)	0.008(1)
Cu-Cu1(ox)	12.0(0.0)	2.92(4)	0.050(8)	-	-	-	-	-	-
Cu-Cu2	6.0(0.0)	3.61(3)	0.026(3)	6.0(0.0)	3.58(2)	0.020(3)	6.0(0.0)	3.58(2)	0.016(2)
Cu-Cu3	9.4(6.4)	4.47(3)	0.023(8)	16.8(7.4)	4.46(2)	0.019(5)	20.2(7.2)	4.46(1)	0.017(4)
Cu-Cu1-Cu4	5.6(8.1)	5.18(3)	0.022(14)	9.4(7.2)	5.18(2)	0.016(7)	11.2(6.7)	5.18(1)	0.014(5)
ΔE_{Cu}		3.6(1.2)			3.2(0.9)			4.7(0.8)	
ΔE_{Cu2O}		5.7(1.1)			8.4(2.4)			11.5(4.3)	
R-factor		0.7%			0.9%			0.8%	

	"20 nm"		
	N	*R* (Å)	σ^2
Cu-O	-	-	-
Cu-Cu1(met)	9.2(1.2)	2.55(1)	0.008(1)
Cu-Cu1(ox)	-	-	-
Cu-Cu2	4.4(3.3)	3.60(3)	0.011(7)
Cu-Cu3	18.2(5.6)	4.46(1)	0.012(3)
Cu-Cu1-Cu4	9.1(6.5)	5.19(2)	0.009(5)
ΔE_{Cu}		5.9(0.6)	
ΔE_{Cu2O}		-	
R-factor		3.2%	

Table 3.3. EXAFS fitting parameters for the fits displayed in Fig. 3.29.

Furthermore, all three BTA-passivated samples are composed of similarly sized nanostructures (Fig. 3.30) and therefore, the difference in SA/Vol does not sufficiently explain the difference in $N_{Cu\text{-}Cu1}$ between O-BTA and L/P-BTA.

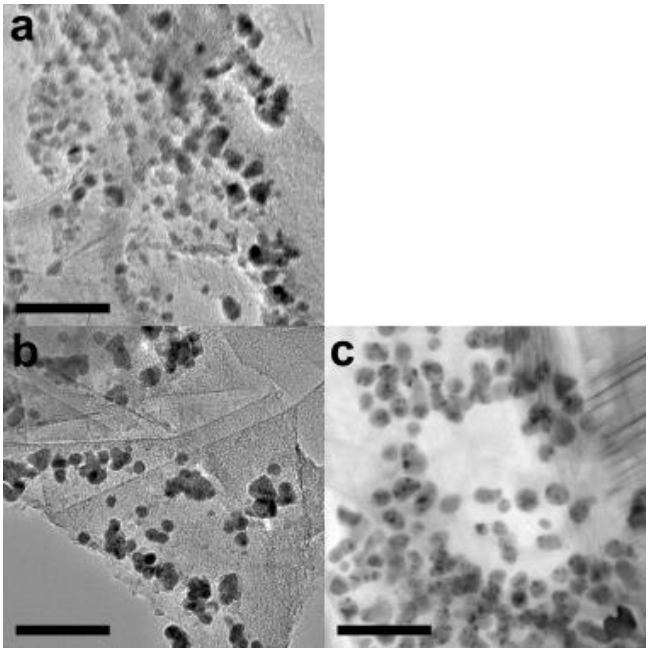

Figure 3.30. TEM of (a) O-BTA, (b) L-BTA, (c) P-BTA, showing that the passivated evolved structures are roughly similar in size, in the region of 20 nm. Scale bars 100 nm.

Low $N_{Cu\text{-}Cu1}$ can result not only from having a higher portion of atoms with missing neighbors, but also by local atomic disorder, which leads to destructive interference of the scattered X-rays.[118] Therefore, O-BTA should have considerably lower crystalline order compared against L/P-BTA to attain such a low $N_{Cu\text{-}Cu1}$ at a similar SA/Vol. Indeed, crystalline domains in O-BTA are difficult to detect by HRTEM (Fig. 3.23c), in contrast with L/P-BTA where extended metallic domains are easily identified (Fig. 3.31). Nanobeam electron diffraction (Fig. 3.32) confirms the relative lack of crystallinity in O-BTA as well.

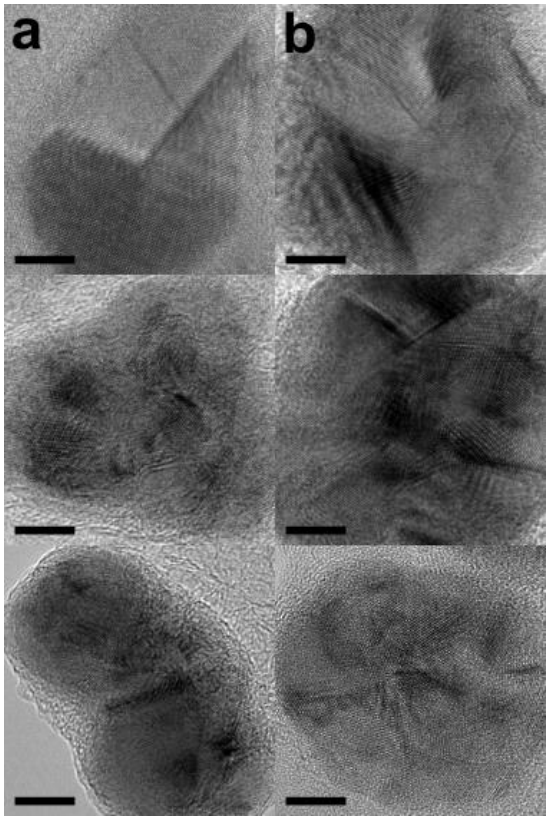

Figure 3.31. HRTEM of (a) L-BTA and (b) P-BTA showing facile identification of extended crystalline domains, in contrast with O-BTA shown in Fig. 3.23. Scale bars 5 nm.

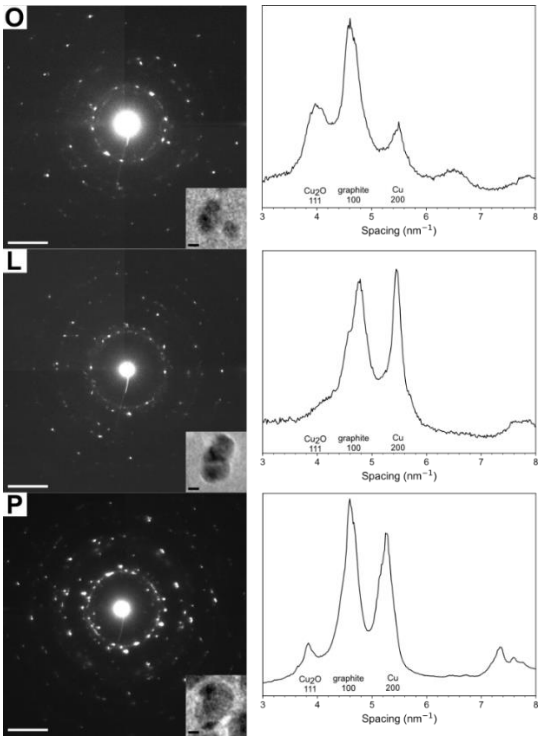

Figure 3.32. Nanobeam electron diffraction (NBED) patterns of O, L, and P passivated by BTA (scale bars 5 nm^{-1}) with TEM inset showing the structures selected in each case (scale bars 10 nm). The DPs are a mix of copper nanostructures and the background graphite from carbon paper. Radial integration of these DPs (right) facilitates the comparison of crystallinity across samples. The Cu 200 reflection is significantly more intense in L-BTA and P-BTA than O-BTA. The Cu 111 reflection overlaps with graphite 100 from the substrate.

These observations indicate that O-BTA achieves a unique state of structural disorder characterized by a low EXAFS-derived $N_{Cu\text{-}Cu1}$ at low SA/Vol (Fig. 3.23). Further details of the calculation employed (and, consequently, how error bars and SDs were generated) are as follows.

3.4.4 Calculation of the expected relationship between EXAFS-derived N and SA/Vol

$N_{Cu\text{-}Cu1}$ is naturally expected to decrease as the diameter of crystalline nanoparticles decreases, or equivalently, as the SA/Vol rises. Here I briefly discuss the method we employ to semi-quantitatively contextualize this relationship against the anomalous $N_{Cu\text{-}Cu1}$ and SA/Vol of O-BTA. The nanoparticles synthesized in this work are a mixture of five-fold twinned nanoparticles and single crystals, as observed by HRTEM. The diameters (d) are measured by TEM to be 6.78 ± 0.49, 9.18 ± 0.85, 14.19 ± 1.35, and 19.86 ± 3.47 nm respectively. As a first order approximation, we consider these nanoparticles to be spherical. We approximate O/L/P-BTA as spherical too, although we recognize that because the structures have lower circularity by TEM, this approximation will increase the uncertainty in our measurements.

For spherical particles, the SA/Vol scales as $3/r$. However, determining the average SA/Vol of the system by summing SA/Vol of individual particles as:

$$SA/Vol = \frac{1}{N}\sum_{i=1}^{N}\left(\frac{3}{r_i}\right)$$

puts equal weight on each particle, which is an invalid assumption. Larger particles contain more atoms, and hence will contribute more to the EXAFS signal. The average SA/Vol should therefore be weighted by number of atoms rather than by particle.

To achieve this, we consider random samples of particles captured by TEM frames as being representative of an EXAFS spot. We then sum the overall surface area and divide by the overall volume within the sample to represent the SA/Vol captured by the EXAFS spot, as follows:

$$SA/Vol = \frac{\sum SA_i}{\sum Vol_i}$$

where SA and Vol are determined by the projected surface area and volume of each particle. This will naturally decrease the SA/Vol relative to weighting by particle, owing to the increased contribution of larger structures, which again, is representative of the EXAFS signal. Notably, this does not affect the average SA/Vol of the spherical nanoparticles much due to the low variance in particle diameter and high circularity. For instance, for the 7 nm NP, weighting by atom as shown here yields a SA/Vol of 0.876, whereas weighting by particle yields 0.882. However, the difference is magnified for O/L/P-BTA, where the increased variance in diameter increases the impact of larger particles that is unaccounted for when particles are equally weighted.

At least 3 random samples (*i.e.* TEM frames) are taken, with the particle sizes measured, from which means and standard deviations are drawn, which are shown in Fig 3.23.

3.4.5 Catalytic implications of the disordered surface

To summarize the salient results from the previous section, L/P-BTA exhibit similarly low SA/Vol to O-BTA but higher $N_{Cu\text{-}Cu1}$, indicating that higher crystalline order is linked to their lower C_{2+} selectivity. Furthermore, low $N_{Cu\text{-}Cu1}$ achieved by high SA/Vol in a crystalline state is likewise insufficient to attain high C_{2+} selectivity at low overpotentials, as evidenced by the activity of isolated small Cu nanoparticles (Fig. 3.23d).[109] These findings strongly suggest that the active surface electrochemically formed and catalytically favorable for CO_2-to-multicarbons exists in a regime of disorder (both low $N_{Cu\text{-}Cu1}$ and low SA/Vol). Previous works have conjectured C_{2+}-boosting effects of tuning binding strength of key intermediates, especially *CO, on diverse and undercoordinated copper surfaces.[60,62,66] Accordingly, a host of high-activity oxide-derived copper catalysts may present such disordered surface sites. However, the direct identification/quantitation of disorder in these catalysts and its effect on binding has not emerged, likely because the large volume involved of the necessary copper oxides as precursors (*e.g.* oxidized Cu foils) yields large proportion of bulk atoms that are catalytically irrelevant but spectroscopically obtrusive for ensemble characterization. Furthermore, because such OD-Cu catalysts tend to have high roughness factors, they may present a complex mix of disordered/undercoordinated active sites and catalytically inactive copper surfaces, one possible explanation for the lack of intrinsic activity increase previously observed.[21]

To interrogate whether a disordered Cu surface as in Sample O truly enhances intrinsic C-C activity, we estimated the electrochemical surface area (ECSA)-normalized specific C_{2+} activity ($\mu A/cm^2_{Cu}$) of the catalysts using lead underpotential deposition (UPD) to measure Cu ECSA (Fig. 3.33).

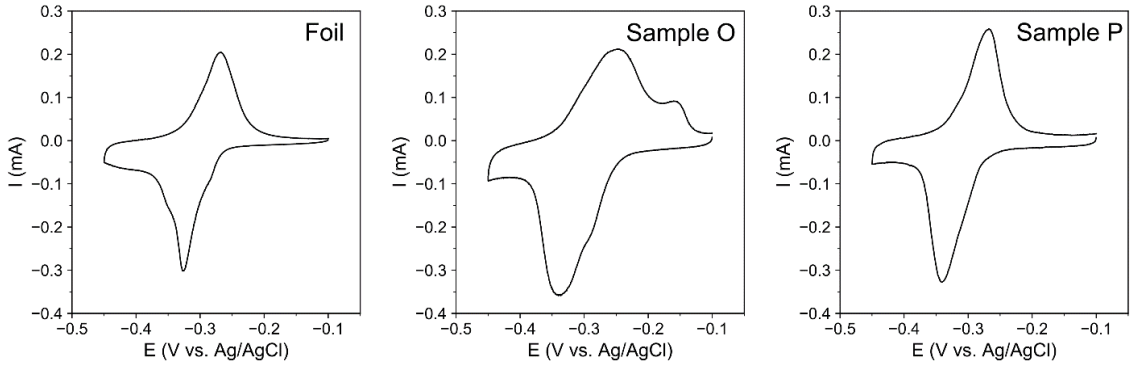

Figure. 3.33. Full cyclic voltammetry in the Pb underpotential deposition potential window for Cu foil, Sample O, and Sample P. The geometric area of Cu foil used is 4.5 cm^2 (with ECSA of 4.5 cm^2) to roughly match the ECSA of Samples O (8.8 cm^2) and P (5.4 cm^2).

The justification of using Pb UPD is as follows. The vast majority of works in the CO_2 literature measure ECSA for Cu using double layer capacitance (DLC).[21] We consider DLC insufficient for the measurement of this catalyst, as the catalyst consists of two elements, carbon and Cu, for which only the Cu surface area is relevant when evaluating intrinsic activity. Thus, the

evaluation of ECSA should involve a chemically specific technique, which we find lead underpotential deposition to be more apt. We find the UPD behavior of Pb on Cu foil to be in line with previous reports, with the estimated charge per cm^2 of polycrystalline Cu to be 270 $\mu C/cm^2$, which is consistent with previous reports.[119]

A rough estimation of ECSA can be provided by the SA/Vol calculations from the prior section, as a check for whether the UPD-derived ECSA is reasonable. Considering the average SA/Vol of the passivated Sample O to be 0.32 nm^{-1}, and given the mass loading of Cu to be 68.9 μg, with half of the area not electrochemically accessible due to being attached to the carbon substrate, we arrive at an estimated 12 cm^2 $ECSA_{Cu}$. We find this estimate to corroborate well with the Pb UPD result (8.8 cm^2), given that the SA/Vol calculation does not consider the SA lost to the junctions within regions of inter-connected particles in denser areas of the electrode. Thus, the ECSA estimated by this simple consideration of SA/Vol should be an overestimate.

In addition, we note that in the case of Sample O, the UPD features change significantly if the electrode is allowed to oxidize to transform into Cu_2O cubes, as shown later in Fig. 3.36a. This also results in a decrease in $ECSA_{Cu}$ from 8.8 cm^2 to 6.8 cm^2, which is reasonable considering the replacement of disordered Cu with reduced crystalline Cu_2O cubes. Thus, considering the change after oxidation, the UPD value measured as 8.8 cm^2 should be more representative of the metallic catalyst before it is allowed to fully oxidize, given that the time between electrolysis and Pb UPD measurement is approximately the same as that between electrolysis and BTA passivation.

Now, considering the specific ECSA of Cu as measured by Pb UPD, Sample O exhibits a considerable 7-fold increase in C_{2+} activity to that of a Cu foil, whereas the polycrystalline Sample P exhibits only a minor increase (Fig. 3.23e). OD-Cu catalysts[56,65,66,107] that show high performance by typically presented metrics such as F.E. (Fig. 3.34) demonstrate similar or lower intrinsic activity to Sample P or Cu foil as well.[21]

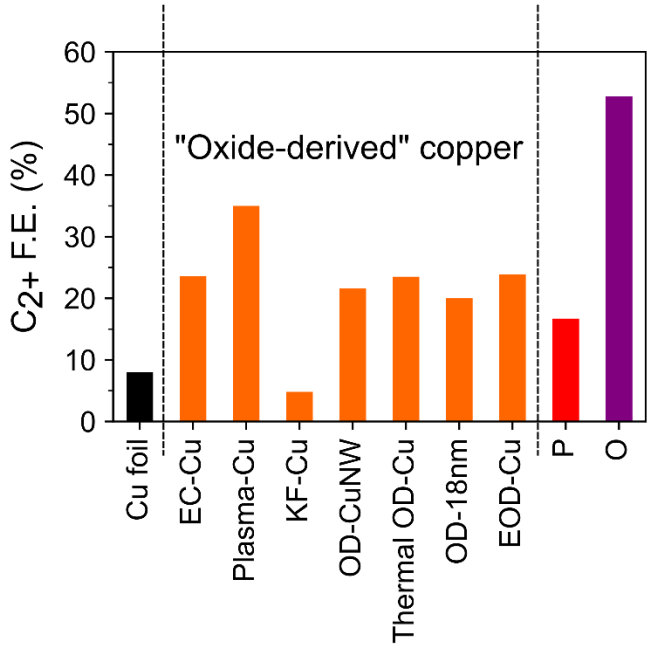

Figure 3.34. Comparison with literature reports of high-performance oxide-derived Cu catalysts for which the ECSA is reported, at -0.8 V vs. RHE in 0.1 M $KHCO_3$. Many OD-Cu catalysts

significantly outperform Cu foil by C_{2+} F.E., resulting in their consideration as state-of-the-art catalysts. However, the high RF of these catalysts results in low intrinsic activity in stark contrast to Sample O with a high density of disordered active surfaces, as explicated in the main text. Catalyst references: EC-Cu (electrochemically cycled cubic oxides in KCl-containing electrolyte),[65] Plasma-Cu (Cu foil treated with O_2 plasma),[56] KF-Cu (electrochemically cycled in KF-containing electrolyte),[107] OD-CuNW (reduced alkaline-derived $CuO/Cu(OH)_2$ nanowires),[65] Thermal OD-Cu (Cu foil annealed at high temperatures with oxygen),[65] OD-18nm (thin film of reduced Cu_2O with average crystallite size 18nm),[66] EOD-Cu (electrochemically deposited Cu_2O).[65]

In contrast, the enrichment of active disordered sites on Sample O is directly responsible for a higher C-C dimerization activity per copper surface available, ranging from 6- to 40-fold enhancement over a representative spread of OD-Cu catalysts (Fig. 3.23e and Fig. 3.35) at moderate overpotential (-0.8 V vs. RHE).

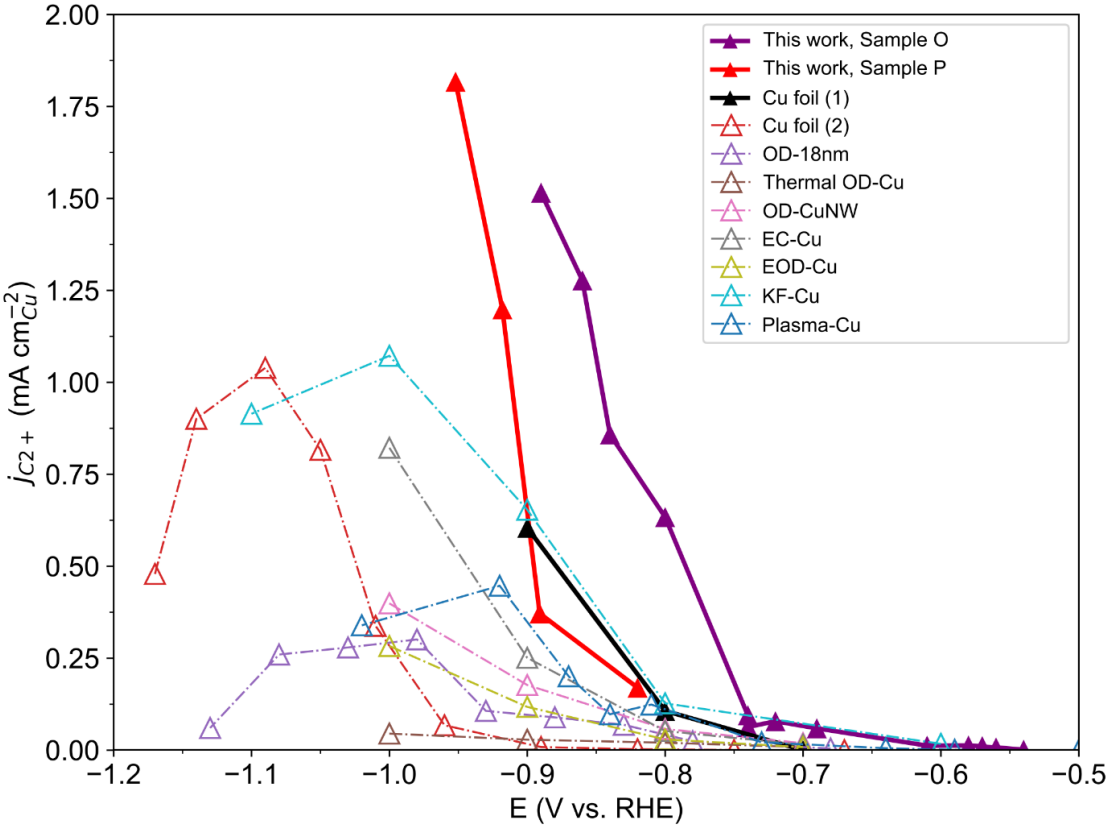

Figure 3.35. Full comparison across a range of potentials for the ECSA-normalized C_{2+} production rate as shown in Figs. 3.23 and 3.34. A second reference for Cu foil[25] is added here, showing the variability across Cu foil comparisons in the literature, likely owing to differences in electrochemical setup. Hence, we elected to use the higher reported values for intrinsic activity for Cu foil, such that our observed enhancement is a conservative estimate. The remainder of comparison catalysts are as explained in the caption for Fig. 3.34.

The high degree of disorder exhibited by Sample O is expected to result in a large concentration of strong binding sites for the key intermediate *CO, thereby increasing the probability and rate of C-C dimerization. Desorption of underpotentially deposited Pb sheds some light into this aspect (Fig. 3.23f). Sample O exhibits Pb desorption peaks (-0.25 and -0.16 V vs. Ag/AgCl) that are quite anodically shifted compared to Sample P or Cu foil (-0.27 V vs. Ag/AgCl), resulting in a +28 mV shift in the centroid of the anodic stripping wave. This indicates that Sample O contains a prevalence of Cu surfaces that should have stronger electrochemical binding to adsorbates, with a lower presence of the sites on the crystalline counterpart (*i.e.* Cu foil) that exhibit weaker binding. The anodic shift is drastically diminished when the catalyst oxidizes to the characteristic single-crystal Cu_2O cubes, where the reduced equivalent is not disordered as before (Fig. 3.36). It is also observed in a greatly reduced manner on a representative OD-Cu catalyst (Fig. 3.36), which explains the low intrinsic C_{2+} activity resulting from their large portion of inactive Cu surfaces. Hence, enhanced C-C activity in Sample O stems from the concentration of disordered surfaces, which have an increased electrochemical binding strength to catalytic intermediates.

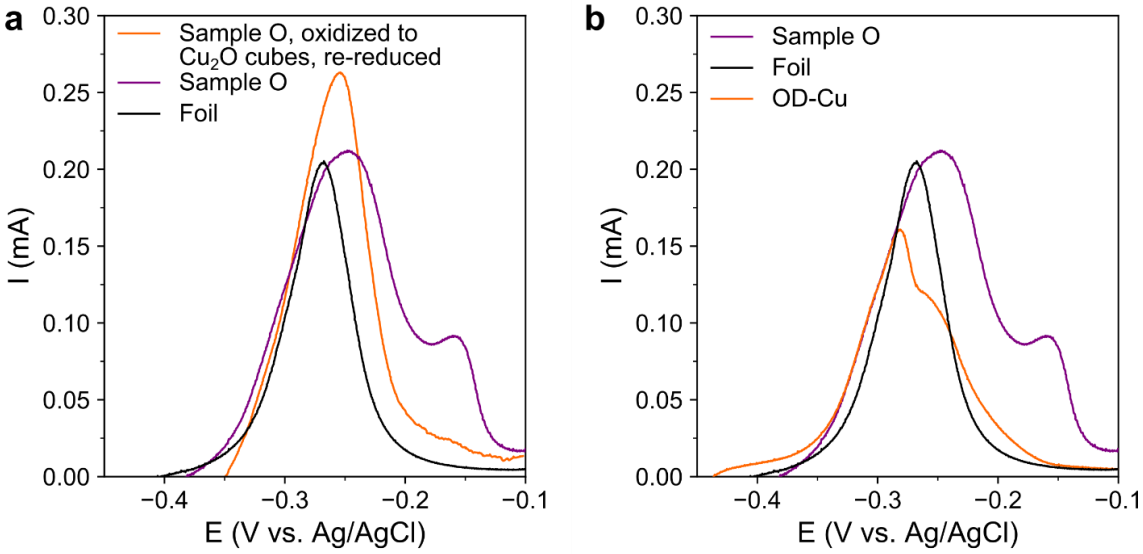

Figure 3.36. Anodic stripping of underpotentially deposited Pb on (a) Sample O after its oxidation to the characteristic Cu_2O cubes (and re-reduced) and (b) a representative OD-Cu catalyst (EC-Cu[65]). The strong anodic centroid shift (as especially evident by the anodic feature at -0.16 V) observed on Sample O is slight on OD-Cu, and is also dramatically reduced in the reduced equivalent of the Cu_2O cubes.

3.5 Conclusions and Perspective

Thus far, I have shown that understanding the structural evolution of a nanostructured system, even one with a clear structural signature, is not straightforward. The dramatic appearance of sharp cubic structures over time was eventually proven to be an artifact of post-reaction oxidation. Despite this, the resulting oxide is far from expected, as instead of the typical core-shell surface oxide formation, we observe single crystal Cu_2O cubes that span close to 100 nm in some cases. The nature of what active structure could form such a cube when simply exposed to ambient

conditions propelled us to use passivating techniques to preserve the *in situ* structure, upon which we acquired indications that the *in situ* structure could be characterized by its disorder as measured by EXAFS. Such a structure would also have catalytic implications, resulting in its high intrinsic activity towards CO_2-to-C_{2+}, and explains how such an active structure could only be formed from the *in situ* electrochemical evolution of the precursor particles.

Obviously, there are many unanswered questions remaining in the study of this fundamentally intriguing catalytic system. What is the origin of this evolution? Why do they oxidize into single crystals, and why cubes? How can such a structure be stabilized outside of the reaction conditions probed here? These questions point to deep materials dynamics that occur only at the interface of nanoscale materials and electrochemical conditions, and may involve factors yet to be imagined. However, before seeking to understand these matters (and thus bring ourselves closer to the ideal of using such evolution as a new means of catalyst synthesis), I will next discuss how *in situ* characterization techniques can help confirm some of the observations shown indirectly here.

Chapter 4. *In Situ* Characterization of Electrocatalyst Evolution and the Illumination of Electrochemical Scrambling

As with Chapter 3, portions of this chapter is adapted from "Electrochemically Scrambled Nanocrystals are Catalytically Active for CO_2-to-Multicarbons," Li, Y.*, Kim, D.*, Louisia, S., Xie, C., Kong, Q., Yu, S., Lin, T., Aloni, S., and Yang, P. *Proc. Natl. Acad. Sci. USA*, **2019**, In review.

Other portions of this chapter are part of an additional manuscript in preparation.

4.1 Preface

Following the previous chapter's discussion around how *ex situ* characterization assists the identification of the scrambling process and active site, I now discuss *in situ* methods development and future perspectives on shedding further insight on electrochemical evolution processes. In particular, I will focus on the relatively novel technique of electrochemical liquid cell transmission electron microscopy, which I will evaluate for its potential utility as applied to CO2RR at its present technological maturity, as others have done in reviews on the topic.[120,121] I follow this discussion with musings on the nature of this structural evolution and how it may be controlled and ultimately harnessed (as a generalizable phenomenon across materials) for the better of catalyst development.

4.2 Introduction

Within the sphere of research surrounding Cu electrocatalysts, a relatively underexplored topic is the origin and role of structural dynamics. In gas phase heterogeneous catalysts, the role of operation-induced restructuring in dictating catalytic activity is well-known.[71,101] Although many works aim to prevent these changes to improve catalyst stability,[76,102,112] recent reports have also suggested the necessity for restructuring to drive catalytic activity of new sites formed in situ.[71,109] In electrochemical systems, *in situ* studies of structural dynamics are more commonly reported in battery[122,123] and fuel cell catalyst[124] studies under redox cycling, where redox events presumably play a large role in facilitating atomic mobility. However, CO_2 electrocatalysts such as Au[75] and Cu[36,109] nanoparticles have been shown to restructure even under the purely cathodic bias conditions where redox is thermodynamically forbidden. These cathodic structural dynamics on Cu surfaces have been shown to benefit C_{2+} selectivity. For example, under operating conditions, bulk Cu foil is observed to restructure to the more C_{2+} selective (100) surface,[74] while structural evolution in Cu nanowires is directly linked to an increase in C_{2+} selectivity as discussed in Chapter 2. Considering the results discussed in the previous chapter, *in situ* observation of such evolution would be a necessary addition to the burgeoning volume of works on Cu structural evolution during CO_2RR.

The use of *in situ* techniques has recently been discussed and reviewed.[121] X-ray absorption spectroscopy, particularly near-edge structure (XANES), has been applied several times to understand the *in situ* oxidation state of Cu-based catalysts, given that they tend to be somewhat

oxide-derived.[59,73,125] Conclusions have been mixed, with some showing near-complete conversion to metallic Cu^0 and some showing the retention of Cu(I) species which are argued to be catalytically important towards the formation of desirable multicarbon products. As summarized in Chapter 1, this debate remains heated. In this work, however, the steady-state composition of the catalyst will be of lesser interest compared with the early-stage change of composition. Meanwhile, *in situ* liquid cell electron microscopy techniques have offered many interesting observations in the fields of crystal growth and nucleation,[126] fuel cell catalysts,[124] and especially in battery materials.[122,127] However, their application towards CO2RR electrocatalysts has only been proposed and yet to be demonstrated.

Here we present the use of complementary *in situ* characterization to assess the structural and compositional dynamics of the Cu NP ensemble catalyst under CO_2 electroreducing conditions. *In situ* X-ray absorption spectroscopy corroborates the hypothesis in the previous chapter that the true structures formed under operation are not Cu_2O themselves but rather Cu^0 species with a high tendency to form single crystal Cu_2O. Furthermore, the system is shown to undergo rapid kinetics. Hence, *in situ* transmission electron microscopy is used to trace the evolution under bias. This study demonstrates the first application of *in situ* electrochemical liquid cell TEM to illuminate the cathodic structural dynamics of CO2 electrocatalysts and highlights the importance of *in situ* characterization for a more complete understanding of a working catalyst.

4.3 Materials and Methods

4.3.1 Liquid cell *in situ* X-ray absorption spectroscopy

In situ X-ray absorption spectroscopy was conducted in a custom-designed PEEK electrochemical XAS cell. A working electrode was fabricated by depositing Cu NPs over a $1cm^2$ area of carbon paper (Sigracet 29AA), which was pressed against a 300 μm Kapton window. The cell was filled and constantly purged at under 1 sccm with 0.1 M $KHCO_3$ kept under CO_2 saturation. Open circuit voltage was measured during purging, and XANES were taken after the cell was completely filled. To begin electrochemical evolution, -1.3 V vs. Ag/AgCl was applied vs. the 3 M KCl Ag/AgCl reference electrode with a glassy carbon counter electrode. Due to the rapid structure evolution under bias, the XANES spectral range was truncated to shorten the measurement time of each spectrum to only 40 seconds, increasing temporal resolution for qualitative study. These spectra were processed without subtracting the pre-edge and post-edge backgrounds due to their truncated spectral range. Depending on the desired duration of bias, 1-20 lines were measured before electrolysis was stopped and the cell disassembled under ambient conditions.

4.3.2 Liquid cell electron microscopy

All *in situ* electron microscopy was conducted at 200 kV (JEOL 2100-F). Commercial electrochemical TEM chips (Hummingbird, XL P7 carbon electrochemical chip) were used with a 500 nm silicon nitride spacer (Hummingbird), such that the total assembly included 100 nm of silicon nitride and 500 nm of liquid volume. All biasing leads were carbon-coated Pt as supplied by the manufacturer. Further details are shown in Fig. 4.4.

To create working electrodes, a 2 μL droplet of a dilute (25 μg/mL) solution of Cu NPs in hexanes was spread over the viewing area of the chip. The droplet was allowed to evaporate, after which the full cell was assembled. 300 μL of ethanol were first purged through, after which 1-1.5

mL of 0.1 M $KHCO_3$ or pure H_2O were purged at 10 μL/min in order to wet and fill up the entire cell.

Electrochemical testing was conducted in a specially-designed biasing holder (Hummingbird) with a floating potentiostat (Gamry Interface 1000), using a three-electrode configuration. The biasing potential was methodically selected to be -0.6 V vs. the carbon pseudo-reference electrode, at which chronoamperometry using a typical cell produced ~500 nA of current. The carbon pseudo-reference electrode was tested to be near the reversible hydrogen electrode potential, such that the -0.6 V applied fell within the range of potentials investigated elsewhere in this study. This assumption was corroborated by water splitting experiments conducted in pure H_2O. In addition, higher currents/potentials (*e.g.* >1 μA at -0.8 V) were deemed unsuitable due to violent ruptures of the electrochemical cell, while significantly lower currents (*i.e.* order of 10-100 nA) failed to reproduce the cubic oxide structures post-electrolysis in favor of adventitious side reactions such as the growth of polycrystalline copper.

During bias, electrolyte purging was halted. Real-time videos were recorded using a screen capture program at 5 frames per second, matching both the raster rate of the STEM beam over the viewing frame and the exposure time of the camera during BF-TEM. After electrochemical imaging experiments, the holder was disconnected from the potentiostat. The cell was then directly disassembled and the working chip rinsed gently with H_2O before drying under N_2. The chip was then imaged by TEM and NBED (JEOL 2100-F) under vacuum conditions.

4.4 Results and Discussion

4.4.1 *In situ* X-ray absorption near-edge spectroscopy

The formation of a highly disordered structure as discussed in Chapter 3 strongly implies a necessity for rapid kinetics, as the thermodynamically preferred path is increasing crystallinity through coarsening. To study the kinetic aspects of electrochemical evolution, we used *in situ* liquid cell electrochemical (EC) XANES and (S)TEM to directly visualize their formation from the starting NP ensemble (Fig. 4.1). Importantly, the electrochemical conditions of evolution were matched as faithfully as possible to the original conditions; *i.e.* CO_2-saturated 0.1 M $KHCO_3$ was used as the buffer, and the evolution potential was set to -0.6 V vs. RHE. This potential was set against a pseudo-reference electrode in the TEM cell, which was previously calibrated to the same Ag/AgCl reference electrode used earlier. Serendipitously, the carbon pseudo-reference electrode was found to be quite similar to the reversible hydrogen electrode in its potential positioning, likely due to the nanoscale dimensions of the electrode resulting in minimal overpotential for HER.

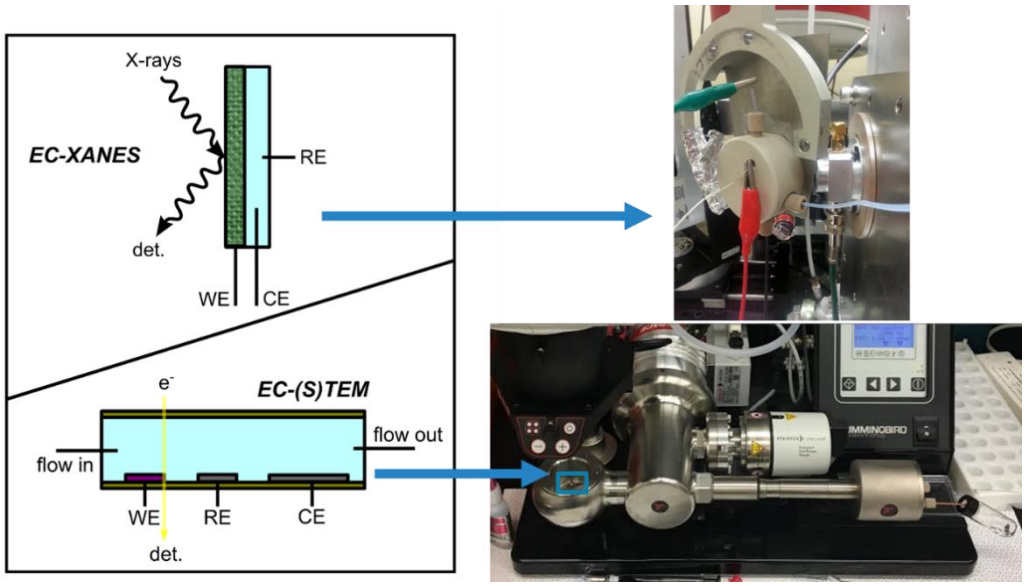

Figure 4.1. *In situ* characterization techniques for the Cu NP ensemble evolution under bias. Configurations used for *in situ* EC-XANES and EC-(S)TEM, accompanied by photographs of the cells.

Upon reductive bias, the EC-XANES shows a rapid (<40s) transition to metallic Cu (Fig. 4.2). This confirms that the phase of the *in situ* active structure is Cu^0, formed almost immediately upon bias. Because of the limited spectral window and low signal/noise ratio, the linear combination fitting previously employed in Chapter 3 is not possible here with high reliability; however, the Cu^0 phase can be readily identified by its spectral signature (two humps) in the near-edge region.

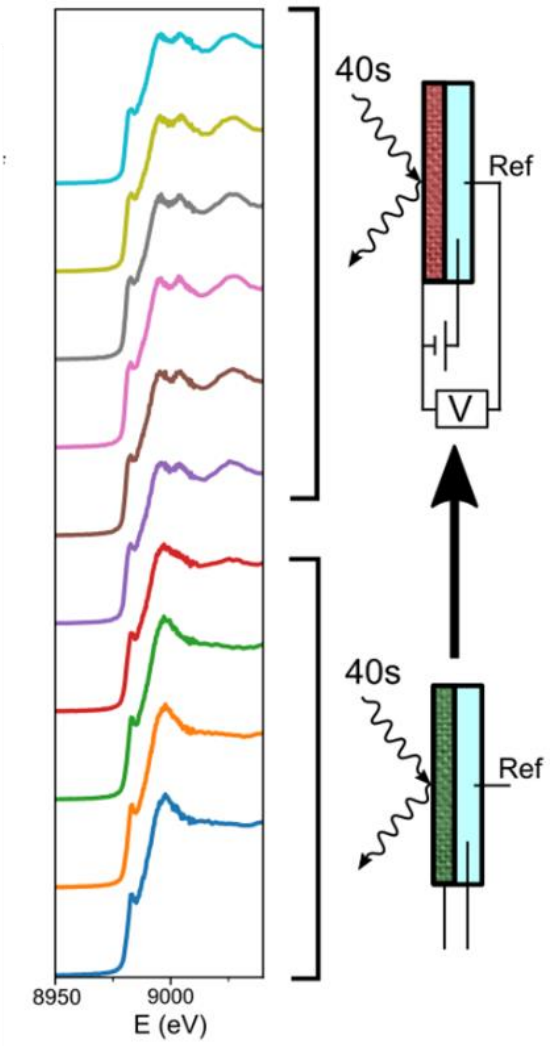

Figure 4.2. EC-XANES with four scans at open circuit and the remainder during bias at -0.6 V vs. RHE. At the very end of the fourth scan, bias is applied. A transition to Cu^0 is observed qualitatively by the fifth scan, the completion of which coincides with 40s having passed since application of bias. No change is observed in subsequent scans.

Electrodes that are observed to become metallic rapidly under bias were also extracted and allowed to dry under ambient conditions as normal, as shown in Figure 4.3. When XANES is conducted on such electrodes, the original characteristic oxidized feature is observed. Hence, the correct structure is confirmed, corroborating that Cu_2O only develops afterwards at open circuit.

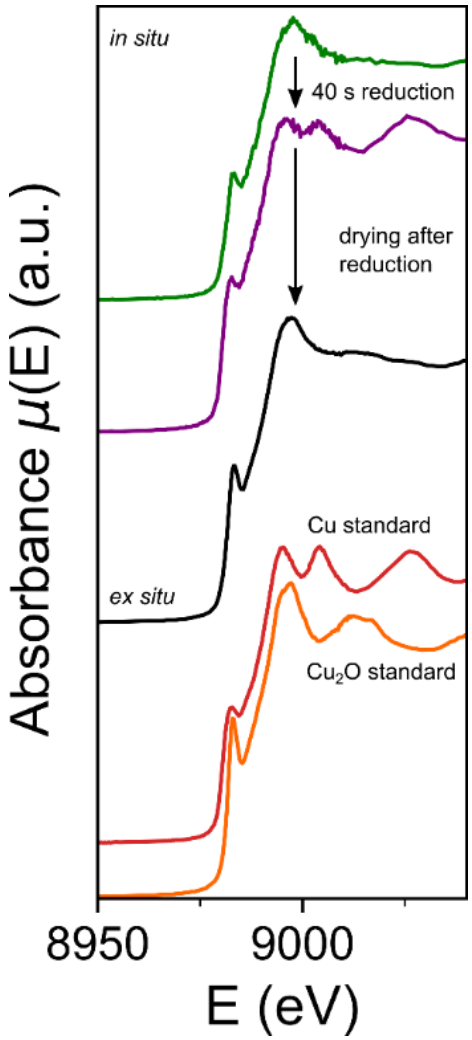

Figure 4.3. The full transformation sequence of the 7 nm Cu NP ensembles as captured by *in situ* and *ex situ* XANES. The 7 nm NPs exhibit metallic Cu^0 within 40s of reductive bias, after which the electrode is dried at ambient conditions, creating a Cu_2O-rich composition which was shown previously (see Chapter 3, Fig. 3.9) to correspond to the single crystal cubes.

4.4.2 *In situ* liquid cell electrochemical (scanning) transmission electron microscopy

Considering the rapid kinetics observed by liquid cell XAS, further elucidation would require more time-resolved techniques. Hence, we developed a system to visually track NP evolution by EC-HAADF-STEM (Fig. 4.4). The cell design is a commercial Hummingbird cell (P7) which uses three interdigitated electrodes that recur in a three electrode pattern across the rectangular viewing window. We use one of these fingers as a pseudo-reference electrode while the other two are used as working and counter. Two-electrode experiments (*i.e.* without the pseudo-reference electrode) were also performed with similar results in aggregate; however, the value of the potential at the cathode is more difficult to determine and so are not presented here.

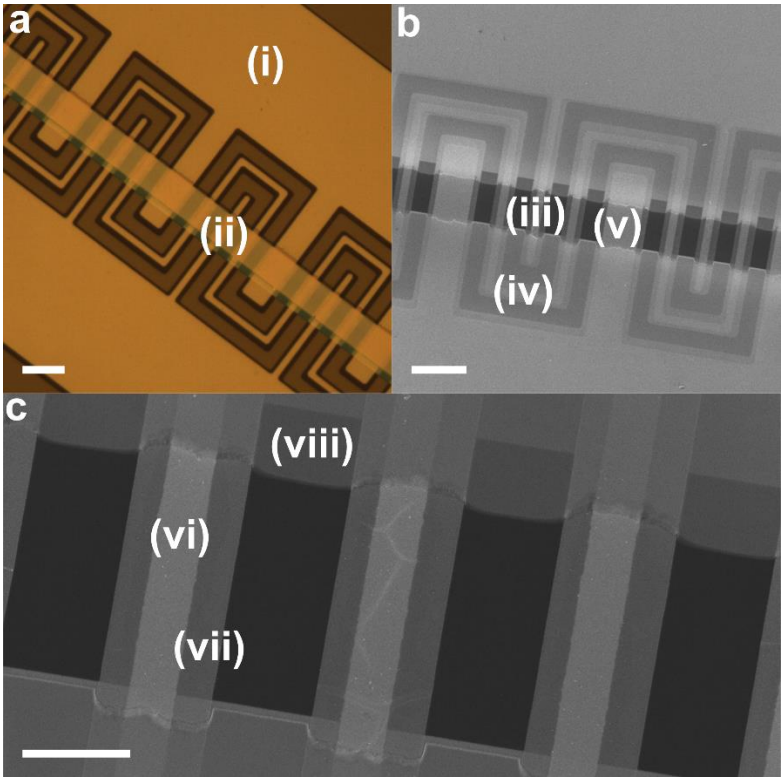

Figure 4.4. The electrochemical liquid cell TEM chip used in *in situ* (S)TEM experiments, imaged by (a) optical microscopy (scale bar 30 μm) and (b-c) SEM (scale bars 30, 10 μm). The cell is fabricated on a (i) Si chip with (ii) a 30 μm x 650 μm silicon nitride viewing window. The 3-electrode setup is shown in panel (b), where the (iii) working electrode is flanked by two fingers of a snaking (iv) reference electrode, followed by a wider (v) counter electrode. Each electrode is composed of (vi) a Pt finger coated with (vii) a thin layer of carbon, which makes up the electron-transparent electrode shown in the rest of this work. Finally, the chip is treated with (viii) a passivation layer to improve liquid confinement.

Both bright field TEM and HAADF-STEM techniques were used to illuminate the structural evolution over the first few seconds of applying potential. Unfortunately, the spatial resolution does not allow the full resolution of the 7 nm nanoparticles, largely due to the system's instability under applied potential. However, resolution of 20 nm structures is possible. Within a second of bias, ~20 nm structures appear to grow from the 7 nm NPs under both BF and HAADF techniques (Figs. 4.5 and 4.6).

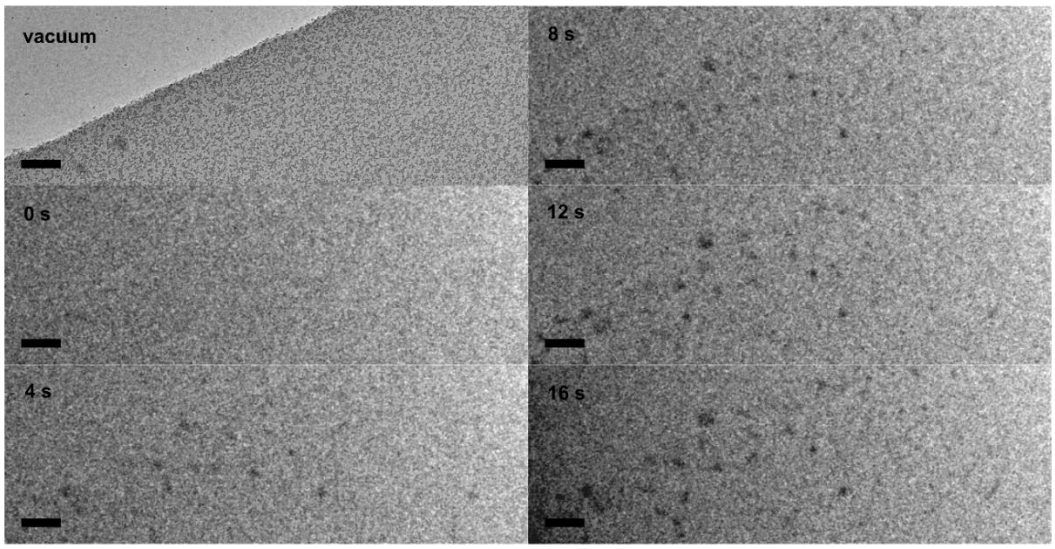

Figure 4.5. A typical bright field (BF) TEM experiment under electrochemical bias at -0.6 V vs. the carbon pseudo-reference electrode with *ex situ* TEM beforehand (upper left) for comparison. Although the particles are easily resolvable under vacuum conditions at this magnification, the liquid layer significantly reduces visibility compared to the BF-TEM shown elsewhere in this dissertation. However, the growth of similar size structures is observed on a comparable time scale of a few seconds. The remaining structures are likely still too small to observe. Scale bars 200 nm.

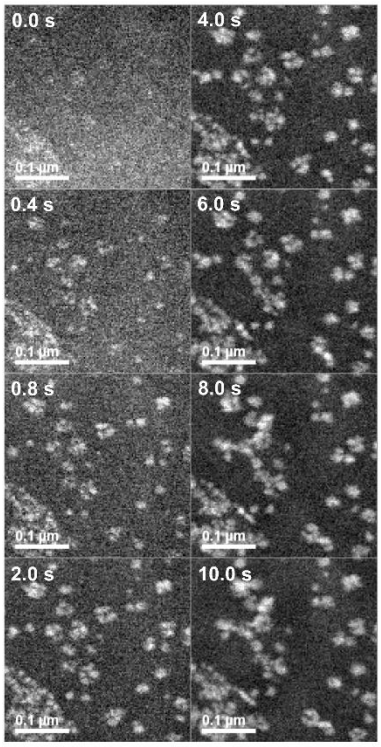

Figure 4.6. EC-HAADF-STEM of the 7 nm Cu NP system taken over a 10s biasing period. Frames were taken at 5 frames per second, though only a select few are shown here. Although the original 7 nm NPs cannot be observed, the appearance of ~20 nm irregular structures is evident within 1

second. The lack of spatial resolution is again attributed to the instability and reactivity of the overall system, due to both radiolysis of electrolyte from electron beam knock-on and the evolution of the particle system itself being more sensitive than is able to be captured routinely with high-magnification STEM.

When the EC-TEM cell is then dried at ambient conditions, cubic structures are commonly found on the electrodes, which are characterized as single crystal Cu_2O (Fig. 4.6 and 4.7), confirming that catalytically relevant structures have formed for the biasing period of EC-TEM.

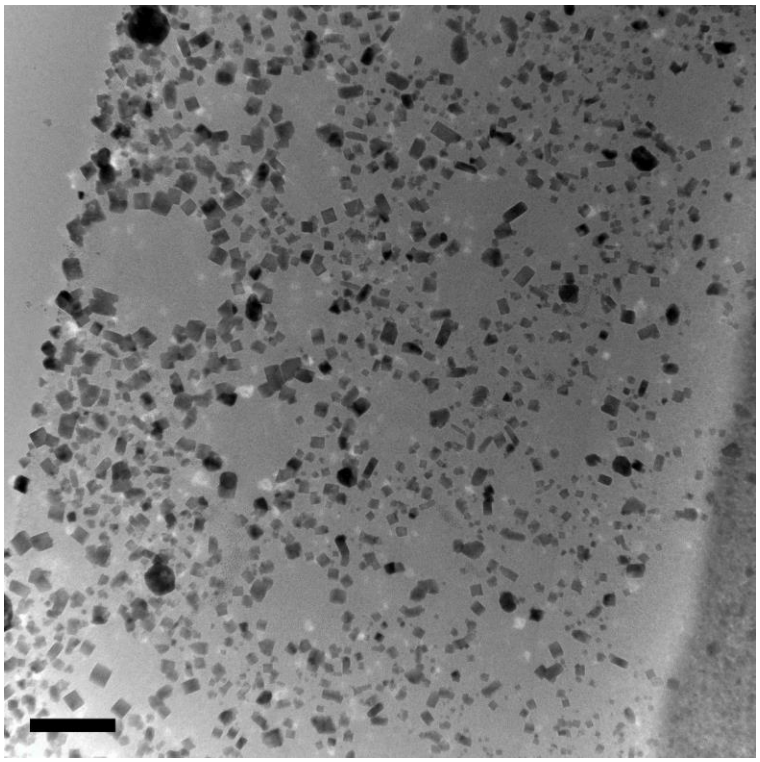

Figure 4.6. A lower magnification view of the working electrode after EC-TEM biasing experiments, showing the predominance of cuboidal Cu_2O structures on the electrode after drying at ambient conditions. Scale bar 500 nm.

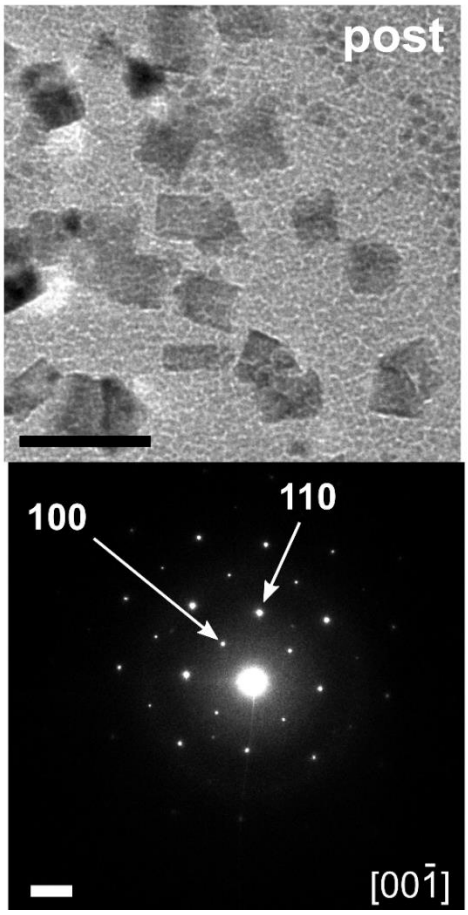

Figure 4.7. *Ex situ* TEM at higher magnification of the EC-STEM electrode after biasing, showing the expected NP-to-cube evolution along with some unreacted NPs (scale bar 100 nm), with nanobeam electron diffraction on a single cube in the region showing single-crystal Cu_2O (scale bar 2 nm^{-1}).

In contrast, larger (15-20 nm) nanoparticles do not undergo much structural change even after 60s of bias (Fig. 4.8), as expected from the post-electrolysis structures of Sample L that indicate minimal movement (Chapter 3, Fig. 3.15). In this case, the original nanoparticles can be clearly resolved and their circular outlines (owing to their spherical morphology) well-defined even in a packed arrangement. Hence, the lack of evolution can be contrasted against the growth of apparently random structures observed in Figure 4.6, despite both datasets showing ~20 nm structures and unable to resolve the original 7 nm particles.

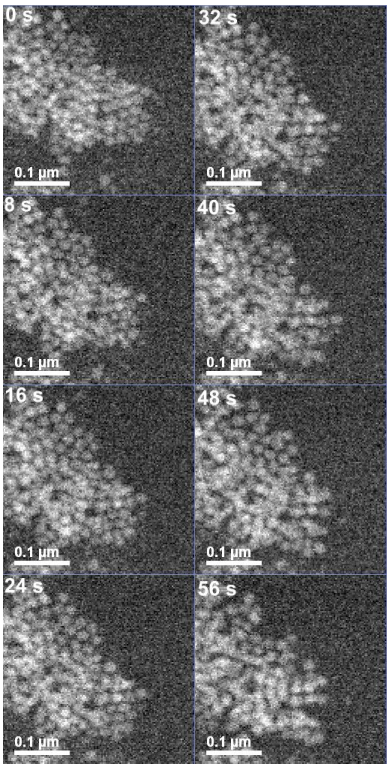

Figure 4.8. *In situ* STEM of larger Cu NPs (20 nm diameter) over the course of 60s of bias at -0.6 V vs. a carbon pseudo-reference. In contrast with the process shown in Fig. 4, the particles are easily resolvable because of their larger size and do not change their structure much despite constant bias, consistent with what is shown in Fig. 3.15 for the nanoparticles used in this size regime.

4.4.3 On the limitations of EC-(S)TEM

Limitations of EC-(S)TEM for CO_2 electroreduction studies, particularly on nanoparticles, merit addressing. Chief among them is the difficulty of achieving high resolution. Although factors such as scattering from the liquid layer (500 nm) certainly contribute, the greatest challenge for resolving the 7 nm NPs, as opposed to 20 nm particles, is their intrinsically dynamic nature with respect to bias or beam, which precludes higher magnifications of bright field techniques. The movies that correspond to the following observations are not included with this dissertation but will be with the aforementioned publication.

Beam induced motion of NPs at high magnifications of EC-BF-TEM tends to result in the formation of large dendrites that are different from the original bias induced evolution, which is further confirmed by the absence of the oxide cubes afterwards. Therefore, we elected to use EC-HAADF-STEM at magnifications in which the beam effect could be managed through tuning the rastering of the beam, to a point at which it did not obviously disrupt the evolution of the structures.

Conducting extended periods of electrolysis brings additional issues. First, accumulation and evolution of gas bubbles starts to interfere with the experiment, resulting in the loss of electrolyte and rupture of the cell itself. The production of byproducts at other electrodes (*i.e.* counter electrode) needs consideration as well. During the short time of bias studied here, the evolution is not affected, especially given the prevalence of the expected oxide cube structures

after electrolysis. However, extremely large structures on the order of several hundred nm or greater are observed during electrolyses that happen to extend beyond a few minutes. These are attributed to reductive deposition of the oxidized species generated at the counter electrode. The effects of these adventitious reactive species at an accelerated pace, when violent liquid movement resulting from bubble formation results in increased convective transport across the cell, causes a rapid growth in adventitious inorganic material. These considerations must inform the design of future *in situ* EC-TEM studies for electroreduction catalysts.

4.4.4 On the meaning of electrochemical scrambling

Nevertheless, we now combine these *in situ* observations in conjunction with our *ex situ* observations from Chapter 3. Together, we find that electrochemical bias induces explosive fusion of a NP ensemble, which we term scrambling. The electrochemical scrambling of Cu nanocrystals results in disordered metallic nanostructures at the steady-state (Sample O) with high C_{2+} selectivity and intrinsic C-C activity (Fig. 4.9). This relative loss of atomic order is likely what triggers a complete "recrystallization" to a single crystalline Cu_2O nanocube on air exposure. The effect is largest for small nanocrystals, owing to their higher energy increasing the tendency for free atomic migration upon bias as represented by their high mobility. In contrast, larger NPs scramble to a lesser extent, while redox pulses allow periods of oxide crystallization to interrupt the scrambling process, resulting in Samples L/P exhibiting more typical polycrystalline Cu structures surrounded by oxide shells. The mechanism by which disorder develops and is maintained in the scrambled NP system bears some resemblance to previously shown atom dynamics at grain boundaries, as well as to phenomena such as surface premelting.

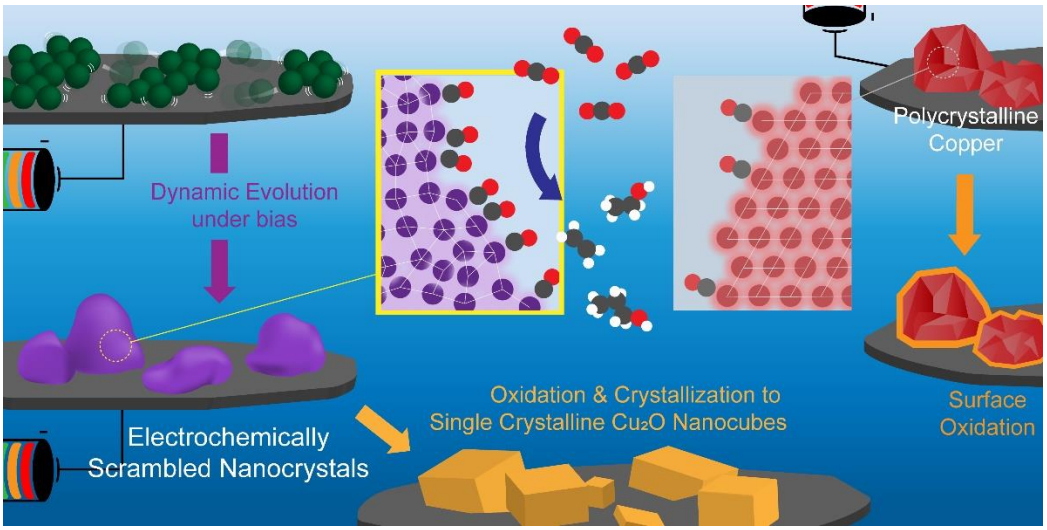

Figure 4.9. Unified description of electrochemically scrambled nanocrystals with disordered surfaces that enhance CO_2-to-C_{2+}, vs. relatively inactive polycrystalline Cu nanocrystals.

The phenomenon induced by electrochemical scrambling, namely, the apparent formation of a disordered metal structured from crystalline nanocrystal precursors, suggests rich nanoscale dynamics under electrochemical conditions. Here, we briefly discuss analogies in the materials science literature to consider the possible mechanisms. We emphasize that this discussion is

exploratory, and that a deep, rigorous investigation into the physics implied here could unearth substantial insight into the effects of electrochemistry on nanoscale systems.

The steady-state structure formed should be in an energetically volatile state, considering its post-reaction susceptibility to complete recrystallization into single crystal Cu_2O cubes. Thus, a primary consideration is how the disordered structure is maintained over electrolysis, rather than crystallizing over time as would be favored thermodynamically. One explanation is that the dynamic mobility of the Cu NPs and their inter-proximity as an ensemble allows fast fusion between them, creating multiple pinned minuscule crystallite junctions that impede boundary or defect migration and crystal growth.[128]

This explanation covers why disorder remains at the steady-state, but does not sufficiently address how the disorder originally arises. At the onset of bias, rapid atomic migration must occur, coupled with a breakage of Cu-Cu bonds to achieve the loss of crystalline order. This process is analogous to melting, albeit at temperatures far below the melting point (or even surface premelting points) of Cu.[129] Notably, in addition to surface premelting, premelting has been observed at grain boundaries and other defects in model crystal systems,[130] which compose a large portion of the 7 nm NP volume relative to larger NPs. In sum, we believe the high energetics of small Cu NPs associated with their relatively larger portion of defective atoms (*i.e.* undercoordinated atoms on the surface and crystal boundaries) allows high degree of freedom for atomic motion and the resulting disordered structure when biased.

So far, we do not have a definitive idea of whether the steady-state scrambled structures are in flux, *i.e.* the constituent atoms or structural units are in continuous motion as in a liquid-like state. All we can provide at this stage is a stationary picture of the coordination environment for the steady-state structure. Therefore, while at least the formation of the disordered structures must have resulted from the formation of a highly mobile "liquid" phase at onset of bias, followed by "supercooling" into a glassy structure during fusion into larger particles,[131] we cannot completely rule out the possibility of the formation and preservation of the "liquid" phase throughout resulting from a process resembling surface premelting, which is also cited as an important activation step in thermal catalysis.[129] Regardless, it still holds that the disordered and glassy surface of copper promotes multicarbon formation at reduced overpotentials (*i.e.* less energy input).

The glassy disordered surface arising from scrambling exhibits increased electrochemical binding strength, which translates to a higher population of strongly-bound *CO. Additionally, relaxing the geometric constraint of crystallinity may allow configurations that alleviate the undesired repulsive interactions of a high density of bound *CO,[132] comparable to the creation of optimal geometries in enzymatic systems. The sum of these effects likely plays a major role in the overpotential reduction towards C-C coupling in the scrambled nanocrystal system, as summarized visually in Figure 4.10. Catalysts exhibiting a lower degree of disorder (*e.g.* Samples L/P) thus are only able to yield comparable C_{2+} activity at elevated potentials (-0.9 V and beyond) (Chapter 3, Fig. 3.35). Given the high degree of structural disorder and complete crystallization to oxide cubes at a release of bias, the scrambled state formed should be metastable. The question of how it is maintained during CO_2 reduction raises an intriguing opportunity to understand the structural requirements for its sustenance. Further insights along this direction will present opportunities for designing catalysts with the necessary characteristics to attain similarly active states.

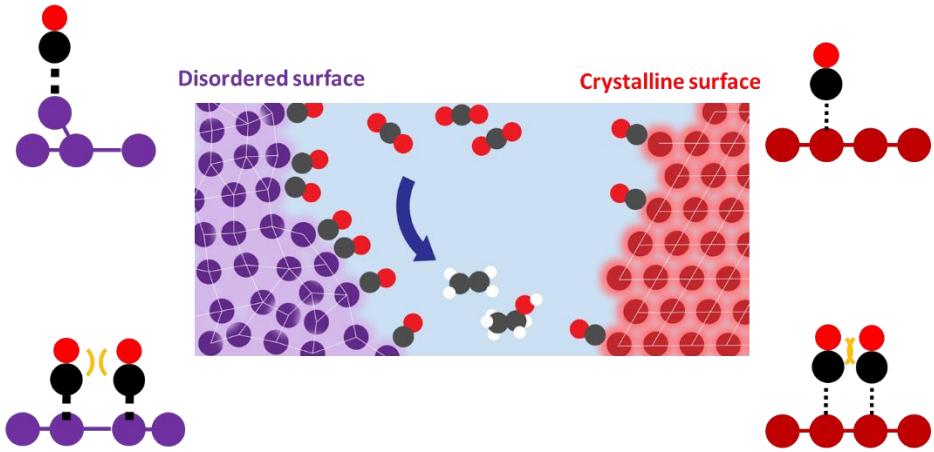

Figure 4.10. Two parallel, potentially complementary avenues for CO_2-to-C_{2+} enhancement on the scrambled disordered surface vs. a typical crystalline (albeit nanostructured) surface. First, an undercoordinated surface may promote adsorbate binding as shown in Chapter 3 with underpotential desorption. Secondly, relaxation of the geometric constraint in the crystal structure at the surface may mitigate CO-CO repulsion as previously shown in gas phase catalysis.

4.5 Conclusions and Perspective

Using an arsenal of techniques as illuminated in Chapters 3 and 4, we have revealed electrochemically scrambled nanocrystals to result from the dynamic fusion of Cu NPs, creating disordered Cu surfaces that are responsible for high CO_2-to-C_{2+} electroconversion activity. By concentrating these disordered active surfaces relative to bulk volume and inert surface area, the scrambled NP catalyst both reveals deeper structural insight for multicarbon formation *via* ensemble-level characterization, and achieves superior catalytic performance through considerations of intrinsic activity or atom economy. Moreover, we emphasize that the most active catalysts may be the most structurally unstable, requiring characterization beyond common *ex situ* techniques.

Critically, what remains to be seen is whether these structural dynamics can be controlled. I will use the remainder of this chapter to outline the methods and reasoning to be employed in our approach to doing so. Figure 4.11 shows a simple schematic of the various parameters that can be considered major variables that potentially influence the evolution of the nanoparticle system: the nanoparticle's intrinsic nature (A), the surrounding electrolyte and electrochemical interface (B), the relationship with the support material (C), the surrounding nanoparticle ensemble (D), and the applied electrochemical potential (E). We can consider the electrochemical evolution as roughly analogous to colloidal nanocrystal synthesis. The five factors listed above are thus proxies of typical synthetic parameters, such as metal precursor identity (A), surfactant and solvent (B, C), concentration (D), and temperature/energy (E).

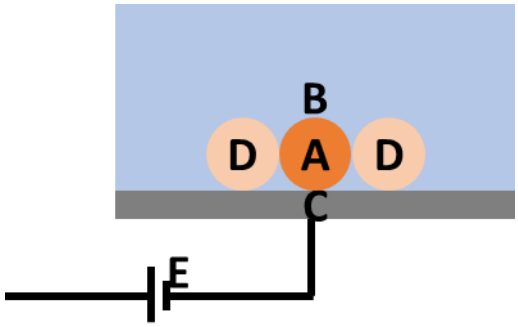

Figure 4.11. The main parameters that are expected to influence electrochemical evolution.

Each of the five parameters to be varied confers benefits to the study proposed. However, I will argue that the study of varying electrochemical environment and how different electrochemical interfaces modulate the evolution of a material is especially timely. Recent work has veered away from aqueous CO_2 reduction towards the high-rate reduction of CO_2 in a gas diffusion environment.[19,133,134] In such environments, the pH of the electrolyte can be raised to >13 in order to suppress the competing HER and also potentially promote CO_2 reduction products through hydroxide action.[68] Furthermore, alkaline environments are also being used in CO reduction studies, for which the gaseous reagent does not engage in buffering behavior with the electrolyte. Hence, the study of electrochemical evolution in alkaline electrolytes (Figure 4.12) will be a necessary and timely first step to understanding how such processes may be harnessed for these new electrochemical environments.

Figure 4.12. Study of variation in the electrochemical environment towards alkaline environments (potentially with CO as the reagent instead of CO_2, or potentially in a gas diffusion architecture) is proposed as a first step to control the evolution.

Chapter 5. Outlook and Perspective on Materials Development for CO_2 Electrocatalysis

In this chapter I summarize the whole of this dissertation. I then offer a personal outlook and perspective on the present state of the art in CO_2 electrocatalysis research, especially towards multicarbon products. I consider the field from the lens of materials science development, particularly from the standpoint of basic research.

In Chapter 1, I introduced the benefits of electrochemistry towards solving some of modern society's most pressing energy concerns. I discussed the basic electrochemistry, thermodynamics, and kinetic considerations of CO_2 reduction in an aqueous environment, including a definition of fundamental concepts and a perspective on the evaluation of CO2RR catalysts. I briefly surveyed recent work on CO2RR electrocatalyst development, and followed with a discussion on how structural dynamics of such electrocatalysts have become increasingly important to consider. I then introduced the throughline of my work, as a subtle paradigm shift from treating such structural dynamics as factors to mitigate, towards understanding them as knobs of catalyst manipulation.

In Chapter 2, I discussed how ultrathin copper nanowires served as an interesting model system to reveal the structure sensitivity of CO2RR. The high selectivity of such nanowires towards methane at high overpotential was seen to degrade rapidly over electrolysis, concurrent with a structural change of the catalyst. Under the philosophy of mitigating structural change, graphene oxide wrapping was employed as a strategy to protect the catalyst and preserve its selectivity. Through this work, I showed how such structural preservation strategies are interesting methods of improving catalyst stability, but also an important tool for illuminating the sensitivity of catalytic activity on surface structure as both evolve over time.

In Chapter 3, I introduced a structurally evolving copper nanoparticle ensemble catalyst and its especially intriguing structural evolution unexpectedly towards cuboids, coupled with its low-overpotential formation of multicarbon products. I comprehensively described the *ex situ* evolution behavior as being characterized by a signature formation of cuprous oxide single crystal cubes. I then showed how such evolution is implausible under reaction conditions, and used passivation strategies to more deeply characterize a surface more likely to be the true *in situ* active structure. Through a battery of characterization techniques, I eventually show that the active *in situ* structure is characterized by apparent disorder in the crystal structure, discussion the implications of such a structure on the intrinsic activity of the catalyst towards multicarbon products.

In Chapter 4, I presented how *in situ* electrochemical liquid cell characterization methods can further corroborate our results in Chapter 3, but also reveal new insights regarding the kinetics of such processes. I showed the evolution as characterized by *in situ* EC-XAS and EC-TEM, directly visualizing the electrochemical evolution in real time by both structure and composition. I then discussed how EC-(S)TEM may be limited in its current state for assisting development of CO2RR catalysts, but where in its limited state it may still offer important insights. At the end, I closed by musing on the physical nature of the electrochemical evolution described in the previous two chapters, and discussed further timely directions inspired by recent work in the literature to

expand the study of electrochemical evolution and continue to approach the idealized control over such processes towards aiding catalyst design.

The idea of structural evolution and structural dynamics is not new to heterogeneous catalysis – however, with heterogeneous electrocatalysis still relatively young, I consider this direction a wide expanse of fertile, unexplored research. The most exciting prospects for such research lies not, in my opinion, in the new and improved advances to catalyst design that may develop, but rather in the potential for the field to change its perspective over the fundamental physical chemistry over a solid surface behavior under an applied bias in an electrochemical interface. Even the reconstruction of surfaces under controlled atmospheres is poorly understood – the sheer complexity of an electrochemical interface and an applied electrochemical potential promises rich and intricate physics at the atomic level, physics that to my knowledge remain as salient gaps in our understanding of even the most common materials (*e.g.* copper).

With such prospects in fundamental physical chemistry provided by such study of electrocatalysts, it is slightly disappointing to sense that the field at large has pivoted towards a technology-centric view in which studies are rewarded primarily for reporting high activity performance. As a case in point, the translation towards gas diffusion architectures is admittedly a critical step towards real, commercial-scale application of such technology. However, the process of this translation has thus far resulted in a sacrifice over understanding of the interface, with abstracts and conclusions constantly fixating on how interesting the makeup of products exiting a cell is. It is my profound hope that this is only a brief phase in the rapidly accelerating study of CO2RR electrocatalysis, and as the hype of improved performance dies down, those dedicated to the deep study of fundamental electrochemistry will continue to unveil new science that exists at the interface of material, electrolyte, and electrochemical potential.

References

(1) Chu, S.; Cui, Y.; Liu, N. The Path towards Sustainable Energy. *Nat. Mater.* **2017**, *16* (1), 16–22. https://doi.org/10.1038/nmat4834.

(2) Mechler, R.; Bouwer, L. M.; Linnerooth-Bayer, J.; Hochrainer-Stigler, S.; Aerts, J. C. J. H.; Surminski, S.; Williges, K. Managing Unnatural Disaster Risk from Climate Extremes. *Nat. Clim. Chang.* **2014**, *4* (4), 235–237. https://doi.org/10.1038/nclimate2137.

(3) Pattyn, F.; Ritz, C.; Hanna, E.; Asay-Davis, X.; DeConto, R.; Durand, G.; Favier, L.; Fettweis, X.; Goelzer, H.; Golledge, N. R.; et al. The Greenland and Antarctic Ice Sheets under 1.5 °C Global Warming. *Nat. Clim. Chang.* **2018**, *8* (12), 1053–1061. https://doi.org/10.1038/s41558-018-0305-8.

(4) Diaz, D.; Moore, F. Quantifying the Economic Risks of Climate Change. *Nat. Clim. Chang.* **2017**, *7* (11), 774–782. https://doi.org/10.1038/nclimate3411.

(5) Kroeker, K. J.; Kordas, R. L.; Crim, R.; Hendriks, I. E.; Ramajo, L.; Singh, G. S.; Duarte, C. M.; Gattuso, J. P. Impacts of Ocean Acidification on Marine Organisms: Quantifying Sensitivities and Interaction with Warming. *Glob. Chang. Biol.* **2013**, *19* (6), 1884–1896. https://doi.org/10.1111/gcb.12179.

(6) Verma, S.; Kim, B.; Jhong, H. R. M.; Ma, S.; Kenis, P. J. A. A Gross-Margin Model for Defining Technoeconomic Benchmarks in the Electroreduction of CO2. *ChemSusChem* **2016**, *9* (15), 1972–1979. https://doi.org/10.1002/cssc.201600394.

(7) Montoya, J. H.; Seitz, L. C.; Chakthranont, P.; Vojvodic, A.; Jaramillo, T. F.; Nørskov, J. K. Materials for Solar Fuels and Chemicals. *Nat. Mater.* **2016**, *16* (1), 70–81. https://doi.org/10.1038/nmat4778.

(8) Appel, A. M.; Bercaw, J. E.; Bocarsly, A. B.; Dobbek, H.; DuBois, D. L.; Dupuis, M.; Ferry, J. G.; Fujita, E.; Hille, R.; Kenis, P. J. A.; et al. Frontiers, Opportunities, and Challenges in Biochemical and Chemical Catalysis of CO_2 Fixation. *Chem. Rev.* **2013**, *113* (8), 6621–6658. https://doi.org/10.1021/cr300463y.

(9) Wang, M.; Torbensen, K.; Salvatore, D.; Ren, S.; Joulié, D.; Dumoulin, F.; Mendoza, D.; Lassalle-Kaiser, B.; Işci, U.; Berlinguette, C. P.; et al. CO2 Electrochemical Catalytic Reduction with a Highly Active Cobalt Phthalocyanine. *Nat. Commun.* **2019**, *10* (1). https://doi.org/10.1038/s41467-019-11542-w.

(10) Ren, S.; Joulié, D.; Salvatore, D.; Torbensen, K.; Wang, M.; Robert, M.; Berlinguette, C. P. Molecular Electrocatalysts Can Mediate Fast, Selective CO2 Reduction in a Flow Cell. *Science* **2019**, *365* (6451), 367–369. https://doi.org/10.1126/science.aax4608.

(11) Ross, M. B.; De Luna, P.; Li, Y.; Dinh, C. T.; Kim, D.; Yang, P.; Sargent, E. H. Designing Materials for Electrochemical Carbon Dioxide Recycling. *Nat. Catal.* **2019**, *2* (8), 648–658. https://doi.org/10.1038/s41929-019-0306-7.

(12) Clark, E. L.; Resasco, J.; Landers, A.; Lin, J.; Chung, L. T.; Walton, A.; Hahn, C.; Jaramillo, T. F.; Bell, A. T. Standards and Protocols for Data Acquisition and Reporting for Studies of the Electrochemical Reduction of Carbon Dioxide. *ACS Catal.* **2018**, *8* (7), 6560–6570. https://doi.org/10.1021/acscatal.8b01340.

(13) Singh, M. R.; Clark, E. L.; Bell, A. T. Effects of Electrolyte, Catalyst, and Membrane Composition and Operating Conditions on the Performance of Solar-Driven Electrochemical Reduction of Carbon Dioxide. *Phys. Chem. Chem. Phys.* **2015**, *17* (29), 18924–18936. https://doi.org/10.1039/c5cp03283k.

(14) Dunwell, M.; Lu, Q.; Heyes, J. M.; Rosen, J.; Chen, J. G.; Yan, Y.; Jiao, F.; Xu, B. The

Central Role of Bicarbonate in the Electrochemical Reduction of Carbon Dioxide on Gold. *J. Am. Chem. Soc.* **2017**, *139* (10), 3774–3783. https://doi.org/10.1021/jacs.6b13287.
(15) Wuttig, A.; Yoon, Y.; Ryu, J.; Surendranath, Y. Bicarbonate Is Not a General Acid in Au-Catalyzed CO 2 Electroreduction. *J. Am. Chem. Soc.* **2017**, *139* (47), 17109–17113. https://doi.org/10.1021/jacs.7b08345.
(16) Zhu, S.; Jiang, B.; Cai, W.-B.; Shao, M. Direct Observation on Reaction Intermediates and the Role of Bicarbonate Anions in CO 2 Electrochemical Reduction Reaction on Cu Surfaces. *J. Am. Chem. Soc.* **2017**, *139* (44), 15664–15667. https://doi.org/10.1021/jacs.7b10462.
(17) Liu, K.; Smith, W. A.; Burdyny, T. Introductory Guide to Assembling and Operating Gas Diffusion Electrodes for Electrochemical CO 2 Reduction. *ACS Energy Lett.* **2019**, *4* (3), 639–643. https://doi.org/10.1021/acsenergylett.9b00137.
(18) Burdyny, T.; Smith, W. A. CO2 Reduction on Gas-Diffusion Electrodes and Why Catalytic Performance Must Be Assessed at Commercially-Relevant Conditions. *Energy Environ. Sci.* **2019**, *12* (5), 1442–1453. https://doi.org/10.1039/c8ee03134g.
(19) Higgins, D.; Hahn, C.; Xiang, C.; Jaramillo, T. F.; Weber, A. Z. Gas-Diffusion Electrodes for Carbon Dioxide Reduction: A New Paradigm. *ACS Energy Lett.* **2019**, *4* (1), 317–324. https://doi.org/10.1021/acsenergylett.8b02035.
(20) Birdja, Y. Y.; Pérez-Gallent, E.; Figueiredo, M. C.; Göttle, A. J.; Calle-Vallejo, F.; Koper, M. T. M. Advances and Challenges in Understanding the Electrocatalytic Conversion of Carbon Dioxide to Fuels. *Nat. Energy* **2019**, *4* (9), 732–745. https://doi.org/10.1038/s41560-019-0450-y.
(21) Nitopi, S.; Bertheussen, E.; Scott, S. B.; Liu, X.; Engstfeld, A. K.; Horch, S.; Seger, B.; Stephens, I. E. L.; Chan, K.; Hahn, C.; et al. Progress and Perspectives of Electrochemical CO 2 Reduction on Copper in Aqueous Electrolyte. *Chem. Rev.* **2019**, *119* (12), 7610–7672. https://doi.org/10.1021/acs.chemrev.8b00705.
(22) Liu, X.; Xiao, J.; Peng, H.; Hong, X.; Chan, K.; Nørskov, J. K. Understanding Trends in Electrochemical Carbon Dioxide Reduction Rates. *Nat. Commun.* **2017**, *8*, 15438. https://doi.org/10.1038/ncomms15438.
(23) Kuhl, K. P.; Hatsukade, T.; Cave, E. R.; Abram, D. N.; Kibsgaard, J.; Jaramillo, T. F. Electrocatalytic Conversion of Carbon Dioxide to Methane and Methanol on Transition Metal Surfaces. *J. Am. Chem. Soc.* **2014**, *136* (40), 14107–14113. https://doi.org/10.1021/ja505791r.
(24) Hori, Y. Electrochemical CO 2 Reduction on Metal Electrodes. In *Modern Aspects of Electrochemistry*; 2008; pp 89–189.
(25) Kuhl, K. P.; Cave, E. R.; Abram, D. N.; Jaramillo, T. F. New Insights into the Electrochemical Reduction of Carbon Dioxide on Metallic Copper Surfaces. *Energy Environ. Sci.* **2012**, *5* (5), 7050. https://doi.org/10.1039/c2ee21234j.
(26) Peterson, A. a.; Abild-Pedersen, F.; Studt, F.; Rossmeisl, J.; Nørskov, J. K. How Copper Catalyzes the Electroreduction of Carbon Dioxide into Hydrocarbon Fuels. *Energy Environ. Sci.* **2010**, *3* (9), 1311. https://doi.org/10.1039/c0ee00071j.
(27) Garza, A. J.; Bell, A. T.; Head-Gordon, M. Mechanism of CO 2 Reduction at Copper Surfaces: Pathways to C 2 Products. *ACS Catal.* **2018**, *8* (2), 1490–1499. https://doi.org/10.1021/acscatal.7b03477.
(28) Hansen, H. A.; Varley, J. B.; Peterson, A. A.; Nørskov, J. K. Understanding Trends in the

Electrocatalytic Activity of Metals and Enzymes for CO 2 Reduction to CO. *J. Phys. Chem. Lett.* **2013**, *4* (3), 388–392. https://doi.org/10.1021/jz3021155.
(29) Li, H.; Li, Y.; Koper, M. T. M.; Calle-Vallejo, F. Bond Making and Breaking between Carbon, Nitrogen and Oxygen in Electrocatalysis. *J. Am. Chem. Soc.* **2014**, *136*, 15694–15701. https://doi.org/10.1021/ja508649p.
(30) Hori, Y.; Takahashi, I.; Koga, O.; Hoshi, N. Electrochemical Reduction of Carbon Dioxide at Various Series of Copper Single Crystal Electrodes. *J. Mol. Catal. A Chem.* **2003**, *199* (1–2), 39–47. https://doi.org/10.1016/S1381-1169(03)00016-5.
(31) Hori, Y.; Takahashi, R.; Yoshinami, Y.; Murata, A. Electrochemical Reduction of CO at a Copper Electrode. *J. Phys. Chem. B* **1997**, *101* (36), 7075–7081. https://doi.org/10.1021/jp970284i.
(32) Gao, D.; Arán-Ais, R. M.; Jeon, H. S.; Roldan Cuenya, B. Rational Catalyst and Electrolyte Design for CO2 Electroreduction towards Multicarbon Products. *Nat. Catal.* **2019**, *2* (3), 198–210. https://doi.org/10.1038/s41929-019-0235-5.
(33) Arán-Ais, R. M.; Gao, D.; Roldan Cuenya, B. Structure- and Electrolyte-Sensitivity in CO2 Electroreduction. *Acc. Chem. Res.* **2018**, *51* (11), 2906–2917. https://doi.org/10.1021/acs.accounts.8b00360.
(34) Kondratenko, E. V.; Mul, G.; Baltrusaitis, J.; Larrazabal, G. O.; Perez-Ramirez, J.; Larrazábal, G. O.; Pérez-Ramírez, J. Status and Perspectives of CO2 Conversion into Fuels and Chemicals by Catalytic, Photocatalytic and Electrocatalytic Processes. *Energy Environ. Sci.* **2013**, *6* (11), 3112. https://doi.org/10.1039/c3ee41272e.
(35) Yang, D.; Zhu, Q.; Chen, C.; Liu, H.; Liu, Z.; Zhao, Z.; Zhang, X.; Liu, S.; Han, B. Selective Electroreduction of Carbon Dioxide to Methanol on Copper Selenide Nanocatalysts. *Nat. Commun.* **2019**, *10* (1). https://doi.org/10.1038/s41467-019-08653-9.
(36) Manthiram, K.; Beberwyck, B. J.; Alivisatos, A. P. Enhanced Electrochemical Methanation of Carbon Dioxide with a Dispersible Nanoscale Copper Catalyst. *J. Am. Chem. Soc.* **2014**, *136* (38), 13319–13325. https://doi.org/10.1021/ja5065284.
(37) Bushuyev, O. S.; De Luna, P.; Dinh, C. T.; Tao, L.; Saur, G.; van de Lagemaat, J.; Kelley, S. O.; Sargent, E. H. What Should We Make with CO2 and How Can We Make It? *Joule* **2018**, *2* (5), 825–832. https://doi.org/10.1016/j.joule.2017.09.003.
(38) Schouten, K. J. P.; Pérez Gallent, E.; Koper, M. T. M. Structure Sensitivity of the Electrochemical Reduction of Carbon Monoxide on Copper Single Crystals. *ACS Catal.* **2013**, *3* (6), 1292–1295. https://doi.org/10.1021/cs4002404.
(39) Huang, Y.; Handoko, A. D.; Hirunsit, P.; Yeo, B. S. Electrochemical Reduction of CO_2 Using Copper Single-Crystal Surfaces: Effects of CO* Coverage on the Selective Formation of Ethylene. *ACS Catal.* **2017**, *7* (3), 1749–1756. https://doi.org/10.1021/acscatal.6b03147.
(40) Pérez-Gallent, E.; Marcandalli, G.; Figueiredo, M. C.; Calle-Vallejo, F.; Koper, M. T. M. Structure- and Potential-Dependent Cation Effects on CO Reduction at Copper Single-Crystal Electrodes. *J. Am. Chem. Soc.* **2017**, *139* (45), 16412–16419. https://doi.org/10.1021/jacs.7b10142.
(41) Schouten, K. J. P.; Qin, Z.; Pérez Gallent, E.; Koper, M. T. M. Two Pathways for the Formation of Ethylene in CO Reduction on Single-Crystal Copper Electrodes. *J. Am. Chem. Soc.* **2012**, *134* (24), 9864–9867. https://doi.org/10.1021/ja302668n.
(42) Hahn, C.; Hatsukade, T.; Kim, Y.-G.; Vailionis, A.; Baricuatro, J. H.; Higgins, D. C.; Nitopi, S. A.; Soriaga, M. P.; Jaramillo, T. F. Engineering Cu Surfaces for the

Electrocatalytic Conversion of CO_2 : Controlling Selectivity toward Oxygenates and Hydrocarbons. *Proc. Natl. Acad. Sci.* **2017**, *114* (23), 5918–5923. https://doi.org/10.1073/pnas.1618935114.

(43) Gurudayal; Perone, D.; Malani, S.; Lum, Y.; Haussener, S.; Ager, J. W. Sequential Cascade Electrocatalytic Conversion of Carbon Dioxide to C–C Coupled Products. *ACS Appl. Energy Mater.* **2019**, *2* (6), 4551–4559. https://doi.org/10.1021/acsaem.9b00791.

(44) Raciti, D.; Cao, L.; Livi, K. J. T.; Rottmann, P. F.; Tang, X.; Li, C.; Hicks, Z.; Bowen, K. H.; Hemker, K. J.; Mueller, T.; et al. Low-Overpotential Electroreduction of Carbon Monoxide Using Copper Nanowires. *ACS Catal.* **2017**, *7* (7), 4467–4472. https://doi.org/10.1021/acscatal.7b01124.

(45) Bertheussen, E.; Hogg, T. V.; Abghoui, Y.; Engstfeld, A. K.; Chorkendorff, I.; Stephens, I. E. L. Electroreduction of CO on Polycrystalline Copper at Low Overpotentials. *ACS Energy Lett.* **2018**, *3* (3), 634–640. https://doi.org/10.1021/acsenergylett.8b00092.

(46) Sandberg, R. B.; Montoya, J. H.; Chan, K.; N??rskov, J. K.; Nørskov, J. K. CO-CO Coupling on Cu Facets: Coverage, Strain and Field Effects. *Surf. Sci.* **2016**, *654*, 56–62. https://doi.org/10.1016/j.susc.2016.08.006.

(47) Montoya, J. H.; Shi, C.; Chan, K.; Nørskov, J. K. Theoretical Insights into a CO Dimerization Mechanism in CO_2 Electroreduction. *J. Phys. Chem. Lett.* **2015**, *6* (11), 2032–2037. https://doi.org/10.1021/acs.jpclett.5b00722.

(48) Pérez-Gallent, E.; Figueiredo, M. C.; Calle-Vallejo, F.; Koper, M. T. M. Spectroscopic Observation of a Hydrogenated CO Dimer Intermediate During CO Reduction on Cu(100) Electrodes. *Angew. Chemie - Int. Ed.* **2017**, *56* (13), 3621–3624. https://doi.org/10.1002/anie.201700580.

(49) Roberts, F. S.; Kuhl, K. P.; Nilsson, A. High Selectivity for Ethylene from Carbon Dioxide Reduction over Copper Nanocube Electrocatalysts. *Angew. Chemie* **2015**, *127* (17), 5268–5271. https://doi.org/10.1002/ange.201412214.

(50) Gao, D.; Zegkinoglou, I.; Divins, N. J.; Scholten, F.; Sinev, I.; Grosse, P.; Roldan Cuenya, B. Plasma-Activated Copper Nanocube Catalysts for Efficient Carbon Dioxide Electroreduction to Hydrocarbons and Alcohols. *ACS Nano* **2017**, *11* (5), 4825–4831. https://doi.org/10.1021/acsnano.7b01257.

(51) Loiudice, A.; Lobaccaro, P.; Kamali, E. A.; Thao, T.; Huang, B. H.; Ager, J. W.; Buonsanti, R. Tailoring Copper Nanocrystals towards C2 Products in Electrochemical CO2 Reduction. *Angew. Chemie - Int. Ed.* **2016**, *55* (19), 5789–5792. https://doi.org/10.1002/anie.201601582.

(52) Grosse, P.; Gao, D.; Scholten, F.; Sinev, I.; Mistry, H.; Roldan Cuenya, B. Dynamic Changes in the Structure, Chemical State and Catalytic Selectivity of Cu Nanocubes during CO 2 Electroreduction: Size and Support Effects. *Angew. Chemie - Int. Ed.* **2018**, *57* (21), 6192–6197. https://doi.org/10.1002/anie.201802083.

(53) Huang, J.; Hörmann, N.; Oveisi, E.; Loiudice, A.; De Gregorio, G. L.; Andreussi, O.; Marzari, N.; Buonsanti, R. Potential-Induced Nanoclustering of Metallic Catalysts during Electrochemical CO2 Reduction. *Nat. Commun.* **2018**, *9* (1), 3117. https://doi.org/10.1038/s41467-018-05544-3.

(54) Li, C. W.; Ciston, J.; Kanan, M. W. Electroreduction of Carbon Monoxide to Liquid Fuel on Oxide-Derived Nanocrystalline Copper. *Nature* **2014**, *508* (7497), 504–507. https://doi.org/10.1038/nature13249.

(55) Li, C. W.; Kanan, M. W. CO2 Reduction at Low Overpotential on Cu Electrodes

Resulting from the Reduction of Thick Cu2O Films. *J. Am. Chem. Soc.* **2012**, *134* (17), 7231–7234. https://doi.org/10.1021/ja3010978.

(56) Mistry, H.; Varela, A. S.; Bonifacio, C. S.; Zegkinoglou, I.; Sinev, I.; Choi, Y.-W.; Kisslinger, K.; Stach, E. A.; Yang, J. C.; Strasser, P.; et al. Highly Selective Plasma-Activated Copper Catalysts for Carbon Dioxide Reduction to Ethylene. *Nat. Commun.* **2016**, *7* (12123), 1–8. https://doi.org/10.1038/ncomms12123.

(57) Grosse, P.; Gao, D.; Scholten, F.; Sinev, I.; Mistry, H.; Roldan Cuenya, B. Dynamic Changes in the Structure, Chemical State and Catalytic Selectivity of Cu Nanocubes during CO 2 Electroreduction: Size and Support Effects . *Angew. Chemie* **2018**, *130* (21), 6300–6305. https://doi.org/10.1002/ange.201802083.

(58) Ren, D.; Ang, B. S. H.; Yeo, B. S. Tuning the Selectivity of Carbon Dioxide Electroreduction toward Ethanol on Oxide-Derived CuxZn Catalysts. *ACS Catal.* **2016**, *6* (12), 8239–8247. https://doi.org/10.1021/acscatal.6b02162.

(59) Eilert, A.; Cavalca, F.; Roberts, F. S.; Osterwalder, J.; Liu, C.; Favaro, M.; Crumlin, E. J.; Ogasawara, H.; Friebel, D.; Pettersson, L. G. M. M.; et al. Subsurface Oxygen in Oxide-Derived Copper Electrocatalysts for Carbon Dioxide Reduction. *J. Phys. Chem. Lett.* **2017**, *8* (1), 285–290. https://doi.org/10.1021/acs.jpclett.6b02273.

(60) Feng, X.; Jiang, K.; Fan, S.; Kanan, M. W. A Direct Grain-Boundary-Activity Correlation for CO Electroreduction on Cu Nanoparticles. *ACS Cent. Sci.* **2016**, *2* (3), 169–174. https://doi.org/10.1021/acscentsci.6b00022.

(61) Lum, Y.; Ager, J. W. Stability of Residual Oxides in Oxide-Derived Copper Catalysts for Electrochemical CO $_2$ Reduction Investigated with ^{18} O Labeling. *Angew. Chemie Int. Ed.* **2018**, *57* (2), 551–554. https://doi.org/10.1002/anie.201710590.

(62) Cavalca, F.; Ferragut, R.; Aghion, S.; Eilert, A.; Diaz-Morales, O.; Liu, C.; Koh, A. L.; Hansen, T. W.; Pettersson, L. G. M.; Nilsson, A. Nature and Distribution of Stable Subsurface Oxygen in Copper Electrodes during Electrochemical CO 2 Reduction. *J. Phys. Chem. C* **2017**, *121* (39), 25003–25009. https://doi.org/10.1021/acs.jpcc.7b08278.

(63) Garza, A. J.; Bell, A. T.; Head-Gordon, M. Is Subsurface Oxygen Necessary for the Electrochemical Reduction of CO2 on Copper? *J. Phys. Chem. Lett.* **2018**, *9* (3), 601–606. https://doi.org/10.1021/acs.jpclett.7b03180.

(64) Ren, D.; Fong, J.; Yeo, B. S. The Effects of Currents and Potentials on the Selectivities of Copper toward Carbon Dioxide Electroreduction. *Nat. Commun.* **2018**, *9* (1), 925. https://doi.org/10.1038/s41467-018-03286-w.

(65) Lum, Y.; Yue, B.; Lobaccaro, P.; Bell, A. T.; Ager, J. W. Optimizing C–C Coupling on Oxide-Derived Copper Catalysts for Electrochemical CO $_2$ Reduction. *J. Phys. Chem. C* **2017**, *121* (26), 14191–14203. https://doi.org/10.1021/acs.jpcc.7b03673.

(66) Handoko, A. D.; Ong, C. W.; Huang, Y.; Lee, Z. G.; Lin, L.; Panetti, G. B.; Yeo, B. S. Mechanistic Insights into the Selective Electroreduction of Carbon Dioxide to Ethylene on Cu2O-Derived Copper Catalysts. *J. Phys. Chem. C* **2016**, *120* (36), 20058–20067. https://doi.org/10.1021/acs.jpcc.6b07128.

(67) Clark, E. L.; Bell, A. T. Direct Observation of the Local Reaction Environment during the Electrochemical Reduction of CO2. *J. Am. Chem. Soc.* **2018**, *140* (22), 7012–7020. https://doi.org/10.1021/jacs.8b04058.

(68) Jouny, M.; Luc, W.; Jiao, F. High-Rate Electroreduction of Carbon Monoxide to Multi-Carbon Products. *Nat. Catal.* **2018**, *1* (10), 748–755. https://doi.org/10.1038/s41929-018-0133-2.

(69) Dutta, A.; Rahaman, M.; Luedi, N. C.; Mohos, M.; Broekmann, P. Morphology Matters: Tuning the Product Distribution of CO 2 Electroreduction on Oxide-Derived Cu Foam Catalysts. *ACS Catal.* **2016**, *6* (6), 3804–3814. https://doi.org/10.1021/acscatal.6b00770.
(70) Tao, F.; Grass, M. E.; Zhang, Y.; Butcher, D. R.; Renzas, J. R.; Liu, Z.; Chung, J. Y.; Mun, B. S.; Salmeron, M.; Somorjai, G. A. Reaction-Driven Restructuring of Rh-Pd and Pt-Pd Core-Shell Nanoparticles. *Science* **2008**, *322* (5903), 932–934. https://doi.org/10.1126/science.1164170.
(71) Zugic, B.; Wang, L.; Heine, C.; Zakharov, D. N.; Lechner, B. A. J.; Stach, E. A.; Biener, J.; Salmeron, M.; Madix, R. J.; Friend, C. M. Dynamic Restructuring Drives Catalytic Activity on Nanoporous Gold–Silver Alloy Catalysts. *Nat. Mater.* **2016**, *16* (5), 558–564. https://doi.org/10.1038/nmat4824.
(72) Jiang, H.; He, Q.; Zhang, Y.; Song, L. Structural Self-Reconstruction of Catalysts in Electrocatalysis. **2018**. https://doi.org/10.1021/acs.accounts.8b00449.
(73) De Luna, P.; Quintero-Bermudez, R.; Dinh, C.-T.; Ross, M. B.; Bushuyev, O. S.; Todorović, P.; Regier, T.; Kelley, S. O.; Yang, P.; Sargent, E. H. Catalyst Electro-Redeposition Controls Morphology and Oxidation State for Selective Carbon Dioxide Reduction. *Nat. Catal.* **2018**, *1* (2), 103–110. https://doi.org/10.1038/s41929-017-0018-9.
(74) Kim, Y.-G. G.; Baricuatro, J. H.; Javier, A.; Gregoire, J. M.; Soriaga, M. P. The Evolution of the Polycrystalline Copper Surface, First to Cu(111) and Then to Cu(100), at a Fixed CO 2 RR Potential: A Study by Operando EC-STM. *Langmuir* **2014**, *30* (50), 15053–15056. https://doi.org/10.1021/la504445g.
(75) Manthiram, K.; Surendranath, Y.; Alivisatos, A. P. Dendritic Assembly of Gold Nanoparticles during Fuel-Forming Electrocatalysis. *J. Am. Chem. Soc.* **2014**, *136* (20), 7237–7240. https://doi.org/10.1021/ja502628r.
(76) Li, Y.; Cui, F.; Ross, M. B.; Kim, D.; Sun, Y.; Yang, P. Structure-Sensitive CO 2 Electroreduction to Hydrocarbons on Ultrathin Five-Fold Twinned Copper Nanowires. *Nano Lett.* **2017**, *17* (2), 1312–1317. https://doi.org/10.1021/acs.nanolett.6b05287.
(77) White, J. L.; Baruch, M. F.; Pander, J. E.; Hu, Y.; Fortmeyer, I. C.; Park, J. E.; Zhang, T.; Liao, K.; Gu, J.; Yan, Y.; et al. Light-Driven Heterogeneous Reduction of Carbon Dioxide: Photocatalysts and Photoelectrodes. *Chem. Rev.* **2015**, *115* (23), 12888–12935. https://doi.org/10.1021/acs.chemrev.5b00370.
(78) Kim, D.; Sakimoto, K. K.; Hong, D.; Yang, P. Artificial Photosynthesis for Sustainable Fuel and Chemical Production. *Angew. Chemie - Int. Ed.* **2015**, *54* (11), 3259–3266. https://doi.org/10.1002/anie.201409116.
(79) Rosen, B. A.; Salehi-Khojin, A.; Thorson, M. R.; Zhu, W.; Whipple, D. T.; Kenis, P. J. A.; Masel, R. I. Ionic Liquid-Mediated Selective Conversion of CO_2 to CO at Low Overpotentials. *Science* **2011**, *334* (6056), 643–644. https://doi.org/10.1126/science.1209786.
(80) Lu, Q.; Rosen, J.; Zhou, Y.; Hutchings, G. S.; Kimmel, Y. C.; Chen, J. G.; Jiao, F. A Selective and Efficient Electrocatalyst for Carbon Dioxide Reduction. *Nat. Commun.* **2014**, *5*, 3242. https://doi.org/10.1038/ncomms4242.
(81) Kim, D.; Resasco, J.; Yu, Y.; Asiri, A. M.; Yang, P. Synergistic Geometric and Electronic Effects for Electrochemical Reduction of Carbon Dioxide Using Gold-Copper Bimetallic Nanoparticles. *Nat. Commun.* **2014**, *5*, 4948. https://doi.org/10.1038/ncomms5948.
(82) Zhu, W.; Zhang, Y. J.; Zhang, H.; Lv, H.; Li, Q.; Michalsky, R.; Peterson, A. A.; Sun, S. Active and Selective Conversion of CO2 to CO on Ultrathin Au Nanowires. *J. Am. Chem.*

Soc. **2014**, *136* (46), 16132–16135. https://doi.org/10.1021/ja5095099.
(83) Chen, Y.; Li, C. W.; Kanan, M. W. Aqueous CO2 Reduction at Very Low Overpotential on Oxide-Derived Au Nanoparticles. *J. Am. Chem. Soc.* **2012**, *134* (49), 19969–19972. https://doi.org/10.1021/ja309317u.
(84) Liu, M.; Pang, Y.; Zhang, B.; De Luna, P.; Voznyy, O.; Xu, J.; Zheng, X.; Dinh, C. T.; Fan, F.; Cao, C.; et al. Enhanced Electrocatalytic CO2 Reduction via Field-Induced Reagent Concentration. *Nature* **2016**, *537* (7620), 382–386. https://doi.org/10.1038/nature19060.
(85) Gattrell, M.; Gupta, N.; Co, A. A Review of the Aqueous Electrochemical Reduction of CO2 to Hydrocarbons at Copper. *J. Electroanal. Chem.* **2006**, *594* (1), 1–19. https://doi.org/10.1016/j.jelechem.2006.05.013.
(86) Tang, W.; Peterson, A. A.; Varela, A. S.; Jovanov, Z. P.; Bech, L.; Durand, W. J.; Dahl, S.; Nørskov, J. K.; Chorkendorff, I. The Importance of Surface Morphology in Controlling the Selectivity of Polycrystalline Copper for CO2 Electroreduction. *Phys. Chem. Chem. Phys.* **2012**, *14* (1), 76–81. https://doi.org/10.1039/c1cp22700a.
(87) Zhang, S.; Kang, P.; Meyer, T. J. Nanostructured Tin Catalysts for Selective Electrochemical Reduction of Carbon Dioxide to Formate. *J. Am. Chem. Soc.* **2014**, *136* (5), 1734–1737. https://doi.org/10.1021/ja4113885.
(88) Kas, R.; Kortlever, R.; Yılmaz, H.; Koper, M. T. M.; Mul, G. Manipulating the Hydrocarbon Selectivity of Copper Nanoparticles in CO $_2$ Electroreduction by Process Conditions. *ChemElectroChem* **2015**, *2* (3), 354–358. https://doi.org/10.1002/celc.201402373.
(89) Ren, D.; Deng, Y.; Handoko, A. D.; Chen, C. S.; Malkhandi, S.; Yeo, B. S. Selective Electrochemical Reduction of Carbon Dioxide to Ethylene and Ethanol on Copper(I) Oxide Catalysts. *ACS Catal.* **2015**, *5* (5), 2814–2821. https://doi.org/10.1021/cs502128q.
(90) Baturina, O. A.; Lu, Q.; Padilla, M. A.; Xin, L.; Li, W.; Serov, A.; Artyushkova, K.; Atanassov, P.; Xu, F.; Epshteyn, A.; et al. CO2 Electroreduction to Hydrocarbons on Carbon-Supported Cu Nanoparticles. *ACS Catal.* **2014**, *4* (10), 3682–3695. https://doi.org/10.1021/cs500537y.
(91) Reske, R.; Mistry, H.; Behafarid, F.; Roldan Cuenya, B.; Strasser, P. Particle Size Effects in the Catalytic Electroreduction of CO_2 on Cu Nanoparticles. *J. Am. Chem. Soc.* **2014**, *136* (19), 6978–6986. https://doi.org/10.1021/ja500328k.
(92) Wang, Z.; Yang, G.; Zhang, Z.; Jin, M.; Yin, Y. Selectivity on Etching: Creation of High-Energy Facets on Copper Nanocrystals for CO2 Electrochemical Reduction. *ACS Nano* **2016**, *10* (4), 4559–4564. https://doi.org/10.1021/acsnano.6b00602.
(93) Ma, M.; Djanashvili, K.; Smith, W. A. Controllable Hydrocarbon Formation from the Electrochemical Reduction of CO2 over Cu Nanowire Arrays. *Angew. Chemie - Int. Ed.* **2016**, *55* (23), 6680–6684. https://doi.org/10.1002/anie.201601282.
(94) Raciti, D.; Livi, K. J.; Wang, C. Highly Dense Cu Nanowires for Low-Overpotential CO2 Reduction. *Nano Lett.* **2015**, *15* (10), 6829–6835. https://doi.org/10.1021/acs.nanolett.5b03298.
(95) Xie, M. S.; Xia, B. Y.; Li, Y. W.; Yan, Y.; Yang, Y.; Sun, Q.; Chan, S. H.; Fisher, A.; Wang, X.; Xie, M. S.; et al. Amino Acid Modified Copper Electrodes for the Enhanced Selective Electroreduction of Carbon Dioxide towards Hydrocarbons. *Energy Environ. Sci.* **2016**, *9*, 1687–1695. https://doi.org/10.1039/C5EE03694A.
(96) Cui, F.; Yu, Y.; Dou, L.; Sun, J.; Yang, Q.; Schildknecht, C.; Schierle-Arndt, K.; Yang, P.

Synthesis of Ultrathin Copper Nanowires Using Tris(Trimethylsilyl)Silane for High-Performance and Low-Haze Transparent Conductors. *Nano Lett.* **2015**, *15* (11), 7610–7615. https://doi.org/10.1021/acs.nanolett.5b03422.

(97) Dou, L.; Cui, F.; Yu, Y.; Khanarian, G.; Eaton, S. W.; Yang, Q.; Resasco, J.; Schildknecht, C.; Schierle-Arndt, K.; Yang, P. Solution-Processed Copper/Reduced-Graphene-Oxide Core/Shell Nanowire Transparent Conductors. *ACS Nano* **2016**, *10* (2), 2600–2606. https://doi.org/10.1021/acsnano.5b07651.

(98) Stankovich, S.; Dikin, D. A.; Piner, R. D.; Kohlhaas, K. A.; Kleinhammes, A.; Jia, Y.; Wu, Y.; Nguyen, S. B. T.; Ruoff, R. S. Synthesis of Graphene-Based Nanosheets via Chemical Reduction of Exfoliated Graphite Oxide. *Carbon* **2007**, *45* (7), 1558–1565. https://doi.org/10.1016/j.carbon.2007.02.034.

(99) Chen, Z.; Zhang, X.; Lu, G. Overpotential for CO 2 Electroreduction Lowered on Strained Penta-Twinned Cu Nanowires. *Chem. Sci.* **2015**, *6* (2), 6829–6835. https://doi.org/10.1039/C5SC02667A.

(100) Weng, Z.; Zhang, X.; Wu, Y.; Huo, S.; Jiang, J.; Liu, W.; He, G.; Liang, Y.; Wang, H. Self-Cleaning Catalyst Electrodes for Stabilized CO2 Reduction to Hydrocarbons. *Angew. Chemie Int. Ed.* **2017**. https://doi.org/10.1002/anie.201707478.

(101) Tao, F.; Crozier, P. A. Atomic-Scale Observations of Catalyst Structures under Reaction Conditions and during Catalysis. *Chem. Rev.* **2016**, *116* (6), 3487–3539. https://doi.org/10.1021/cr5002657.

(102) Cui, C.; Gan, L.; Heggen, M.; Rudi, S.; Strasser, P. Compositional Segregation in Shaped Pt Alloy Nanoparticles and Their Structural Behaviour during Electrocatalysis. *Nat. Mater.* **2013**, *12* (8), 765–771. https://doi.org/10.1038/nmat3668.

(103) Gunathunge, C. M.; Li, X.; Li, J.; Hicks, R. P.; Ovalle, V. J.; Waegele, M. M. Spectroscopic Observation of Reversible Surface Reconstruction of Copper Electrodes under CO_2 Reduction. *J. Phys. Chem. C* **2017**, *121* (22), 12337–12344. https://doi.org/10.1021/acs.jpcc.7b03910.

(104) Weng, Z.; Wu, Y.; Wang, M.; Jiang, J.; Yang, K.; Huo, S.; Wang, X.-F.; Ma, Q.; Brudvig, G. W.; Batista, V. S.; et al. Active Sites of Copper-Complex Catalytic Materials for Electrochemical Carbon Dioxide Reduction. *Nat. Commun.* **2018**, *9* (1), 415. https://doi.org/10.1038/s41467-018-02819-7.

(105) Jiang, K.; Sandberg, R. B.; Akey, A. J.; Liu, X.; Bell, D. C.; Nørskov, J. K.; Chan, K.; Wang, H. Metal Ion Cycling of Cu Foil for Selective C–C Coupling in Electrochemical CO2 Reduction. *Nat. Catal.* **2018**, *1* (2), 111–119. https://doi.org/10.1038/s41929-017-0009-x.

(106) Hoang, T. T. H.; Ma, S.; Gold, J. I.; Kenis, P. J. A.; Gewirth, A. A. Nanoporous Copper Films by Additive-Controlled Electrodeposition: CO_2 Reduction Catalysis. *ACS Catal.* **2017**, *7* (5), 3313–3321. https://doi.org/10.1021/acscatal.6b03613.

(107) Kwon, Y.; Lum, Y.; Clark, E. L.; Ager, J. W.; Bell, A. T. CO2 Electroreduction with Enhanced Ethylene and Ethanol Selectivity by Nanostructuring Polycrystalline Copper. *ChemElectroChem* **2016**, *3* (6), 1012–1019. https://doi.org/10.1002/celc.201600068.

(108) Wang, H.; Matios, E.; Wang, C.; Luo, J.; Lu, X.; Hu, X.; Li, W. Rapid and Scalable Synthesis of Cuprous Halide-Derived Copper Nano-Architectures for Selective Electrochemical Reduction of Carbon Dioxide. *Nano Lett.* **2019**, *19* (6), 3925–3932. https://doi.org/10.1021/acs.nanolett.9b01197.

(109) Kim, D.; Kley, C. S.; Li, Y.; Yang, P. Copper Nanoparticle Ensembles for Selective

Electroreduction of CO_2 to C_2–C_3 Products. *Proc. Natl. Acad. Sci.* **2017**, *114* (40), 10560–10565. https://doi.org/10.1073/pnas.1711493114.
(110) Guo, X.; Lv, W.; Li, X.-Y. Additive-Free Shape-Invariant Nano-to-Micron Size-Tuning of Cu_2O Cubic Crystals by Square-Wave Voltammetry. *J. Phys. Chem. C* **2014**, *118* (20), 11062–11077. https://doi.org/10.1021/jp412194q.
(111) Kim, D.; Becknell, N.; Yu, Y.; Yang, P. Room-Temperature Dynamics of Vanishing Copper Nanoparticles Supported on Silica. *Nano Lett.* **2017**, *17* (4), 2732–2737. https://doi.org/10.1021/acs.nanolett.7b00942.
(112) Goodman, E. D.; Schwalbe, J. A.; Cargnello, M. Mechanistic Understanding and the Rational Design of Sinter-Resistant Heterogeneous Catalysts. *ACS Catal.* **2017**, *7* (10), 7156–7173. https://doi.org/10.1021/acscatal.7b01975.
(113) Lamberti, C.; Bordiga, S.; Bonino, F.; Prestipino, C.; Berlier, G.; Capello, L.; D'Acapito, F.; Llabrés I Xamena, F. X.; Zecchina, A. Determination of the Oxidation and Coordination State of Copper on Different Cu-Based Catalysts by XANES Spectroscopy in Situ or in Operando Conditions. *Phys. Chem. Chem. Phys.* **2003**, *5* (20), 4502–4509. https://doi.org/10.1039/b305810g.
(114) Tranquada, J. M.; Heald, S. M.; Moodenbaugh, A. R. X-Ray-Absorption near-Edge-Structure Study of La2-x(Ba,Sr)XCuO4-y Superconductors. *Phys. Rev. B* **1987**, *36* (10), 5263–5274. https://doi.org/10.1103/PhysRevB.36.5263.
(115) Beverskog, B.; Puigdomenech, I. Revised Pourbaix Diagrams for Copper at 25 to 300°C. *J. Electrochem. Soc.* **1997**, *144* (10), 3476. https://doi.org/10.1149/1.1838036.
(116) Finšgar, M.; Milošev, I. Inhibition of Copper Corrosion by 1,2,3-Benzotriazole: A Review. *Corros. Sci.* **2010**, *52* (9), 2737–2749. https://doi.org/10.1016/J.CORSCI.2010.05.002.
(117) Leapman, R. D.; Grunes, L. A.; Fejes, P. L. Study of the L23 Edges in the 3d Transition Metals and Their Oxides by Electron-Energy-Loss Spectroscopy with Comparisons to Theory. *Phys. Rev. B* **1982**, *26* (2), 614–635. https://doi.org/10.1103/PhysRevB.26.614.
(118) Teo, B. K.; Chen, H. S.; Wang, R.; Antonio, M. R. EXAFS of Glassy Metallic Alloys: Amorphous and Crystalline MoNi. *J. Non. Cryst. Solids* **1983**, *58* (2–3), 249–274. https://doi.org/10.1016/0022-3093(83)90028-5.
(119) Giri, S. D.; Sarkar, A. Estimating Surface Area of Copper Powder: A Comparison between Electrochemical, Microscopy and Laser Diffraction Methods. *Adv. Powder Technol.* **2018**, *29* (12), 3520–3526. https://doi.org/10.1016/j.apt.2018.09.034.
(120) Hodnik, N.; Dehm, G.; Mayrhofer, K. J. J. Importance and Challenges of Electrochemical *in Situ* Liquid Cell Electron Microscopy for Energy Conversion Research. *Acc. Chem. Res.* **2016**, *49* (9), 2015–2022. https://doi.org/10.1021/acs.accounts.6b00330.
(121) Handoko, A. D.; Wei, F.; Jenndy; Yeo, B. S.; Seh, Z. W. Understanding Heterogeneous Electrocatalytic Carbon Dioxide Reduction through Operando Techniques. *Nat. Catal.* **2018**, *1* (12), 922–934. https://doi.org/10.1038/s41929-018-0182-6.
(122) Liu, X. H.; Liu, Y.; Kushima, A.; Zhang, S.; Zhu, T.; Li, J.; Huang, J. Y. In Situ TEM Experiments of Electrochemical Lithiation and Delithiation of Individual Nanostructures. *Adv. Energy Mater.* **2012**, *2* (7), 722–741. https://doi.org/10.1002/aenm.201200024.
(123) Yuan, Y.; Amine, K.; Lu, J.; Shahbazian-Yassar, R. Understanding Materials Challenges for Rechargeable Ion Batteries with in Situ Transmission Electron Microscopy. *Nat. Commun.* **2017**, *8* (1), 15806. https://doi.org/10.1038/ncomms15806.
(124) Zhu, G.-Z.; Prabhudev, S.; Yang, J.; Gabardo, C. M.; Botton, G. A.; Soleymani, L. In Situ

Liquid Cell TEM Study of Morphological Evolution and Degradation of Pt–Fe Nanocatalysts During Potential Cycling. *J. Phys. Chem. C* **2014**, *118* (38), 22111–22119. https://doi.org/10.1021/jp506857b.

(125) Zheng, X.; De Luna, P.; García de Arquer, F. P.; Zhang, B.; Becknell, N.; Ross, M. B.; Li, Y.; Banis, M. N.; Li, Y.; Liu, M.; et al. Sulfur-Modulated Tin Sites Enable Highly Selective Electrochemical Reduction of CO2 to Formate. *Joule* **2017**, *1* (4), 794–805. https://doi.org/10.1016/j.joule.2017.09.014.

(126) Nielsen, M. H.; Aloni, S.; De Yoreo, J. J. In Situ TEM Imaging of CaCO3 Nucleation Reveals Coexistence of Direct and Indirect Pathways. *Science* **2014**, *345* (6201), 1158–1162. https://doi.org/10.1126/science.1254051.

(127) Gu, M.; Parent, L. R.; Mehdi, B. L.; Unocic, R. R.; McDowell, M. T.; Sacci, R. L.; Xu, W.; Connell, J. G.; Xu, P.; Abellan, P.; et al. Demonstration of an Electrochemical Liquid Cell for Operando Transmission Electron Microscopy Observation of the Lithiation/Delithiation Behavior of Si Nanowire Battery Anodes. *Nano Lett.* **2013**, *13* (12), 6106–6112. https://doi.org/10.1021/nl403402q.

(128) Holm, E. A.; Foiles, S. M. How Grain Growth Stops: A Mechanism for Grain-Growth Stagnation in Pure Materials. *Science* **2010**, *328* (5982), 1138–1141. https://doi.org/10.1126/science.1187833.

(129) Liu, X.; Wen, X.; Hoffmann, R. Surface Activation of Transition Metal Nanoparticles for Heterogeneous Catalysis: What We Can Learn from Molecular Dynamics. *ACS Catal.* **2018**, *8* (4), 3365–3375. https://doi.org/10.1021/acscatal.7b04468.

(130) Alsayed, A. M.; Islam, M. F.; Zhang, J.; Collings, P. J.; Yodh, A. G. Premelting at Defects within Bulk Colloidal Crystals. *Science* **2005**, *309* (5738), 1207–1210. https://doi.org/10.1126/science.1112399.

(131) Inoue, A. Stabilization of Metallic Supercooled Liquid and Bulk Amorphous Alloys. *Acta Mater.* **2000**, *48* (1), 279–306. https://doi.org/10.1016/S1359-6454(99)00300-6.

(132) Eren, B.; Zherebetskyy, D.; Patera, L. L.; Wu, C. H.; Bluhm, H.; Africh, C.; Wang, L. W.; Somorjai, G. A.; Salmeron, M. Activation of Cu(111) Surface by Decomposition into Nanoclusters Driven by CO Adsorption. *Science* **2016**, *351* (6272), 475–478. https://doi.org/10.1126/science.aad8868.

(133) Ma, S.; Sadakiyo, M.; Luo, R.; Heima, M.; Yamauchi, M.; Kenis, P. J. A. One-Step Electrosynthesis of Ethylene and Ethanol from CO2 in an Alkaline Electrolyzer. *J. Power Sources* **2016**, *301*, 219–228. https://doi.org/10.1016/j.jpowsour.2015.09.124.

(134) Dinh, C.-T.; Burdyny, T.; Kibria, M. G.; Seifitokaldani, A.; Gabardo, C. M.; García de Arquer, F. P.; Kiani, A.; Edwards, J. P.; De Luna, P.; Bushuyev, O. S.; et al. CO2 Electroreduction to Ethylene via Hydroxide-Mediated Copper Catalysis at an Abrupt Interface. *Science* **2018**, *360* (6390), 783–787. https://doi.org/10.1126/science.aas9100.